Michigan Technological University
Digital Commons @ Michigan Tech

Dissertations, Master's Theses and Master's Reports - Open

Dissertations, Master's Theses and Master's Reports

2011

Numerical study on the curling and warping of hardened rigid pavement slabs

Qin Yinghong
Michigan Technological University

Follow this and additional works at: https://digitalcommons.mtu.edu/etds

 Part of the Civil and Environmental Engineering Commons

Copyright 2011 Qin Yinghong

Recommended Citation
Yinghong, Qin, "Numerical study on the curling and warping of hardened rigid pavement slabs", Dissertation, Michigan Technological University, 2011.
https://doi.org/10.37099/mtu.dc.etds/284

Follow this and additional works at: https://digitalcommons.mtu.edu/etds

 Part of the Civil and Environmental Engineering Commons

NUMERICAL STUDY ON THE CURLING AND WARPING OF HARDENED RIGID PAVEMENT SLABS

By

Yinghong Qin

A DISSERTATION

Submitted in partial fulfillment of the requirements for the degree of

DOCTOR OF PHILOSOPHY

(Civil Engineering)

MICHIGAN TECHNOLOGICAL UNIVERSITY

2011

© 2011 Yinghong Qin

This dissertation, “Numerical study on the curling and warping of hardened rigid pavement slabs,” is hereby approved in partial fulfillment of the requirements for the DEGREE OF DOCTOR OF PHILOSOPHY IN CIVIL ENGINEERING

Civil and Environmental Engineering

Signatures:

Dissertation Advisor: _____
Jacob E. Hiller

Department Chair: _____
William M. Bulleit

Date: _____

Contents

List of Figures

List of Tables

Preface

This dissertation computes the environmental loadings that in-service pavement slabs are subjects to. It develops a heat transfer model to predict the slab temperatures and then proposes a heat-transfer and moisture transport model to simulate the slab-moisture distribution. The environmental loadings are computed by uses of predicted temperatures and predicted moisture to evaluate the curling and warping of the slab. For the sake of simplicity, the computation considers only the stresses developed in joint plain concrete pavement slab and treats the slab as a beam that has visco-elastic, drying-creep behaviors.

Other than the environmental loadings, the sensitivity of the local weather conditions to the slab-moisture and -temperature distributions are also of the dissertation's concern. The dissertation investigates the role of air temperature, wind speed, and solar radiation on the slab temperature; it assesses the influence of the wind speed, local annual rainfall distribution, and air relative humidity on the slab-moisture distribution.

The dissertation contains 9 chapters. Chapter 1 presents the research significance regarding the models to predicted slab moisture and slab temperature and also reviews the literatures relative to this modeling. Chapter 2 develops a model to simulate the slab temperature distribution. Chapter 3 investigates the impact of air temperature on the temperature profile of in-service pavement slabs. This chapter has been published in *Construction and Building Materials*, with my advisor Jacob E. Hiller as the co-author. The author keeps only his contribution and removes the contribution of the co-author. The copyright permission is attached in **Appendix A**. Chapter 4 focuses on roles of wind speed on the slab-temperature development and on formulation of the slab-surface heat convention coefficient. Chapter 5 examines the impacts of the solar radiation and the pavement albedo on the slab-temperature distribution. This chapter has been approved by *KSCE Journal of Civil Engineering*, with my advisor Jacob E. Hiller as the co-author. It only presents the contribution of the author. The copyright permission is attached in **Appendix B**. Chapter 6 proposes a model to simulate the moisture distribution through in-service slab. Chapter 7 characterizes the sensitivity of slab moisture to roles of rainfall pattern, wind speed, seasonal air RH, daily variation of RH, water-to-cement ratio, treatment of the upper boundary, etc. Chapter 9 draws the conclusions from the dissertation and proposes the future works to build upon works from this dissertation.

Yinghong Qin
June 16, 2011

Acknowledgement

I am indebted to my advisor Dr. Jacob E. Hiller for his funding support, his gentle leadership, and his meticulous guidance during my research. It is an honor to be his student. I also extend my thanks to my committee members, Dr. Zhanping You, Dr. Devin Harris, and Dr. Gregory M. Odegard, for taking time to review this work.

Thanks to all of the students, staffs, and faculties in the Department of Civil and Environmental Engineering. The atmosphere of academic excellence and academic collegiality fostered in the department played a crucial role in my productivity and my enjoyment during my PhD program. Karl Peterson, Qingli Dai, Yogini Deshpande, Yue Li, Yu Liu, Rita Lederle, Cory Shorkey, Robert Lothschutz, Haizhu Lu, Shu Wei Goh, Hui Yao, Yongliang Jin, Andrew Walter, Abdul Koroma have provided specific helps. Helps from Dr. Haiying Wang and Dr. Spandan Maiti also are greatly appreciated.

Thanks to my friends Chen Liao, Xiaoxue Liao, Wen Lu, Nan Ding, Rong Liu, Liu Chen, Rui Yan, Wei Chen, etc. Our meeting time is a special moment that brings pleasure into my daily life and draws me out of the seemingly endless research time. My PhD studies may have deterred without your enthusiasms. Supports from my roommates Andy Drew and Jing Liu can never be underestimated either.

Thanks to my whole family: my parents, two brothers, two sisters, two sisters-in-law, and two brothers-in-law. You are always a part of my life. Your unyielding support supply endless energy to pursuing my PhD at Michigan Tech. Special thanks to my friend Pei Tang. You treat me as one of your brothers. You give me unselfish support in both my daily life and my research program. You are my best friend at Michigan Tech. Thanks also to my friend Fanghua Li for her understanding and encouragement.

Sincerely,
Yinghong Qin

Abstract:

In-service hardened concrete pavement suffers from environmental loadings caused by curling and warping of the slab. Traditionally, these loadings are computed on the basis of treating the slab as an elastic material, and of evaluating separately the curling and warping components. This dissertation simulates temperature distribution and moisture distribution through the slabs by use of a developed numerical model that couples the heat transfer and moisture transport. The computation of environmental loadings treats the slab as an elastic-viscous material, which considers the relaxation behavior and Pickett effect of the concrete.

The heat transfer model considers the impacts of solar radiation, wind speed, air temperature, pavement slab albedo, etc. on the pavement temperature distribution. This dissertation assesses the difference between documented models that aim to predict pavement temperature, highlighting their pros and cons. The moisture transport model is unique for the documented models; it mimics the wetting and drying events occurring at the slab surface. These events are estimated by a proposed statistical algorithm, which is verified by field rainfall data. Analysis of the predicted results examines on the roles of the local air RH (relative humidity), wind speed, rainy pattern in the moisture distribution through the slab. The findings reveal that seasonal air RH plays a decisive role on the slab's moisture distribution; but wind speed and its daily variation, daily RH variation, and seasonal rainfall pattern plays only a secondary role.

This dissertation sheds light on the computation of environmental loadings that in-service pavement slabs suffer from. Analysis of the computed stresses centers on the stress relaxation near the surface, stress evolution after the curing ends, and the impact of construction season on the stress's magnitude. An unexpected finding is that the total environmental loadings at the cyclically-stable state divert from the thermal stresses. At such a state, the total stress at the daytime is roughly equal to the thermal stress; whereas the total stress during the nighttime is far greater than the thermal stress. An explanation for this phenomenon is that during the night hours, the decline of the slab's near-surface temperature leads to a drop of the near-surface RH. This RH drop results in contraction therein and develops additional tensile stresses. The dissertation thus argues that estimating the environmental loadings by solely computing the thermally-induced stresses may reach delusive results. It recommends that the total environmental loadings of in-service slabs should be estimated by a sophisticated model coupling both moisture component and temperature component.

Chapter 1 Introduction

1.1 Motivation

Environmental loadings develop through in-service concrete pavement slabs, even if the slab is not open to traffic. These stresses are due to differential profiles of temperature and moisture through the slab (Yang H. Huang 2004; MEPDG 2004). Non-uniform temperature profiles through a slab lead to the curling of pavement slab. They produce curling stress because the curling is restrained by the pavement shoulder or adjacent lanes, slab's self weight, base, etc. Moisture gradients across the slab result in differential shrinkage between the top and bottom of the pavement. The mechanism of stress caused by this slab deformation is similar to curling, but are termed warping stresses. The combination of the curling and warping stresses, in some cases, can be high enough such that the concrete slab cracks before the pavement slab is exposed to any traffic loading (Heath et al. 2003).

Curling stresses experience both diurnal and seasonal cycles. Diurnally, temperature distributions in a pavement slab depend primarily on the heat flux at the top of a pavement slab because the slab surface area experiences higher heat flux than its depth. During daytime, the solar radiation heats up the pavement surface whereas the remaining portions of the slab remain relatively colder. This different thermal condition leads to differential deformation across the slab. It generates compressive stress at the top and tensile stress at the bottom. At nighttime, both heat convection and thermal irradiation dissipate the absorbed solar radiation and make the near surface colder but the deeper slab relatively warmer. This temperature difference creates tensile stress at the top and compressive stress at the bottom. Seasonally, the daily peak solar radiation arriving at the earth surface follows a pattern ranging from nadir in December to a peak value in July. The pattern means that a relatively sharper temperature gradient develops through the slab during the summertime and a relatively gentler temperature gradient, during the wintertime. Curling stresses during the summertime are thereby higher than that during the wintertime. The seasonal solar radiation pattern also results in heat storage under the slab during warmer seasons and in heat dissipation during colder seasons. This seasonally-cyclic heat storage and heat dissipation influences the temperature at the bottom of a slab and affects the non-linearity of the slab-temperature profile through its depth. The curling stress developed in a pavement slab thus undergoes both daily and seasonal cycles

The warping stress varies irregularly, strongly depending on the local weather conditions. Moisture profiles cause warping (shrinkage) stresses due to their non-uniformity through the depth of the slab. Unlike the variation pattern of slab's temperatures, the slab-moisture profile is seldom affected by the daily variation of the ambient air RH. This is because the moisture diffusivity of a slab is several orders of magnitude lower than the thermal diffusivity. The slab moisture profile depends on the ambient air RH, wind speed, local rainfall, slab's diffusivity, etc. Such dependencies determine that the slab's internal RH varies primarily near the top whereas the lower

portions of a slab's volume remains close to a saturation level, generally greater than 80% RH (Chunqiu Li et al. 2008a). This differential slab-temperature distribution results in a differential shrinkage within a slab. The shrinkage is also restrained by the self weight of the slab, friction of the base, the compatibility of the slab's element, etc, leading to bending stresses. Development of these stresses is relatively complicate because the shrinkage depends not only on the pore RH and its gradient through the slab but also on the age of the concrete. This time-dependent nature of concrete deformation has to be considered during the computation of the warping stresses since the rate of RH variation through a slab is slower than that of the temperature variation.

These curling and warping stresses introduce damage in rigid pavements. Since shrinkage causes significant stresses in the early age of the pavement, hairline cracking can possibly occur at the top and make the slab prone to continuous cracking after the slab is open to traffic. As time lapses, stress relaxation reduces the warping stresses; but the diurnal cyclic curling (thermal) stresses possibly remain significant enough to accelerate the fatigue damage of the slab (J.E. Hiller and Roesler 2010). The curling stresses do not considerably relax because they depend only on the shape of temperature profile, which relies on the thermal state of the slab and is not degraded as time elapse. These stresses greatly increase of the amount of bending stress through the slab. In the case of high bending stresses, the slab may lose the support of the underlying layers, directly leading to slab's cracking when a heavy traffics passes on the surface. A thorough study on the combined effect of curling and warping stresses necessitates.

1.2 Literature review

1.2.1 Temperature effects on rigid pavement slabs

1.2.1.1 In-situ and numerical investigations of temperature profiles

Experimental testing and numerical methods have been extensively used to study the temperature distribution within concrete slabs. In-situ measurements have been conducted to record the temperature profiles of rigid pavement slab. The recorded data is typically logged by thermocouples that are inserted at different depths to monitor the temperature distribution through the slab (Richardson and Armaghani 1987; Yu et al. 1998; Jeong and Zollinger 2005). This data is accurate for short-term readings, but may lead to significant errors due to the zero drift of the thermocouples for long-period measurements. Also, extrapolating this data to other sites can be delusive because in-situ observations cannot cover all the site-specific conditions influencing heat transfer between the slab and the surrounding environment (Richardson and Armaghani 1987; Ashraf Mohamed and Hansen 1997; Yu et al. 1998). Numerical models are thus popular to simulate the temperature through the pavement slabs (Liang and Niu 1998; Yavuzturk et al. 2005). These models usually treat the heat exchange between the pavement and the surrounding air as one-dimensional problem (Kapila et al. 1997; Bentz 2000; Minhoto et al. 2005). This treatment is reasonable because the width and length of the slab is orders of magnitude greater than the thickness of the slab. Temperature distribution through the

slab depends primarily on the adoptions of upper- and lower-boundary conditions. The upper boundary is treated as a heat-flux boundary. The flux comes from the solar radiation, thermal irradiation, and convection. It depends on wind velocity, solar absorption, air temperature, roughness of pavement surface, etc. The lower boundary is set as either an adiabatic boundary condition (Figure 1.1b) or a Dirichlet boundary condition (Figure 1.1a) (Minhoto et al. 2005; Yavuzturk et al. 2005), where the temperature is assumed as a constant (Liang and Niu 1998; Bentz 2000).

Documented one-dimensional heat models need improvement because the denoted boundary conditions are inadequately addressed. At least two limitations exist at the specified upper boundary condition. First, methods used to compute the heat convection coefficient needs refinement. This coefficient is mainly determined by the local wind speed. For instance, the heat convection coefficient is assumed to increase with the wind velocity following a 0.7 power-law in Enhanced Integrated Climatic Model (EICM), a sub-model embedded in the Mechanistic-Empirical Pavement Design Guide (MEPDG). This increasing rate goes against the accepted heat transfer theory (Jiji 2009). According to this theory, this coefficient should be a function of the Reynolds and Prandtl numbers of the ambient air (Kapila et al. 1997; Jiji 2009). Second, input of the incoming solar-radiation peak value to the heat transfer model needs a process for refined estimation. Currently, the EICM model allows repeated uses of one-year observed solar radiation when a long-term temperature prediction is conducted (MEPDG 2004). This repeated use overlooks the heat history development of the slab.

Limitations also exist at the specified lower boundary condition of the documented models. The lower boundary condition is usually assumed to either be a constant temperature (Bentz 2000) or be null heat flux (Yavuzturk et al. 2005). On one hand, the longer period waves of the seasonal temperature cycle are neglected if the bottom of a pavement is regarded as a fixed temperature boundary. On the other hand, the shorter period of diurnal temperature cycle goes unaccounted if the bottom of the pavement is seen as a null heat flux bottom. For instance, a sunny day predated by a cloudy day could result in a positive heat budget to the ground; a null heat flux at the bottom of the pavement fails to mimic this positive budget. Actually, the deep ground under the pavement structure is a boundary with neither a fixed temperature nor a null heat flux. Temperature variation beneath the pavement slab decreases as depth increases, according to the extenuating characteristic of the ground temperature profile. Thus there exist a depth below which soil temperature maintains a constant value (Andersland and Ladanyi 1994). This depth is a site-specific condition and is also affected by the net heat flux at the pavement surface. An artificial denotation for this depth potentially results in an improper prediction of the pavement slab's temperature.

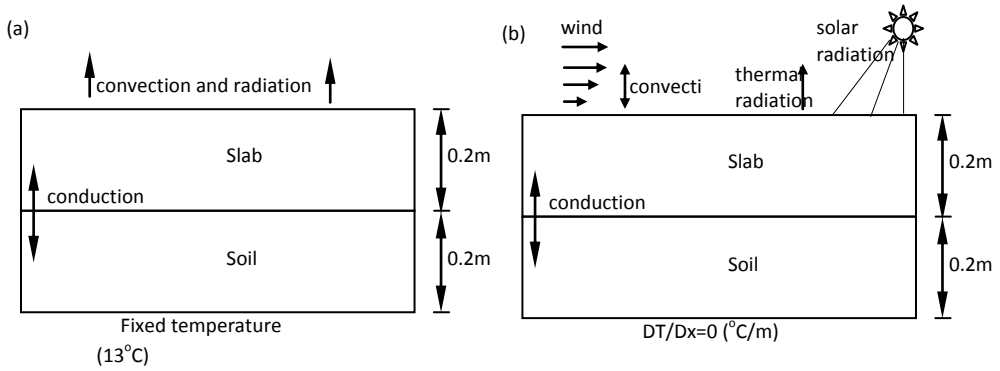

Figure 1.1 One-dimensional heat transfer models for concrete pavement; a) After Bentz (2000), b) After Yavuzturk (2005).

1.2.1.2 Temperature induced stresses

Thermally-induced stresses developed through concrete slabs were first addressed by Westergaard (Westergaard 1927). His assumption of a linear gradient through the depth of the slab had been extensively used to estimate the curling stresses of curled concrete pavements (Tianxi Tang et al. 1993; Papagiannakis and Masad 2007). His solution to the thermal stress across a concrete slab with finite dimensions was popularized by Bradbury (1938). Bradbury presumed the linear distribution of temperature through a slab. In his solution the thermal stresses developed in a slab can be definitively calculated once the temperatures at the top and bottom of slab are obtained. However, later researchers noted that the temperature distribution through a pavement slab can be highly non-linear (Armaghani et al. 1987; Thompson et al. 1987; Ashraf Mohamed and Hansen 1997). The non-linearity is because the near-surface temperature is easily affected by the heat flux at the top whereas the internal portions of slabs exhibit relatively less fluctuation.

The stresses induced by the non-linear temperature profiles were first addressed by Thomlinson (Ioannides and Khazanovich 1998). Thomlinson's work subdivides the total thermal stress into three parts: stress induced by the uniform temperature; stress due to a linear temperature gradient; stress caused by the "internal force" as shown in **Figure 1.2**. The stress induced by the uniform temperature causes an expansion or a contraction of the slab because of the restraints from the underlying layer's friction and from the neighboring slabs' constraint. The stress due to a linear temperature gradient through the slab thickness is restrained by the slab's self weight, the underlying layer's friction, and external loads. The stress caused by the "internal force" is because the non-linearity of temperature distribution exerts an internal force to neighboring elements to satisfy compatibility requirements. This "internal force" contributes either a tensile or a compressive stress to the slab. The specific internal force is a function of the location through the depth of the slab. The stress caused by this force is self-equilibrating stress. It is significant enough that it should not go unaccounted.

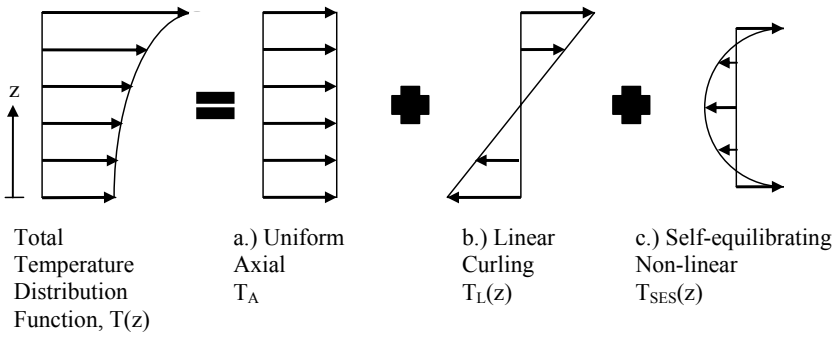

Figure 1.2 The components of the total temperature-induced deformation.

Methods used to compute the self-equilibrating stress have been well documented. Main difference between these methods lies on the use of either a quadratic or cubic polynomial to approximate the temperature profile (Richardson and Armaghani 1987; Solaimanian and Kennedy 1993). By assuming the temperature profile followed a quadratic relationship, Hiller and Roesler (J.E. Hiller and Roesler 2008) developed a simplified method to capture the self-equilibrating stress on the performance of rigid pavement by using a single parameter named NOLA (NOn-Linear Area). This method is simple and can link the NOLA to the self-equilibrating stress. Fatigue induced by the thermal stresses also can be estimated based on the NOLA. Mohamed and Hansen (1997) computed self-equilibrating stress by using an proposed theoretical algorithm that the temperature profile is fitted by polynomial of the third degree. Although the third-order polynomial generally provides a better fit than a quadratic function, the non-linearity cannot be captured within one single term such as NOLA.

Whatever the methods to compute the thermally-induced stress, the computation has always been based on the elastic theory in rigid pavement structures. It has not considered relaxation behavior of the thermally-induced stress developed through the depth of in-service concrete slabs. Although this stress depends primarily on the temperature profile and less on the stress history, the stress relaxation potentially reduces the development of the compressive stress near the top whereas increasing the tensile stress at the bottom. This is because during daytime a relatively sharper positive gradient is developed within the slab, resulting in the daily maximum-compressive stress appearing at the top. Conversely, the stresses developed during nighttime are relatively gentler. Cycles of this stress pattern can lead to a compressive creep at the top and tensile creep at the bottom. Relaxation behavior of concrete thus may need to be considered when the thermal stresses developed through a slab are estimated.

1.2.2 Moisture and moisture distribution

Moisture distribution within concrete slabs and the resulting warping stresses have been extensively investigated. In-situ investigations have shown that the moisture gradient varies significantly to a depth of approximately 2 inches, whereas the deeper portions of pavement slab remain at approximately 80% percent of saturation or higher

(Philip and Vries 1957). Numerical studies concerning both drying shrinkage and creep behavior of concrete have gained a great deal of attention, driven by the need to quantify the long-term deformation and stability of nuclear reactor containments (Bazant and Najjar 1971; Bazant 1983; Bazant and Prasannan 1988; Bazant 1998; Shah and Hookham 1998; Witasse et al. 2002). Nevertheless, limited numerical studies center on the moisture profile through pavement slabs and on the subsequent stresses caused by the moisture profile. Typically, moisture gradients in concrete pavement generate differential shrinkage between the top and bottom of pavement. They lead to warping stresses in which the top of pavement is in tension but the bottom is in compression for a vast majority of time (Janssen 1987).

1.2.2.1 Laboratory and field tests for moisture distribution within concrete slab

Moisture distribution through a concrete specimen in a laboratory environment is typically measured by RH probes that are inserted into concrete to record the internal moisture (Andrade et al. 1999; Jin-Keun Kim and Lee 1999). The air RH of the lab environment is the decisive factor determining the moisture distribution through the slab (Z. Bažant and Najjar 1972). Moisture content across the field concrete slabs is typically recorded by the psychrometers that are installed in pavement sections to read the RH of pavement slabs (Janssen 1987; Kohler 2005). The intake and outtake of moisture of pavement is primarily controlled by the wetting (absorption dominant) and drying cycles at the surface of the pavement (Hanzic and Ilic 2003; Chunqiu Li et al. 2008b). Unlike many other concrete structures, the unique geometry of a pavement slab defines that the moisture intake and evaporation is almost always through the slab surface.

To better estimate the moisture distribution with concrete, laboratory studies have been extensively conducted to investigate the diffusivity of the concrete. The factors influencing the diffusivity can be categorized into both internal and external factors. For the internal factor, the diffusivity is mainly controlled by the concrete porosity, which is linked to the water/cement ratio and permeability of concrete. For the external factor, the diffusivity strongly depends on internal pore RH. An interpretation to this dependency is that moisture migrates under capillary force at high pore moisture content but transports under gas pressure at lower pore moisture content (Bazant 1998). Temperature also has been found as an external factor impacting the diffusivity of concrete (Wong et al. 2001; Jooss and Reinhardt 2002). Wong (2001) investigated the diffusivity of concrete at the saturation state, D_{sat} , and found that temperature strongly influenced concrete's diffusivity. For instance, D_{sat} increases approximately 6-8 times when temperature increases from 20 to 40 ^{o}C, thereby affecting moisture transport more effectively during warmer months for many climates.

1.2.2.2 Numerical study of the moisture transport within concrete slab

Numerical simulations have been extensively conducted to study the moisture transport within concrete (Z. Bažant and Najjar 1972; Xi et al. 1994; Bazant 2001). The crux of the simulation is to properly estimate the diffusivity, which depends on the

moisture content of concrete, porosity of concrete, internal temperature distribution, etc. (Z. Bažant and Najjar 1972). For in-service concrete slabs, another crux lies on wetting/drying cycles. Moisture gain of an in-service slab is controlled by the wetting cycle at which the absorption is dominant. Moisture loss is determined by the drying cycle. This process depends highly on the RH of the ambient air (Šelih et al. 1996; Grasley et al. 2006) and the wind velocity at the ground surface.

Models used to predict the moisture profile through slabs need improvement for two reasons. First, currently most models are based on isothermal conditions. This is the case because other structures, unlike pavement slabs that are directly exposed to sunlight, experience lower temperature cycles. It is also because the temperature regimes of these structures become relatively steady soon after (1 or 2 days) the structure is built. For in-service slabs, their diurnal temperature variation, however, may significantly affect moisture migration within the slab because the concrete's diffusivity varies with temperature (Jooss and Reinhardt 2002). Secondly, the denotation of the upper boundary condition needs a refined specification. Bazant and Raftshol (1982) experimentally investigated the drying shrinkage of specimens and suggested that the upper boundary could be set as the RH of the ambient air. This setting is the case for the laboratory specimens that do not experience wind effects. However, this assumption overlooks the surface moisture emissivity of concrete. The emissivity depends on several factors including air velocity, porosity, surface roughness, etc. (Torrenti et al. 1999; Yuan and Wan 2002). The impact of these factors on the moisture distribution within an in-service slab should be wisely considered because pavements experience varying wind speeds in all climatic regions.

1.2.3 Coupled heat transfer and moisture transport

Models coupling heat transfer and moisture transport have been proposed to predict the moisture distribution within concrete structures (Bazant 1970; Kapila et al. 1997; Burkan Isgor and Razaqpur 2004). The phenomena relevant to moisture, pressure, and temperature distributions are coupled by the assumption that moisture distribution affecting the temperature regime is neglected. The driving force for the moisture transport within concrete consists of moisture gradient, pressure gradient, and temperature gradient (C. L. D. Huang et al. 1979; Hall 1989). Numerical results show that the porosity of concrete dominates the moisture transport within concrete (Wong et al. 2001). Nevertheless, none of these models were designed to predict the moisture distribution of pavement slabs. Burkan's model (2004) commissions to compute the carbonation process of concrete structures. Kapila's work (1997) aims at predicting the moisture distribution within early-age hydrating concrete. Very few studies have been conducted to investigate the coupled heat transfer and moisture transport through in-service concrete pavements and then to compute the environmental loading-induced stresses through the slab. With the thermal and moisture-induced stresses in concrete pavements constituting a large percentage of stress development due to its geometry, this

is a critical task to undertake to better predict the service life of these pavements ultimately.

These environmental loading-induced stresses are seldom investigated because of three reasons. First, it is difficult to separate the curling stresses and warping stresses from the total stress measured in field. This difficulty suggests that even though a model may be sophisticated enough to predict the thermal- and moisture-induced stresses in other structures, its reliability to predict the environmental loadings in a pavement is almost unverifiable. Secondly, the occurrence of micro-cracking and creep in the concrete significantly relaxes the stresses (Yang H. Huang 2004). The stress relaxation encumbers a prediction attempting to capture the coupled impact of moisture and thermal gradients on the stresses development. Finally, occurrence of wetting and drying cycles at the pavement surface remains uncertain to experts in pavement science. Modeling of the impact of these cycles on the pavement moisture budget is still conducted by use of artificial fixed wetting period, such as 15 or 30 days (Chunqiu Li et al. 2008a; Kefei Li et al. 2009).

1.3 Critical appraisal

Four main limitations, at least, exist in the current documented numerical models that aim to predict the heat transfer and moisture transport within concrete pavements.

- The thermal history of both the pavement slab and the underlying layers is not considered. Currently the prediction for the pavement temperature profile usually considers only the thermal interaction between the pavement and the subbase (Bentz 2000; Yavuzturk et al. 2005). In fact, the temperature profile of the subgrade, usually 10m or even deeper beneath the pavement surface, varies seasonally (Ladanyi 1994) because the seasonal temperature wave propagates deeper than the diurnal temperature cycle (Pollack and Huang 2000). Without considering the thermal history of the underlying layers potentially leads to an unreliable prediction of the pavement temperature.
- The boundary condition at the bottom of the computational domain is improperly specified. Documented models assume that the temperature at the bottom of the subbase or base is either a constant (Bentz 2000) or an adiabatic boundary (Yavuzturk et al. 2005). This assumption results in considerable error because a geothermal gradient exists at the deep ground (usually 10-20m) beneath the pavement surface (Ladanyi 1994; Liang and Niu 1998).
- Currently, the moisture transport model used to predict the moisture distribution within pavement slab is based on isothermal conditions (Jin-Keun Kim and Lee 1999; Leivo and Rantala 2005; Chunqiu Li et al. 2008a). The effect of the temperature on the diffusivity of the concrete goes unaccounted.
- The moisture gain and loss at the pavement surface needs more refined specification. Documented models usually overlook the impact of wind velocity on the moisture loss at the slab and neglect the influence of wetting/drying cycles on the

moisture gain at the surface. For a specific region, such cycles should be determined by the local seasonal rainfall distribution and should have a probabilistic distribution.

1.4 Objectives

This dissertation numerically investigates the coupling heat transfer and moisture transport within a concrete slab and evaluates the warping and curling of concrete pavement slab. Its goals consist of three parts:

- The first part develops a proposed heat transfer model to characterize the impacts of air temperature amplitude, solar radiation, slab-surface solar absorptivity, and wind velocity on the temperature distribution within pavement slabs. It verifies the feasibility of the proposed model by use of field slab temperatures. The subsequent analysis highlights the difference between the proposed model and the documented models, and compares the predicted reliability of these models.
- The second part develops a moisture transport model to predict the moisture distribution through in-service slabs. It proposes a straightforward algorithm to simulate the wetting and drying events and validates the algorithm by use of field observations concerning the local rainfall distribution. It utilizes both laboratory observed data to verify the prediction of the proposed moisture transport model. The associated discussion centers on the effects of the wetting/drying cycle and ambient conditions, e.g. wind speeds and air relative humidity, on the slab moisture distribution.
- The third part characterizes the curling stress, warping stress, and the combination of them by using a model that considers creep, autogenous shrinkage, and drying shrinkage of JPCP slab. It also estimates the evolution of the warping stresses during the expected service period of the pavement, especially at early ages of the concrete slabs. It computes the total environmental loadings that in-service slabs suffer from. The computation considers both the stress relaxation and Pickett effect of concrete slabs. The analysis to the developed total stress focuses on the impact of wind speed, air RH, stress evolution, construction season, and pavement location on the magnitude of the stress.

1.5 Organization

The dissertation has 9 Chapters as described below.

Chapter 2 develops a model to simulate the temperature distribution through in-service slabs. The model accommodates the roles of air temperature, solar radiation, wind speed, dew point, etc on the heat exchange between the slab and the surrounding environment. Both short- and long-term field temperature observations are used to verify the model. Numerical code for this simulation can be referred to **Appendix C**.

Chapter 3 investigates the impact of air temperature on the temperature profile of in-service pavement slabs. It centers on the impacts of daily temperature swing on the temperature variation of the slab. It studies whether the replacement of the observed air

temperature with the sinusoidal-approximated air temperature compromises the predicted temperature.

Chapter 4 focuses on roles of wind speed on the temperature development of a slab and on formulation of the heat convention coefficient at the pavement surface. It investigates the degrees that wind speed reduces the pavement temperature gradient. Considering that this formulation determines the heat convention coefficient, this chapter highlights the difference between the documented models used to compute the coefficient. It emphasizes that the use of the EICM model potentially results in the predicted temperature being insensitive to wind speed because this model greatly underestimates the heat convection coefficient.

Chapter 5 examines the impact of the solar radiation and the pavement albedo on the temperature distribution through in-service pavement slabs. It considers both the probabilistic and deterministic portions of the solar radiation. It examines the impact of different site-specific sunrise/sunset time models on the temperature prediction. It centers on whether the heat history affects the temperature distribution and thermal-stress development of the slab.

Chapter 6 proposes a model to simulate the moisture distribution through in-service slab. It develops an algorithm to evaluate the wetting and drying events occurring at the pavement surface. It uses both field data and lab data to verify the model and proposes a formulation that characterizes the moisture evaporation rate during the drying events. Numerical code for this simulation can be referred to **Appendix D**.

Chapter 7 characterizes roles of rainfall pattern, wind speed, seasonal air RH, daily variation of RH, water-to-cement ratio, treatment of the upper boundary, etc on the moisture prediction through in-service slabs. The associated analysis focuses on the different roles between these factors. It also examines the mechanisms that some environmental factors play as decisive role on the slab moisture distribution whereas others act only in a secondary role.

Chapter 8 computes the total environmental loadings that in-service slabs suffer from. Numerical code for this simulation can be referred to **Appendix E**. The computation method considers both Pickett effect and stress-relaxation behavior of the concrete slab. The analysis to the computed stress concentrates on the evolution of the stress after the curing ends, on the long-term stress development, and on the impact of construction season upon the stress developed. The subsequent discussion primarily concerns whether the total stress at the stable state (moisture loss balances the moisture gain) converges to the thermally-induced stress.

Chapter 9 draws the conclusions from the dissertation and proposes the future works to build upon work from this dissertation. It discusses the implications of the conclusions to the elongation of the rigid pavement performance and summarizes the limitations of the dissertation. Future work is expected to study the built-in curling; the stress-softening at the post-failure state; fatigue damage of rigid pavements; and the moisture soaking at the pavement surface during wetting events.

Chapter 2 Model development and verifications

Prediction of the pavement temperature ties to both the estimate of the maximum pavement surface temperature and the computation of the thermally-induced stress developed through a slab. Numerical models have been extensively conducted to predict the temperature distribution through in-service concrete pavement slabs. These models require improvements in the treatment of the lower boundary condition and in the computation of the heat convection coefficient.

This chapter proposes a new heat transfer model to simulate the pavement temperature through the depth of the pavement structure. The model specifies a geothermal gradient to the deeper soil (20m in depth). It uses the accepted heat transfer theory to estimate the heat convection coefficient at the pavement surface. Both short- and long-term field temperature observations are used to verify the reliability of the model.

2.1 Numerical simulation of the temperature regime of pavement slab

Pavement temperatures are mainly controlled by the heat flux at the top because the width and length of a pavement slab is far greater than the thickness. A one-dimensional heat transfer model is thus adequate to predict the temperature distribution of a slab and its underlying layers. To simplify the model, the following assumptions are made:

1) Heat conduction dominates heat transfer process in the pavement structure and the underlying layers. The heat convection within the ground and the pavement slab is neglected;
2) Occurrence of moisture transport beneath the slab does not significantly affect the thermal properties of the underlying layer. Temperature variation does not lead to the variations of the thermal conductivities, heat capacities, and densities of the pavement and the underlying layers.

Heat flux at the upper boundary consists of the solar radiation, convection, irradiation, and emissivity occurring at the pavement surface (Figure 2.1). The temperature at deep ground is mainly affected by the heat flux from the interior of the earth. It exhibits less variation. The depth of zero annual temperature amplitude ranges approximately from 10 to 20m below the ground surface (Andersland and Ladanyi 1994), depending on the site-specific condition. This study selects 20m beneath the bottom of the pavement's base layer as the lower boundary, in order to avoid that this depth is lower than the bottom of the computational domain.

2.1.1 One-dimensional heat transfer model

The temperature T of the media (the pavement slab and the underlying layers) can be described by the Fourier Equation:

$$\rho c \frac{\partial T}{\partial x} = div(k \cdot grad(T) + q_{hydra} \tag{2.1}$$

where k (W/m^oC^{-1}) is the thermal conductivity of mediums; ρ (kg/m^3) and c (J/kg/ºC) are the density and the heat capacity of mediums, respectively; q_{hydra} (W/m^{-2}) is the internal heat generation rate, for hardened concrete,q_{hydra} =0. The thermal capacity, density, and thermal conductivity of concrete have been well documented by previous researchers (Khan 2002; Kook-Han Kim et al. 2003; Chung and Shin 2008). These properties depend on concrete mixture characteristics, e.g., water-to-cement ratio, aggregate type, aggregate volume, and porosity of the concrete. Detailed values are site-specific and reasonably controllable parameters. Table 2.1 tabulates the assumed parameter values and typical ranges of these parameters.

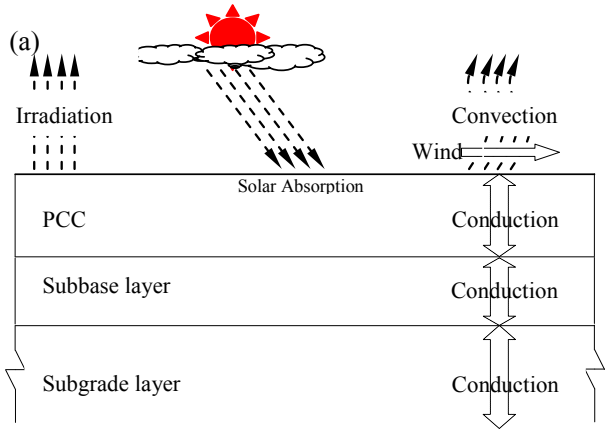

Figure 2.1 A schematic show for the heat transfer model.

Table 2.1Thermal parameters of the pavement and underlying layers

Stratum	k ($W\cdot K^{-1}\cdot m^{-1}$)	c ($KJ\cdot kg^{-1}\cdot K^{-1}$)	ρ(kg/m^3)
Slab[a]	2.5 (1.5-3.5)	1.0 (0.84-1.17)	2350 (2200-2400)
Asphalt base[b]	1.8 (1.5-2.0)	0.9 (0.9-1.3)	2210 (2297-2425)
Gravel subbase[c]	1.8 (1.5-1.8)	0.9 (0.7-0.9)	2210 (1792-2405)
Subgrade[d]	1.5 (0.5-2.0)	0.86 (0.8-0.9)	1560 (1380-1600)

Note: Values within the bracket are a rough range of the medium's thermal properties; the exact value is site-specific. [a](Morabito 2001); [b](Luca and Mrawira 2005); [c](Jean and Jean-Marie 2005); [d](Lu et al. 2006); Density for subgrade is dry density.

2.1.2 Heat flow at the pavement surface

Heat flux at the pavement surface is affected by factors including the surrounding air temperature, dew point, wind velocity, etc. These factors are available at the National Oceanic and Atmospheric Administration (NOAA) database.

2.1.2.1 Thermal irradiation

Thermal irradiation is a long-wave heat fluxes between the natural ground surfaces and the sky. The total irradiation emitted, q_{irr}(W/m^2), follows the Stefan-Boltzmann law and usually is expressed as:

$$q_{irr} = \varsigma \times \varepsilon \times (T_{sky}^4 - T_s^4) \tag{2.2}$$

where T_s is slab-surface temperature, (^{o}K). $\varsigma(Wm^{-2}K^{-4})$ is the Stefan-Boltzmann constant; $\varsigma = 5.669 \times 10^{-8}$; T_{sky}(^{o}K) is the effective sky temperature (effective sky temperature is the temperature of blackbody radiation having the same flux as the downward atmospheric radiation and is not equal to air temperature); and ε is the ground surface emissivity. $\varepsilon = 0.90$ is used in this study and others (Kapila et al. 1997; Rohsenow et al. 1998) when evaluating pavement temperatures. T_{sky} can be evaluated by Eq.(2.3):

$$T_{sky} = \varepsilon_{sky}^{0.25} \times T_a \tag{2.3}$$

where T_a (^{o}K) is air temperature; ε_{sky}, the sky emissivity, is given by Tang *et al*(Runsheng Tang et al. 2004):

$$\varepsilon_{sky} = 0.754 + 0.0044T_{dp} \tag{2.4}$$

where T_{dp} is the dew point.

The local dew point can be approximated using the following formula:

$$T_d = b\gamma(T, RH)/[a - \gamma(T, RH)] \tag{2.5}$$

where $a = 17.3$, $b = 237.7^oC$, and $\gamma(T, RH) = aT/(b + T) + ln(RH/100)$.

2.1.2.2 Convection

Heat convection at the pavement surface is given by:

$$q_{conv} = h_{conv}(T_a - T_s) \tag{2.6}$$

where h_{conv} is the convection coefficient, W/m^{o}C^{-1}. h_{conv} is a function of the local Reynolds number Re, the thermal conductivity of the air K_{air} (W·K^{-1}·m^{-1}), the air's Prandtl number Pr, and the characteristic length of the medium where wind blows upon. According to traditional heat transfer theory (Rohsenow et al. 1998; Jiji 2009), h_{conv} consists of two parts: free and forced convections. The heat convection coefficient of free air convection on a flat plane is approximately 5.6 W/m^{o}C^{-1} (Jiji 2009). According to the Blasius solution (Jiji 2009), the coefficient of a forced convection on a flat plane is $0.332Re^{0.5}\,Pr^{1/3}\,K_{air}/L$ if the airflow is at low speed (e.g.<=6m/s). In this study, the Blasius solution is modified by combining the heat convection coefficients at free and forced convections. Therefore, the heat convection relationship developed in this study is expressed as:

$$h_{conv} = 5.6 + 0.332Re^{0.5}\,Pr^{1/3}\,K_{air}/L \tag{2.7}$$

where for the air, $K_{air} = 0.027, Pr = 0.7$. For the airflow upon an infinite flat plate, $L = 0.15$m. The Reynolds number Re is:

$$Re = wL/\upsilon \tag{2.8}$$

where w is the local wind velocity, υ (m^2s^{-1}) is the air's kinematic viscosity and usually is $16.01*10^{-6}$ (m/s) .

2.1.2.3 Radiation

Solar radiation propagates energy as a short wave arriving at the ground surface. McCullough and Rasmussen (1999) proposed the following formula for the short-wave absorption of solar radiation q_{abs} (W/m^2):

$$q_{abs} = \gamma_{abs} \times I_f \times q_{solar} \tag{2.9}$$

where γ_{abs} is the surface absorptivity (SA)--or 1- the albedo of the surface; I_f is the intensity factor counting for the sun's angle during a 24-hour day; and q_{solar} is the peak value of the solar radiation during a-day period.

Solar absorptivity γ_{abs} relies on slab's surface color, concrete components, abrasion of the slab, etc. (Levinson and Akbari 2002). For concrete pavements, γ_{abs} ranges from 0.5 to 0.9 for new and older concrete, respectively. Considering a rigid pavement slab becomes darkened after opening to traffic, this paper uses $\gamma_{abs} = 0.85$ unless otherwise noted.

Solar radiation intensity factor I_f strongly depends on the atmospheric conditions, time of day, and incident angle of the sun's ray on the ground surface. During nighttime conditions, the solar radiation is negligible. During the daytime, I_f is assumed to follow a sinusoidal function (Bentz 2000; Ge 2005). It varies with the time of day and ranges from zero at both sunrise and sunset times to a peak value at midday. The sunrise time t_{sr}(hr) and sunset time t_{ss} (hr) can be computed by:

$$t_{sr} = 13 - 1/15 \times arccos(\theta) \tag{2.10}$$
$$t_{ss} = 13 + 1/15 \times arccos(\theta) \tag{2.11}$$

where θ is the hour angle. Eqs (2.10) and (2.11) are used during standard time (autumn and winter seasons), but during daylight savings times, the number "13" in both equations would be "12". To avoid confusion, this study uses standard time only. w_0 is calculated by:

$$w_0 = (sin(-0.83°) - sin\varphi sin\delta)/(cos\varphi cos\delta) \tag{2.12}$$

where $\varphi(°)$ is the latitude of the pavement site (positive in the northern hemisphere, negative in southern hemisphere), and δ (°) is the sun declination defined by:

$$\delta = 23.45sin\left(\frac{2\pi(284+DAY)}{365}\right) \tag{2.13}$$

in which DAY is the day of a year (January 1 is the first day, or $DAY = 1$).

The peak value q_{solar} of solar radiation depends on the sky conditions (e.g., cloud cover) and on the latitude of the pavement. Rather than providing daily detailed solar radiations, weather stations usually provide monthly maximum q_{max}, mean q_{mean}, and minimum q_{min} solar radiations (units: kWh/m^2/day). All of them are usually recorded by a flat-plate collector. Typically the observed data contains $\pm 9\%$ uncertainty. In this case, inputting the mean vallue to the heat transfer model overlooks the impacts of the maximum temperature and heat history on the pavement slab. Inputting solar radiations to a slab-temperature predicted model thus have to include the combination of the deterministic and probabilistic radiations. The deterministic portion reflects on the q_{mean}. The probabilistic portion fluctuates between the q_{max} and q_{min}, following a random normal distribution whose standard deviation depends on the uncertainty of the observation. Therefore, the q_{solar} to the heat transfer model is:

$$q_{solar} = 12 * \pi \times 41.67 \frac{q_{mean}+0.5(q_{max}-q_{min})*random(0,1)/1.38}{t_{sr}-t_{ss}} \tag{2.14}$$

where the random(0,1) produces a number according to the standard normal distribution; the denotation of the number 1.38 represents the level of uncertainty (9%) of the measurements (Patel and Read 1996); and the number 41.67 is the conversion factor from units kWh/m^2/day to W/m^2.

Therefore, the total heat flux q_{total} (W/m^2) at the pavement surface can be calculated as:

$$q_{total} = q_{conv} + q_{irr} + q_{abs}. \tag{2.15}$$

2.1.3 Heat flow at the deep ground

Temperature at the slab's bottom is not a constant but a variable. It depends on the boundary conditions at the pavement surface and on the physical properties of the underlying layers. At a certain point in deep ground, there exists a depth where the annual temperature amplitude is zero. This depth and its temperature are site-specific and thus are difficult to determine. However, for a specific site, the geothermal gradient at deep ground remains a constant (Andersland and Ladanyi 1994). Therefore, a geothermal gradient, usually 0.03°C/m (Goering and Kumar 1996), is denoted for the lower boundary condition of the computational domain shown in Figure 2.1. This geothermal gradient

adds another heat component to the underlying layers and keeps the deep ground thermal gradient, not the temperature magnitude, a constant.

2.2 Simulation information

The computational domain is discretized by 23 three-node elements, with 10 elements for the slab, 3 elements for base, and 10 elements for the subgrade. The slab has a thickness of 25.4cm (10inch). The base is assumed to be 10cm thick asphalt concrete. Time step size is 6 minutes to ensure the convergence of the simulation in realistic time. The cubic spline interpolation is used when an interpolation is needed. The initial temperature for the pavement structure and underlying layer is obtained by using the ground temperature profile from the preceding date. This date's temperature profile is gained by utilizing the local annual variation of ambient air temperature to simulate the ground temperature to a degree such that the temperature profile difference between this date and the same date in the previous year is less than 0.01°C. The Crank-Nicolson method is adopted to implicitly solve the differential Fourier equation in Eq. (2.1). Convergent tests are conducted to verify the accuracy of the results (Ainsworth and Oden 1997).

2.3 Model verification

Reliability of the proposed heat transfer model is verified by the documented data that was observed in the field. Whether the predicted temperature coincides with the monitored temperature of a slab is of primarily concern. However, usually the monitored temperature is a relatively short term data, e.g. 1 to 10 days. Agreement between the predicted and monitored temperatures does not necessarily mean a long-term predicted temperature would coincide with the field temperature of a slab. In this regard, this study also verifies the model using the field observations pertaining to both slab temperatures and the ground temperatures. Numerical code for this simulation can be referred to **Appendix C**.

2.3.1 Verification of the slab temperature.

Documented data presented in (Yu et al. 1998) are used to verify the propose heat transfer model. The data was measured from an in-situ pavement slab on I-70 on July 12, 1994. Climatic conditions are obtained from the NOAA database as input parameters for the model. The thermal properties, tabulated in Table 2.1 (the value outside the bracket), of the pavement slab and underlying layers are obtained from the United States Department of Agriculture (USDA) (USDA 2009).

The numerical results computed from the proposed heat transfer model coincide with the in-situ observed data (Figure 2.2). The maximum temperature difference between numerical result and in-situ observation is 2.5^{o}C, far lower than the error predicted in

documented literatures (Bentz 2000; Yavuzturk et al. 2005). The mean error and standard error are -0.17 ^{o}C and 1.24 ^{o}C, respectively.

The comparison in Figure 2.2 raises a question that if the variations of the thermal parameters of the slab or underlying layers leads to a different validation. To this question, I arrange the heat transfer equation such that the slab's thermal parameters (k, ρ, and c) are compacted to the thermal diffusivity, α(m^2/s). The arrangement turns Eq. (2.1) to Eq. (2.16):

$$\frac{\partial T}{\partial x} = div(\alpha \cdot grad(T) \tag{2.16}$$

where $\alpha = k/\rho c$.

The dependence of the slab temperatures on thermal diffusivity thus can be used to investigate the sensitivity of the slab-temperature prediction to the thermal parameters in Table 2.1. This is because heat transfer model is a boundary-value problem in which most heat flux comes from the slab surface. The dependency can be estimated by using the maximum-, mean-, minimum-thermal diffusivities to simulate the slab temperature, respectively. These three diffusivities are tabulated in Table 2.2, which is computed by use of the thermal parameters in Table 2.1.

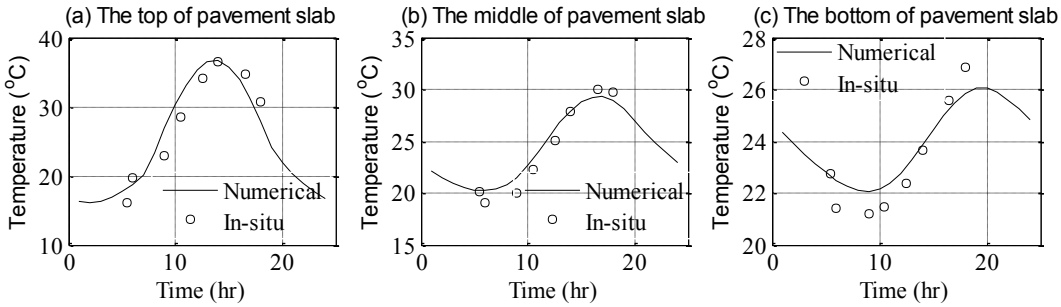

Figure 2.2 Predicted versus in-situ observed temperature (dotted data reproduced from Yu et al. (1998). Note: air temperature is 19.8oC; daily peak value of the solar radiation is 630 W/m2; daily air temperature amplitude is 9.0oC; daily wind speed is 3m/s; the slab' thickness is 12inch therein.

The prediction confirms that the variation of the thermal diffusivity affects on the slab temperature prediction indiscernibly. The predictions are respectively compared to the observed temperature illustrated in Figure 2.2. The comparison demonstrates that the validation is notably improved or worsened when different slab's diffusivities are used (Figure 2.3). This consistence is further confirmed in the statistical comparisons, which yield standard deviation less than 0.0043^{o}C. Therefore, selection of the mean value of the thermal parameter tabulated in Table 2.1 is suitable to predict the temperature distribution of a slab; also, the slab temperatures possibly are more sensitive to the weather conditions such as wind speed, air temperature, solar radiation, etc.

Table 2.2 Variation range of the thermal diffusivity of the slabs

Thermal diffusivity	maximum	mean	minimum
$\alpha(10^{-6}m^2/s)$	1.89	1.06	0.53

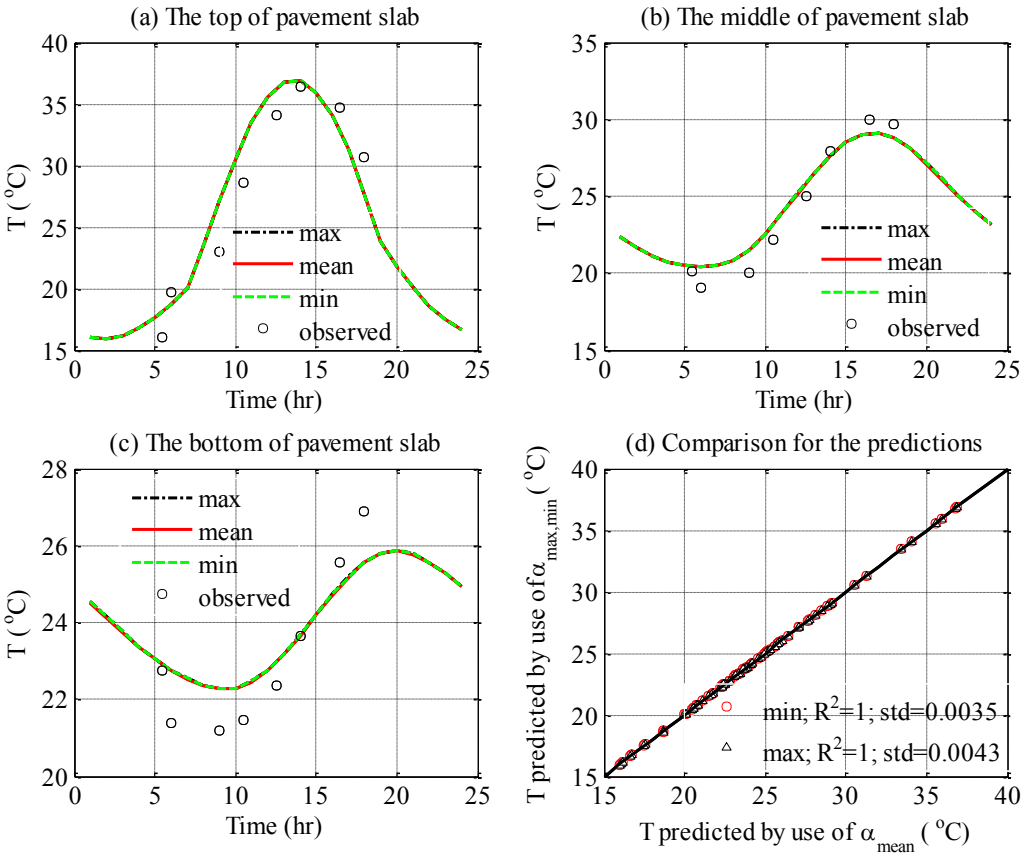

Figure 2.3 Validation of observed temperature by use of maximum, mean, minimum slab's diffusivity.

Considering that a-day temperature prediction is a short-term temperature observation, this study verifies the model using a 12-day field observed temperature with a slab. The monitored temperature was recorded at a slab in Rantoul IL (Kohler 2005). The inputted weather conditions to the model, according to the weather station at Rantoul, are plotted in Figure 2.4. Some days are rainy day such that the solar radiation is less than 200W/m. Other information needed to simulate the slab's temperature is relative humidity and wind speed, which are takes as 0.68 and 3m/s, respectively. The albedo of the slab is 0.5 because the slab was not open to the traffic (Kohler 2005).

The predicted temperatures statistically and visually coincide with the observed temperature (Figure 2.5). A relatively lower of the regression coefficient is possibly due to that the temperature variations were relatively smaller so that the predicted error was

magnified. Also, a relatively higher of the standard deviation comes from the predicted temperature at depth of 1.27cm because of the uncertainties of the inputted weather conditions at the pavement surface. For instance, the wind speed during a specific may vary irregularly.

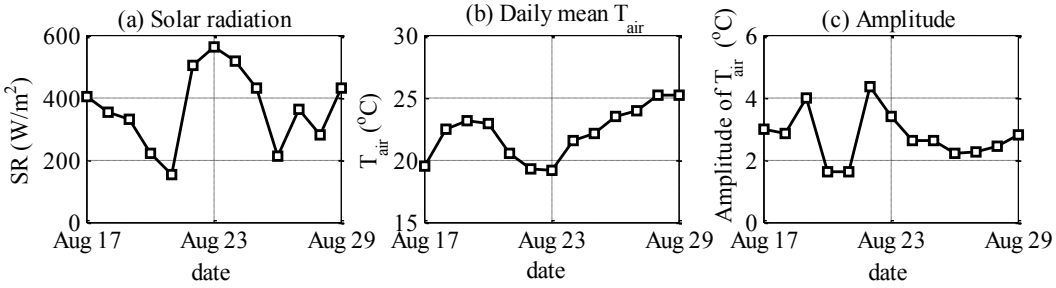

Figure 2.4 The inputted weather conditions at Rantoul, Illinois from Aug 17 to Aug 29, 2003. Note: some days are rainy data such that the solar radiation is less than 200W/m.

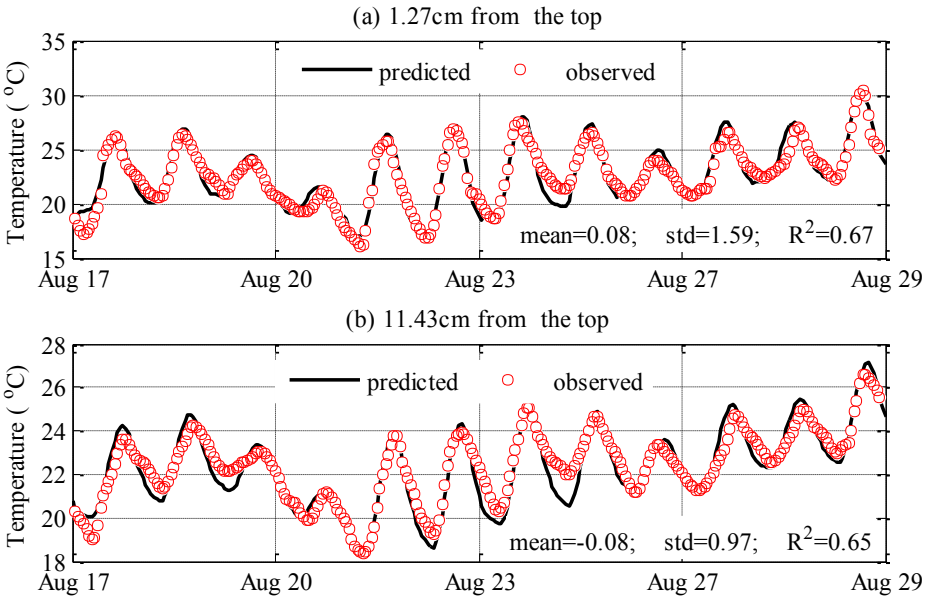

Figure 2.5 Verification of the temperatures observed from a slab in Rantoul, IL.

2.3.2 Verification of the deep ground temperature

Temperature at the bottom of a slab varies not only during a day period but also a seasonal cycle. It exhibits a seasonal cycle. Therefore the agreement of the short term temperature prediction does not necessarily mean that the long-term temperature prediction is reliable. This study also provides a long-term temperature verification of the model by use of the long-term ground temperature observation. Normally, such long-term data is unavailable because the field observation of a slab temperature is easily broken by

the overlain traffic. In this study, the temperature monitoring under the nature ground in a test section on the Qinghai-Tibet plateau, China is use to verified the long-term prediction of the model. The ground surface's albedo is assumed 0.22 ($\gamma_{abs} = 1 - 0.22$); the relative humidity is 0.6 during the whole year. It merits noting that modeling the ground temperature in the cold region like the Qinghai-Tibet plateau needs a formulation of the phase change issue of the ground soil. Details in this issue can be found at (Qin and Hiller 2011a). This inputted weather conditions are plotted in Figure 2.6.

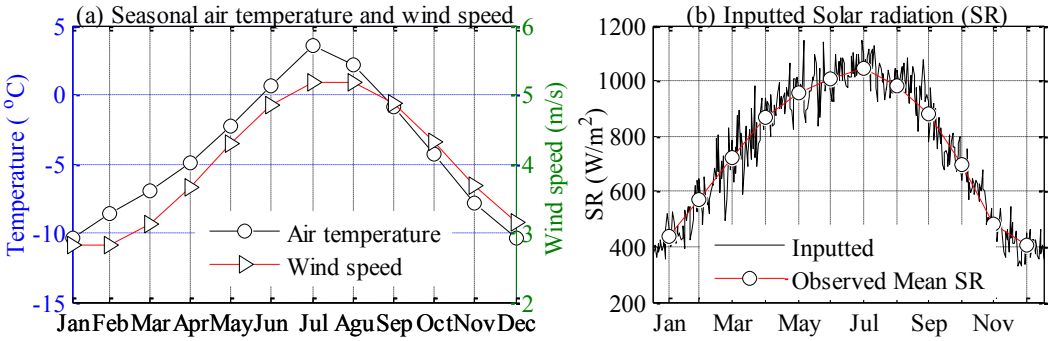

Figure 2.6 The seasonal weather condition at the Qinghai-Tibet plateau.

The predicted temperature statically and visually coincides with and observed data. The predicted temperature series at depth of the 0.5m show excellent agreement with the observed data, with a standard derivation of 0.76°C and an R-squared of 0.97. The proposed model can well predict the zero-curtain of the near ground temperature, as shown in the magnified plot in Figure 2.7b. Considering the temperature at depth may be deviated from the prediction, the temperature profiles on the February 10, 2002 (the coldest day at depth of 0.5m) and August 19, 2009 (the warmest day at depth of 0.5m) are also compared with the predicted profiles. Almost overlaps between the profiles (R^2>0.96) signify that the proposed model is capable of credibly predicting the shallow ground temperature.

2.4 Summary

This chapter develops a heat transfer model to simulate the pavement slab temperature distribution. It verifies the reliability of the model by using the field observation. The model distinguishes itself from the documented model in the following aspects:

- The model adopts a geothermal gradient to the deeper soil of the subgrade. The adoption makes the predicted results contained the information of the thermal history. It also makes the predicted results unaffected by specification of the lower boundary condition.

- The model computes the heat convection coefficient at the pavement by using of the accepted heat transfer theory. The estimated coefficient is impacted by the air thermal conductivity, air Prandtl number, and the characteristic length airflow, etc.
- The model considers both the probabilistic and deterministic portions of the local solar radiation at the pavement surface. It is capable of characterizing the impact of heat history (solar radiation at the previous day or days) on the pavement temperature distribution.

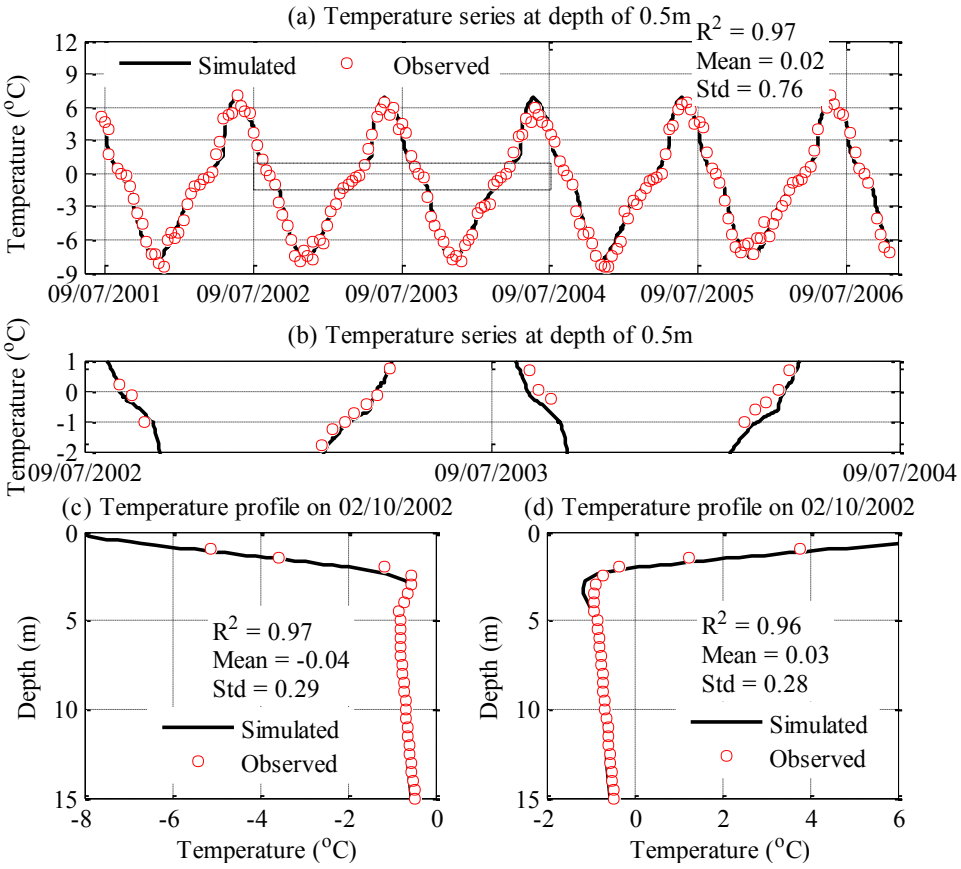

Figure 2.7 The verification of the predicted model by the use of 5-year observed ground temperature in the Qinghai-Tibet Plateau.

Chapter 3 Impact of air temperature[1]

Concrete pavements in the field are subject to temperature gradients and subsequently thermal stresses (Dempsey et al. 1985; Jensen and Hansen 1999). The surrounding air temperature controls the heat convection at the ground surface and plays a crucial role on slab temperature distributions. This role is hardly recognized from field investigations because slab temperature is concomitantly affected by other weather conditions like wind speed, solar radiation, etc. A numerical model capable of reasonably characterizing this role is thus necessary.

Temperature distribution within a slab has been widely modeled (Solaimanian and Kennedy 1993; Ramadhan and Al-Abdul Wahhab 1997). However, the documented models still need improvement, especially in the way to characterizing the impact of ambient air temperature on the heat convection and thermal irradiation at the pavement surface. For example, in the Enhanced Integrated Climatic Model (EICM), the free heat convection coefficient used in this model is minimal (MEPDG 2004). This negligible coefficient goes against the accepted heat transfer theory, in which a coefficient ranging from 5-7 W/m^2 is adopted depending on the ground's surface condition. In the EICM model, the thermal irradiation is evaluated by a series of complex formulas containing several uncertain, empirical parameters (MEPDG 2004). Other models are relatively simpler and consist of less uncertain coefficients (Bentz 2000; Yavuzturk et al. 2005; Gui et al. 2007). However, these models usually adopt a Dirichlet lower boundary, potentially leading to delusive predicted results. These brief reviews necessitate a new model to properly characterizing the role of air temperature on temperature development within a slab.

This study investigates the impact of air temperature on the temperature distribution in concrete pavement slabs. It uses the proposed model in Chapter 2 to simulate the temperature of the pavement slab servicing in different regions. The predicted results center on the impact of the daily air temperature swing on the slab temperature distribution, on the feasibility of using the sinusoidal-approximated air temperature, and on impact of air temperature on pavement-surface thermal irradiation. The associated discussion highlights the difference between the proposed model and documented models, especially the EICM model.

3.1 Study area

This study evaluates thermal regimes of rigid pavements in Los Angeles, California (coastal region) and Reno, Nevada, USA (mountainous desert region), respectively. To assess the extreme case, the pavement's temperature regime on July 22, 2010 is simulated. The thermal parameters of the pavements in these two regions are assumed with the same values to eliminate the effect of the controllable factors (e.g., media thermal conductivities, slab thickness, etc.) on the predicted temperature distributions and to find

[1] The material contained in this chapter was previously published in the journal of Construction Building Material. The copyright permission is attached in the Appendix A.

the differences due to the regions alone. The thermal parameters of the media are tabulated in Table 2.1 (outside the bracket). The slab thickness is 25cm. The uncontrollable environmental factors such as wind velocity and dew point are set to the same values as well. These assumptions are practical because (1) on this date, the mean wind velocity in Reno is about 3m/s and that in Los Angeles is 2.8m/s, and (2) the variation of dew point only slightly affects the irradiation at the slab's surface as its effect on the sky emissivity of Eq.(2.4) is minimal.

The ambient daily air temperatures (DAT) of these two regions are considerably different, as shown in Figure 3.1. The DTA (obtained by using least square fitting) in Los Angeles and Reno are 4.8 and 17.2°C, and the mean air temperatures are 21.2°C and 26.4°C, respectively. This difference in temperature wiggle may result in appreciably different temperature profiles across the slabs.

3.2 Simulation results

3.2.1 Temperature distribution through slabs

3.2.1.1 Slab-surface Temperatures and air temperature

Slab surface temperatures (T_s) are always higher than the ambient air temperatures (T_a), but the magnitude of $T_s - T_a$ varies with time. During the daytime, the pavement slab in Los Angeles experiences higher $T_s - T_a$. This slab is thus able to dissipate more absorbed heat to the air and experiences a lower surface temperature, as shown in Figure 3.2a. Conversely, during the nighttime, the pavement slab in Reno undergoes higher $T_s - T_a$ (Figure 3.2b). In Reno, a hotter slab during the daytime is partially heat-stored and thus keeps the slab warmer during the nighttime. This heat storage makes the slab in Reno hotter than that in Los Angeles. This different pavement surface temperature necessitates an understanding of through-depth temperature profiles, because these profiles determine the thermal stress development within a slab.

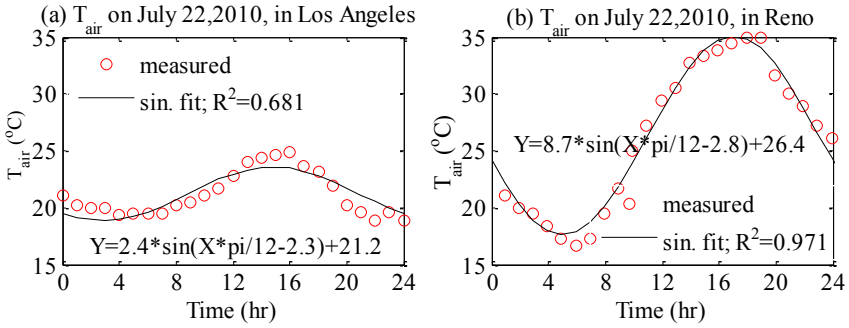

Figure 3.1 Air temperatures on July 22, 2010 in Los Angeles and Reno.

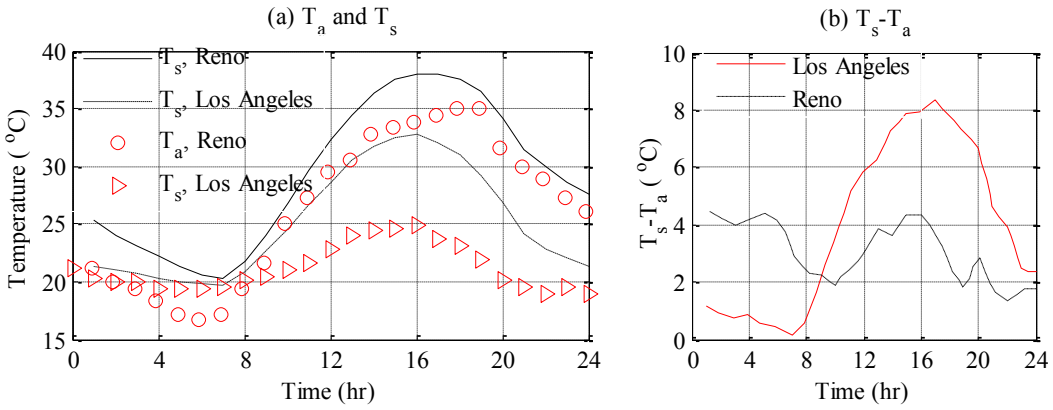

Figure 3.2 Air temperature and slab-surface temperature.

3.2.1.2 Temperature across the slab

Pavements in Reno experiences greater nonlinear temperature gradients, especially during the nighttime. During the daytime, the temperature contours of pavement in Los Angeles are spaced further apart than in Reno, indicating a higher temperature changes through the depth of the slab (Figure 3.3). The maximum temperature differences between the top and bottom are approximately +9°C for the pavement slab in Reno and +7°C for the slab in Los Angeles. This difference occurs owning to that in Reno, the relatively greater air temperature at daytime declines the heat loss from the pavement slab (Figure 3.2 a).

Also, during the nighttime, higher negative temperature gradients develop at the pavement in Reno. As shown in Figure 3.3, the temperature differences between the top and bottom during night hours are approximately -8°C for the pavement slab in Reno and -4°C for the slab in Los Angeles. This difference happens due to that heat convections cools the slab surface rapidly but the remaining parts of the slab remain hotter (the bottom of the slab in Reno is about 5°C higher than that in Los Angeles).

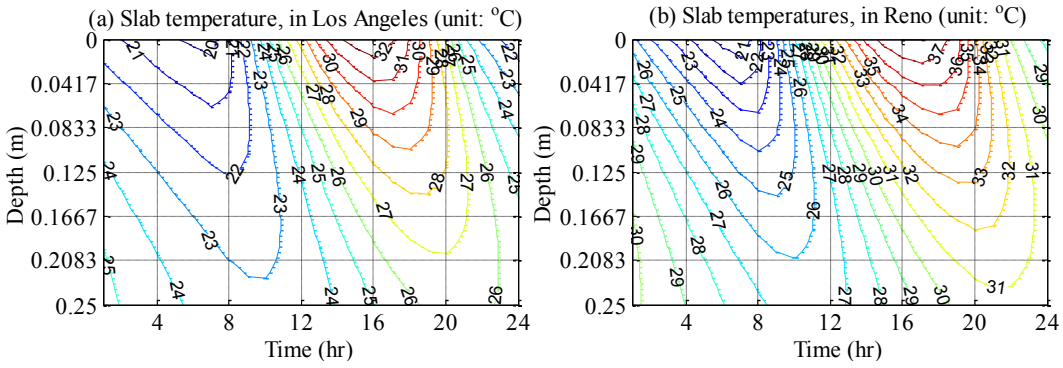

Figure 3.3 Temperature contours of JPCP slabs in Reno and Los Angeles (contours at 1oC spacing).

3.2.1.3 Heat flow at the pavement surface

The pavement surface in Reno experiences higher heat-loss and -gain cycles compared with that in Los Angeles. During the daytime, the total heat flux into the pavement in Reno is higher than that in Los Angeles (Figure 3.4a). During the nighttime, the pavement in Reno also experiences higher heat loss. Total heat flux was declined after 13:00, the peak-value appeared time of the solar radition. But the peak value of the pavement surface temperature appeared around 16:00. This difference occurs because after the midday, the total heat flux at the ground surface still is positive (Figure 3.2) and this positive budget may be higher than the downward-propagated heat budget. This positive daily thermal budget results in that surface temperature still increases after the midday. The budget suggests that whether the peak surface temperature occurs after or before the peak air temperature depends on the solar radiation, heat convection, and thermal irradiation.

Different total heat fluxes of these two slabs are due primarily to the different heat convection and thermal irradiation at the slab surfaces. For heat convection, the pavement in Reno undergoes less convection during the daytime (Figure 3.4b) because the high surrounding air temperature hinders the heat dissipation from the surface. Conversely, during the nighttime, the pavement in Reno experiences more heat convection as the higher $T_s - T_a$ in Reno (Figure 3.2b) facilitates heat outflow from the slab surface.

Thermal irradiation primarily depends primarily on the slab surface temperature (Eq. (2.2)). Because the slab surface temperature in Reno is always higher than that in Los Angeles, the thermal irradiation of the pavement in the former region is always higher than that in latter (Figure 3.4c). During the nighttime, the pavement in Los Angeles experiences approximately 30 W/m^2 heat loss than that in Reno because the $T_s - T_a$ of the slab in Los Angeles is close to zero at this time (Figure 3.2b).

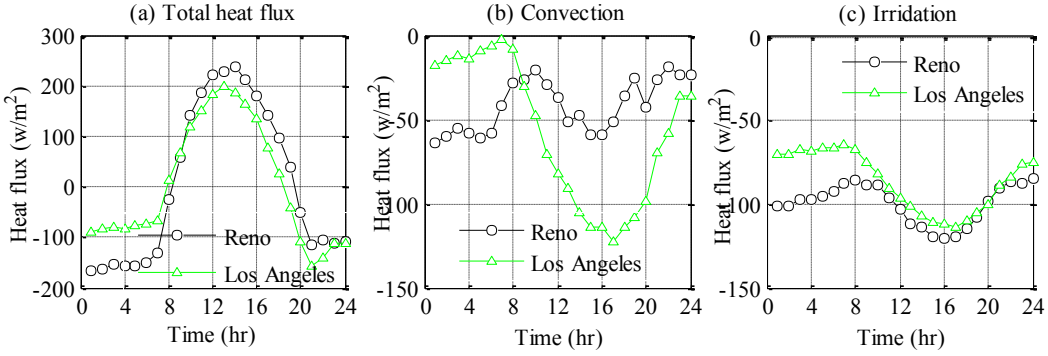

Figure 3.4 Heat flux at the top of the slabs.

3.2.2 Use of sinusoidal-approximated air temperature (SAAT)

3.2.2.1 The significance of using SAAT

The impacts of the local air temperature on the slab's temperature distribution demonstrate at the numerical results shown in the above sections. However, a detailed air-temperature series of a given day may be missing from a database, especially when the long-term temperatures through a slab are estimated. Even though such series are available in NOAA database in one hour intervals, the temperatures between intervals have to be interpolated since the step time of the numerical model is far less than 1 hour to achieve convergence. According to a formula presented by (Gui et al. 2007), the minimum time step would be approximately 6 minutes if quadratic elements are used and the element length is 1cm, in order to make the simulation reasonably converged.

Therefore, a question may arise. Can the daily air temperature input to our models be approximated as a sinusoidal function? If the error resulting from this approximation is minimal, the inputted DTA into a computational model can be parameterized by the mean daily air temperature and its amplitude.

3.2.2.2 The feasibility of using SAAT

Replacing the field air temperature (FAT) with the SAAT does not affect the numerical results significantly. Figure 3.5 shows the heat fluxes at the surface and plots the temperatures of the slab when the model replaces the FAT with the SAAT. Regression coefficients for this replacement are consistently higher than 0.98. The errors resulting from this replacement are tabulated in Table 3.1. Errors of the simulation for the slab in Los Angeles are almost the same magnitude as those in Reno, although the regression coefficient for the air temperature in Los Angeles is significantly lower (Figure 3.1). Therefore, replacing FAT with SAAT is feasible when predicting temperature distribution through a slab, even if the air temperature does not necessarily follow a sinusoidal pattern rigorously.

This approximation is feasible because the net thermal budgets resulting from this replacement are minimal. As shown in Figure 3.5a, this replacement influences the heat flux at the pavement surface more than it does temperatures distribution (Figure 3.5b and c). Using the SAAT as a substitute of the FAT makes the input air temperature different from the field air temperature. It thus results in the heat convection and thermal irradiation deviating from the field conditions. However, the deviation is compensated during a day period, and therefore the average of these deviations is close to zero (-1.1 W/m and 0.43 W/m, for Reno and Los Angeles, respectively).

3.2.3 Impact of air temperature on the thermal irradiation

Air temperature influences the heat convection explicitly (Eq. (2.6)) and also affects the thermal irradiation implicitly. The implicitness presents in Eq. (2.3), in which the air temperature directly correlates with sky temperature. In the Stefan-Boltzmann law, the

thermal irradiation linearly decreases with $T_{\square ky}^4$. This quadruple power-law linking T_a to T_s merits a thorough examination and review.

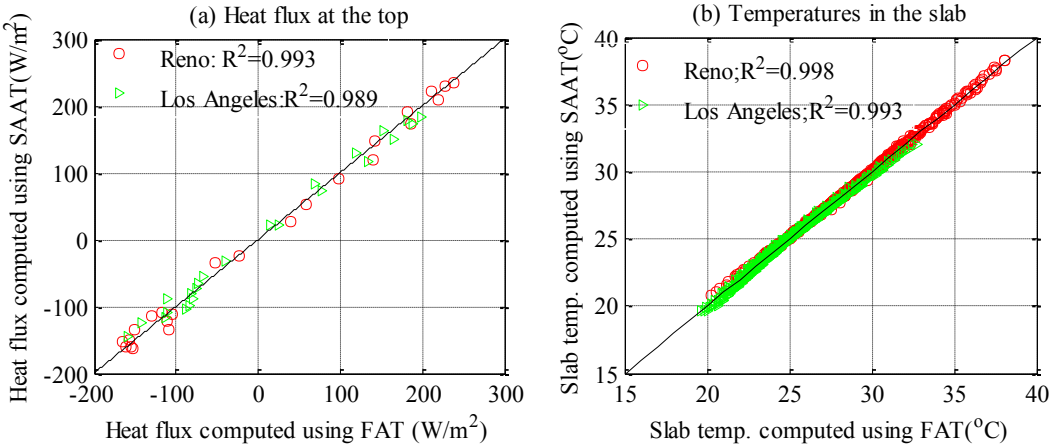

Figure 3.5 The feasibility of using sinusoidal approximated air temperature input (SAAT).

Table 3.1 The errors of using SAAT in the numerical model

Error	Heat flux(W/m^2)		Temperature(^{o}C)	
	Los Angeles	Reno	Los Angeles	Reno
Standard error	12.07	11.72	0.12	0.17
Maximum error	27.02	20.52	0.58	0.67
Mean error	-1.10	0.43	0.10	-0.12

3.2.3.1 The correlation between air and sky temperature in the literature

The sky temperature is determined primarily by the surrounding air temperature and also to a certain extent, by other factors including the dew point, water vapor pressure, sky cloud cover, etc. The simplest formulations to evaluating the sky temperature are Eq. (3.1) (Dreyfus and Hilleary 1962) and Eq.(3.2) (Swinbank 1963):

$$T_{sky} = T_a \tag{3.1}$$

$$T_{sky} = 0.0552T_a^{1.5} \tag{3.2}$$

These straightforward, easily-obtained formulas fail to consider the impacts of the factors like dew point. One model that considers the impact of the water vapor tension P_v (mmHg) is Eq. (3.3) (Centeno V 1982):

$$T_{sky} = T_a(0.056 + 0.08P_v^{0.5})^{0.25} \tag{3.3}$$

Because P_v is a function of air temperature (Ahren 2007), Eq. (3.3) does not count the effect of the dew point on the sky temperature. Another model that considers this effect is Eq. (3.4) (Berdahl and Fromberg 1982)

$$\varepsilon_{sky} = 0.741 + 0.0062T_{dp} \tag{3.4}$$

The sky emissivity can be also a function of the combined effect of cloud cover, water vapor pressure, and dew point. Formulations for this function are overly complicated. One of these formulations, proposed by Walton (Walton 1985), uses the combination of Eq.(3.5) and (3.6).

$$\varepsilon_{sky} = 0.787 + 0.764 \times ln\left(\frac{273+T_{dp}}{273}\right) \times F_{cloud} \tag{3.5}$$

where F_{cloud} is a cloud cover factor calculated as follows:

$$F_{cloud} = 1.0 + 0.024N - 0.0035N^2 + 0.00028 * N^3 \tag{3.6}$$

where N is cloud cover, taking value between 0 to 1.0.

3.2.3.2 Impact of air- and sky-temperature correlation on numerical results

The predicted slab temperature depends, to a certain extent, on the correlation utilized between the sky and air temperatures. Numerical results from the different models presented in Eqs.(3.1) to (3.6) are compared to the temperatures recorded by Yu et al (1998), which has been verified in Figure 2.2. Comparisons between the predictions from different model are demonstrated in Figure 3.6. The models (Dreyfus et al., and Swinbank) that directly link the sky temperature to air temperature tend to overestimate the temperature of a slab, whereas the Swinbank's formula appears to better predict the pavement slab's temperature (Figure 3.6a). The models that consider the dew point and/or the cloud cover show a higher level of reliability to predict the slab surface temperature (Figure 3.6b). These models predict temperatures results in a regression coefficient greater than 0.91.

However, this does not necessarily indicate that some models are capable to correctly predict the pavement temperature whereas others are not (Qin and Hiller 2011b). As shown in Figure 3.6a, the temperatures predicted using the formulas of Dreyfus et al., and Swinbank shows approximately 3-4^{o}C higher than the measured temperatures. An adjustment of the input parameters, e.g., wind velocity and/or daily solar-radiation peak value, can generate predicted temperatures from this model to better match the observed temperature. In this regard, better predictions of the temperature distribution in a pavement slab require proper characterization of the correlation between sky and air temperatures. Further investigation is expected to refine this determination between sky temperature and air temperatures.

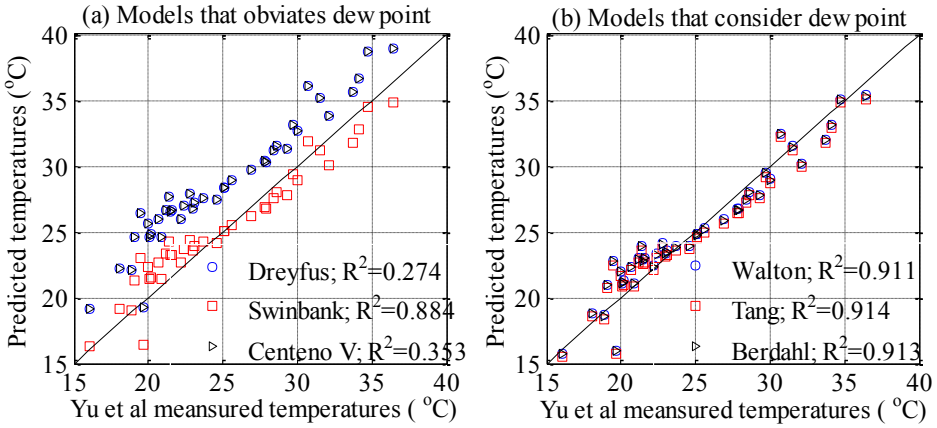

Figure 3.6 Predicted slab temperatures computed from different sky-temperature formulas; Note: In Walton model, *N=0.1* is used as the sky condition is unusually clear during the summer near the Kansas-Colorado border.

3.3 Discussion

3.3.1 Applications to other regions

All the presented data and associated analysis are based on an extreme summer weather condition in either Reno or Los Angeles. Extents of them to other regions or to other seasons provoke, at least, four questions.

3.3.1.1 Does the augment that $T_a < T_s$ still hold true?

The inequality of $T_a < T_s$ fails to hold true in other seasons, especially in the high altitude regions. To illustrate this issue, we consider the weather conditions in the polar region during the winter time. In this case, the solar radiation is negligible. The thermal irradiation and the heat convection dominate the heat convection at the pavement surface. The pavement (ground) surface temperatures should satisfy the following inequality:

$$T_{sky} < T_s < T_a \tag{3.7}$$

This inequality holds because:

1) If $T_a < T_s$, both the thermal irradiation in Eq.(2.6) and heat convection in Eq. (2.2) consists of the heat loss from the surface. T_s thus must rapidly decline until $T_s = T_a$.
2) If $T_s = T_a$, then $q_{conv} = 0$ and $q_{irr} < 0$ because $T_{sky} < T_a$ ($\varepsilon_{\text{sky}} < 1$). Therefore, T_s still has to decrease and thus $T_s < T_a$.
3) If T_s decrease to a degree such that $T_s = T_{sky}$, then $q_{conv} > 0$ and $q_{irr} = 0$. Therefore, T_s increases and thus $T_s > T_{sky}$.

These three reasons indicate that the inequality of Eq. (3.7) must hold in polar regions during the wintertime. In other regions, this inequality may hold depending on the altitude of the location. In seasons other than winter time, the inequality may also hold depending on the available solar radiation. Therefore, one cannot conclude that $T_a < T_s$ consistently or vice versa.

3.3.1.2 Does the daily air temperature still appreciably influence the thermal gradient across a slab?

The influence of the daily air temperature on the temperature gradient of a slab is still notable in other regions or seasons. In other regions during the summertime, the incoming solar radiation heats up the pavement surface temperature rapidly during the daily time. A higher swing of the surrounding air temperature thus decreases the heat convection, resulting in a greater temperature positive temperature profile developing within a slab.

During other seasons such as winter time, the incoming solar radiation becomes less dominant on the heat exchange at the ground surface. The air temperature still controls the heat convection at the top. A greater daily air temperature variation leads to a greater temperature variation at the pavement surface. In this regard, a greater daily air temperature variation still results in a steeper gradient of the temperature profile within a pavement slab.

3.3.1.3 *Is replacing field air temperatures with SAAT still feasible?*

Replacing the field air temperatures within SAAT does not compromise accuracy of the predicted temperature, regardless of the regions or season. In this study, the simulation uses the weather conditions in extreme cases. Such cases make the predicted results being magnified. This means that the replacement will be certainly feasible in other regions and in other common daily air-temperature swing cases.

Here now considers uncommon cases that the air temperature either increases or drops suddenly. Supposed that a sudden drop of the air temperature of 10^oC occurs in a summer day, the ground surface temperature has to decline. However, this decline is greatly less than the 10^oC owning to three reasons.

(1) In this case, the regression air temperature yields lower daily temperature amplitude than the difference between maximum and minimum air temperatures, as shown in Figure 3.1b.
(2) The existence of both the temperature boundary layer and speed boundary layer (wind effect) make the surface temperature dampened to the sudden variation of the ambient air temperature.
(3) The heat development within the slab is inherited (Figure 3.3). The heat inheritance from the previous time frame supplies heat to the pavement surface, preventing an extreme sudden temperature drop at the top.

These three arguments strengthen the feasibility of the replacement of field air temperatures with SAAT, even as a sudden air temperature drop occurs. An example of

this feasibility is shown in Figure 3.1b. A sudden air temperature variation about 4°C occurred from 09:00 to 10:00 and from 16:00 to 18:00. However, the prediction using the SAAT agrees well with the prediction using the field air temperatures, with little notable deviation (Figure 3.5a). These same arguments can be made in terms of an abrupt air temperature increase as well.

3.3.1.4 Do the methods of estimating the sky temperature still notably influence the predicted temperature?

The methods to computing the sky temperature still appreciably affect the pavement temperature regardless of the regions and the seasons. Normally, the dew point can be 5-10°C lower than the air temperature, depending on the local air relative humidity (Centeno V 1982). The hold of the inequality of Eq.(3.7) thus proves this impact during the winter seasons. During the summer time, the surface temperature is heated up by the solar radiation, magnifying the role of the sky temperature on the thermal irradiation according to Eq. (2.2).

3.3.2 Difference between the proposed model and EICM model

One distinguishable feature of the proposed model from the documented models, particularly the EICM model, relates to the specification of the lower boundary condition. The EICM model, as well as other models like Bentz model (Bentz 2000), adopts a constant temperature at a certain depth below the pavement surface, assuming that the soil at this depth is capable of supplying infinite heat to keep temperatures therein constant.

When considering the role of the air temperature, the difference between the various models' methods of estimating the heat convection and thermal irradiation is distinct. This is due to the air temperature appearing explicitly in Eq. (2.6) and implicitly in Eq. (2.2).

3.3.2.1 Heat convection in different models

The method for computation of the heat convection coefficient h_{conv} in the EICM model is somewhat unreliable. This model evaluates h_{conv} use Eq. (3.8)

$$\mathrm{h_{conv}} = \beta * [0.00144\mathrm{T_m^{0.3}w^{0.7}} + 0.00097(\mathrm{T_s} - \mathrm{T_a})^{0.3}] \tag{3.8}$$

where T_m (°K) is the average of the surface and air temperatures (Dempsey et al. 1985); β is constant, $\beta = 122.3$. Setting wind velocity to $w = 0$, the h_{conv} is close to zero because $0.00097(\mathrm{T_s} - \mathrm{T_{air}})^{0.3}$ is minimal. This indicates that the EICM model adopts zero convection in the case of free convection (no wind velocity). This zero free convection goes against the accepted heat transfer theory (Jiji 2009). Another unreliable factor of Eq. (3.8) is that the pavement surface temperature must always be higher than the air temperature, otherwise h_{conv} would be a complex number. This is not always the case as demonstrated in Eq. (3.7).

To further show the impact of the EICM method to compute h_{conv},, Figure 3.7 plots the h_{conv} calculated from the proposed model, EICM model, and Bentz's model, the last of which uses Eq. (3.9).

$$h_{conv} = \begin{cases} 5.6 + 4.0 \times w, & w \leq 5 m/s \\ 7.2 \times w^{0.78}, & w > 5 m/s \end{cases} \quad (3.9)$$

Details pertaining to the difference between Bentz's model and the proposed model involve analysis on the heat transfer theory relevant to the topic of heat convection and thus are out of the scope of this dissertation. However, Figure 3.7 clearly illustrates the difference between the models. Use of the h_{conv} computed from EICM model significantly underpredicts the heat convection occurring at the pavement in comparison with the Bentz and proposed models. Since this convection normally accounts for the heat loss from the ground, adoption of EICM model would overpredict the pavement temperature. In addition, this predicted temperature from the EICM is insensitive to variations of wind speed, as illustrated through the calculated h_{conv} (Figure 3.7).

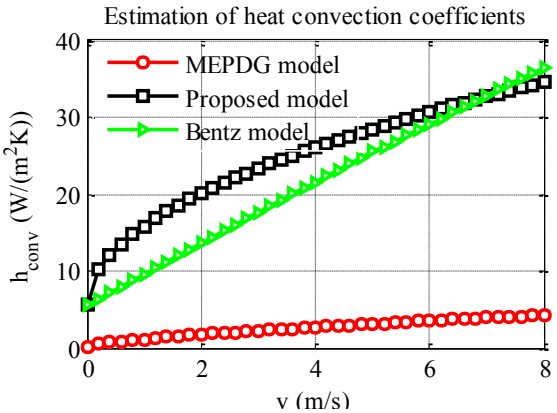

Figure 3.7 Comparison between inputted heat convection coefficients for different models. Note: when the h_{conv} in the EICM model computed, $T_s - T_a = 30^{o}$C is used in order to magnify the computed h_{conv} of the model. $T_s - T_a$<0 ^{o}C results in a complex number using Eq. (3.8).

3.3.2.2 Thermal irradiation in different models

It is necessary to compare the thermal irradiation in the proposed model with the EICM model because the EICM is the most widely-used tool to predict the temperature distribution in PCC pavements. Unfortunately, the EICM does not use the sky temperature to formulate the thermal irradiation at the slab surface. The impact of sky temperature on the pavement temperature distribution thus cannot be directly estimated. However, the formulation of thermal irradiation in both the proposed model and Bentz model are simpler and rely on less uncertain parameters (MEPDG 2004). In EICM model, the parameters to compute the thermal irradiation from the sky emissivity

includes cloud base factor, average cloud cover during day and night, air vapor pressure, and several empirical coefficients (G, ρ, and J) , etc.

For the sake of the simplicity and clearance, use of the formula in the EICM model to compute the thermal irradiation at the ground surface is not recommended. According to heat transfer theory (Jiji 2009), the irradiation should be evaluated using the sky emissivity. Methods to this account for sky emissivity are highlighted in the Eq. (3.1) to Eq.(3.5), depending on the available local weather data. Tang's formula (Eq.(3.4)) is recommended and utilized in the proposed model. It links the sky temperature to dew point for the best accuracy of temperature prediction in concrete slabs whereas not requiring the cloud factor, which can be a highly uncertain parameter.

3.4 Conclusions

The impact of air temperature on the temperature distribution through pavement slabs has been presented from three aspects: (1) the impact of DTA on pavement temperature distribution through the slabs, (2) the feasibility of using the sinusoidal-approximated air temperature, and (3) the predicted thermal profile results dependence on the correlation between the air and sky temperatures. Also, the difference between the proposed model and documented models, especially the EICM model, is highlighted in terms of how these models characterize the impact of air temperature on the heat convection and thermal irradiation. From this study, the following points can be drawn:

- The daily temperature amplitude affects the temperature distributions across a pavement slab during the daytime more than during nighttime. Pavements in regions with higher daily air temperature amplitude experience greater negative temperature gradients during the nighttime hours.
- Replacing the field air temperature with the sinusoidal-approximated air temperatures does not affect the predicted slab temperature. The occurrence of a sudden air temperature drop or increase does not compromise this agreement significantly.
- Uses of the correlations between air and sky temperatures in a slab-temperature predicted model notably influences the predicted results. Methods that estimate the thermal irradiation by link the sky emissivity to dew point should be included in a slab-temperature predicted model.
- The EICM model tends to significantly underestimate the heat convection coefficient and thus overpredict the pavement temperature, compared with the proposed and other published models. The use of the EICM model potentially results in the predicted temperatures highly insensitive to wind speed variations.

Chapter 4 Impact of wind speed[2]

In-service jointed plain concrete pavements (JPCPs) suffer from diurnal temperature variations and lead to thermal deformations across the pavement slab. Stresses caused by these deformation depend, to a certain extent, on the pavement geometry and the underlying layer support but primarily on the temperature distribution within a slab. They thus mainly rely on the in-situ weather conditions, e.g., solar radiation, air temperature, wind velocity, and the combination of these factors. Among these conditions, the role of wind speed on the pavement temperature distribution merits a thorough study because wind velocity greatly determines the amount of heat convection occurring at the pavement surface.

The impact of wind conditions on the temperature profile of a pavement structure has been well documented (Kapila et al. 1997; Bentz 2000; Burkan Isgor and Razaqpur 2004; Yavuzturk et al. 2005); but formulation of the wind speed on the heat convection coefficient remains contentious. Such a coefficient at pavement surface nonlinearly increased with wind speed (MEPDG 2004). Currently use of the nonlinearity is based on the empirical regression of laboratory experiments. It overlooks the impact of the air thermal properties like thermal conductivity, air-flow Reynolds number, etc. on heat convection. This impact had been considered by Kapila *et al*. (1997), which connected the heat coefficients to the Reynolds and Prandtl numbers of the air. However, Kapila *et al*. assumed that the characteristic length used to compute the Reynolds number is the width of the pavement. This characteristic length used is significantly larger than that computed from traditional heat transfer theory (Jiji 2009). Although the heat convection coefficients calculated from the aforementioned models deviate from each other, it is clear that wind velocity directly influences the heat convection at ground surface. If this influence is of considerable magnitude, a proper estimate of the heat convection will be critical in predicting this influence on both temperature profiles and thermal stresses in JPCPs.

This chapter investigates the impact of wind velocity on the temperature distribution in JPCPs and evaluates the role that the heat convection coefficient plays with respect to stress profiles in the slab. It centers on the degree that the variation of wind speed on the temperature distribution and thermal-stress distribution through a pavement slab. It highlights the difference between the methods to computing the heat convection coefficients in different models. The reliability of these models is analyzed on the basis of the accepted heat transfer theory and of the predicted feasibility.

4.1 Simulation results

This chapter estimates the temperature and thermal stresses of a JPCP in Reno, Nevada. To assess the maximum stress effect, the pavement temperature regime for July 12, 2010 is simulated. The thermal parameters regarding the underlying soils under I-80

[2] Part of the material contained in this chapter was submitted to Journal of Transportation Engineering for considering publication.

at Rainbow Ridge Park (in Reno) are obtained from USDA. The slab's thickness is 25.4cm and the local air temperature, dew point temperature, etc., are obtained from NOAA. The air temperature series and wind speeds on July 12, 2010 are demonstrated Figure 4.1a and Figure 4.1b, respectively. The temperature series can be approximated to a sinusoidal period, whereas the wind speed exhibits more randomized deviation with a maximum speed of 9m/s. Because of these varying wind velocities in field, the following simulates both the temperature profiles and developed thermal-stress profiles of a slab under different wind velocities.

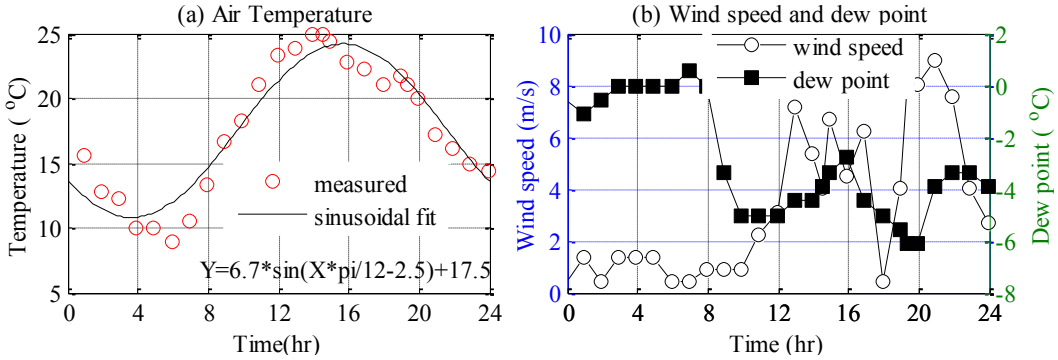

Figure 4.1 Air temperature and wind speed on July 12, 2010, in Reno, Nevada

4.1.1 Effect of different wind velocities on temperature development

An increase of wind speed from 0-6 m/s greatly declines the temperature of a slab. Degree of the decline depends on the time of a day and on the amount the incoming solar radiation (Figure 4.2). During the daytime, the top of the slab declines roughly 2°C if the weather is a cloudy day; whereas the temperature difference at the bottom seems negligible. During a sunny day, the decline at the top would be up to approximately 14°C at the top and about 8°C at the bottom. The reason that wind blow can reduce the temperature more in a sunny day is that wind flow at such a day is capable to dissipate more energy from the pavement surface. At the night, although the solar radiation vanishes, wind still notability affects the pavement temperature, especially during a sunny day. This is because the heat inherited during the daytime makes the thermal state of the slab different from the state of the surrounding air. At the night time of a sunny day, increase of wind speed from 0-6m/s reduces the 4°C at the top and 6°C at the bottom. Therefore, the effect of the wind speed on the pavement slab varies with time and depends on the available solar radiation.

The increase in airflow helps mitigate the nonlinear temperature gradients through the slab, especially during the daytime of a sunny day. This gradient reduction is visualized at the density of the temperature contours shown in Figure 4.2. During the daytime of sunny day, the slab experiencing 6m/s airflow has temperature contours that are spaced further away (Figure 4.2d) than those under no wind (Figure 4.2c), indicating higher temperature gradients in the slab. The gradient reduction can be also estimated from the

temperature cycles that the bottom and top of the slab suffer from. As illustrated in Figure 4.2, during a sunny day, the amplitude of slab-top temperatures is 38°C in the case of 0m/s wind speed and 28°C in the case of 6m/s wind speed.

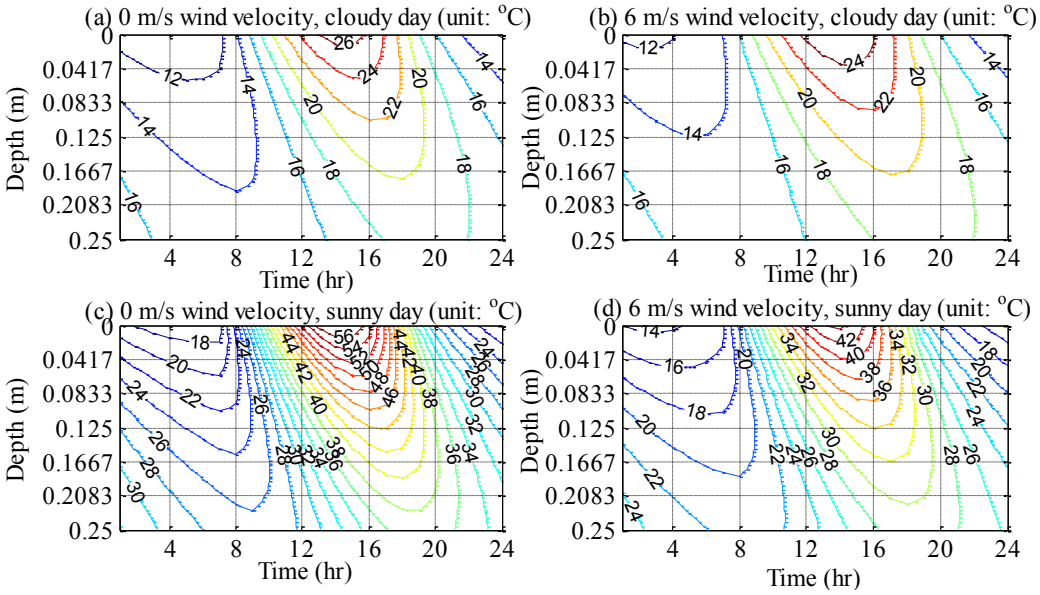

Figure 4.2 Temperature contours of a slab experiencing different wind velocities. Note: coordinate system is considered positive downward and measured from the slab's top.

4.1.2 Computation of the curling-induced stress within a slab

Curling of rigid pavement slabs has captured considerable attention (Ashraf R. Mohamed and Hansen 1996; Ashraf Mohamed and Hansen 1997; Yu et al. 1998; J.E. Hiller and Roesler 2008). Several methods have been proposed to compute the exact amount of curling-induced stress (Hong et al. 1997; Ashraf Mohamed and Hansen 1997; Jacob Eskel Hiller 2007) within JPCP slab. They usually use elastic plane theory to compute the thermal stresses within a pavement slab, assuming negligible uniform temperature effects. Any temperature profile $T(z)$ results in a specific strain profile $\varepsilon_T(z)$:

$$\varepsilon_T(z) = \alpha T(z) \tag{4.1}$$

where α (10^{-6}/°C) stands for the thermal expansion coefficient of the slab. The strain in Eq. (4.1) results in a stress profile proportional to the temperature profile if the stresses within the slab develop freely. This stress profile, called free stress profile, is:

$$\sigma_T = -\frac{E}{1-\mu}\alpha T(z) \tag{4.2}$$

where E is the conventional Young's modulus of concrete (Pa); μ is the Poisson ratio of the slab.

Stresses estimated in Eq. (4.2) are free stresses. They automatically redistribute to minimize the stress energy according to the principle of minimum potential energy. The redistributed stress is the real stress that the slab subjects to. It can be definitely computed by use of 3-D finite element method to evaluate Eq.(4.2) (Pane et al. 1998). However, considering that pavement engineering is more of practical importance than theoretical importance in nature, this dissertation uses the method proposed by Mohamed and Hansen to compute the redistribution of the free stresses (Ashraf R. Mohamed and Hansen 1996). This method, easily followed by engineers, is briefly presented in the following.

The stresses in the Equation (4.2) generate a normal internal N (N) and a bending moment M (Nm^2). These two forces are:

$$N = \int_{-h/2}^{h/2} \sigma_T dz \tag{4.3}$$

And

$$M = \int_{-h/2}^{h/2} \sigma_T z dz \tag{4.4}$$

where h is the thickness of the slab; z is the coordinate that is perpendicular to the slab surface and has an origin at the middle of the slab.

Both the force in Equations (4.3) and the moment in Eq. (4.4) make the slab being in a un-equilibrium state. It is thus necessary to impose an equal, opposite force N and moment M to balance the resulting stress distribution. These forces come from the self-weight of the slab and from the reaction among the slab, base, and roadway shoulder. Therefore, the self-equilibrating stress σ_{res} (MPa) resulting from the constraints of compatibility is:

$$\sigma_{res} = \sigma_T - \frac{12Mz}{h^3} - \frac{N}{h} \tag{4.5}$$

where the second term of the Eq.(4.5) stands for the stress coming from the moment M; the third term, from the force N.

Other than σ_{res}, a temperature profile through the slab results in linear stresses developed in the slab. This development is due to the restraint of the slab's self weight to the bending moments M. This moment results in a bending curvature, κ; their relationship can be estimated by Eq. (4.6):

$$\begin{bmatrix} M_x \\ M_y \end{bmatrix} = \frac{Eh^3}{12(1-\mu^2)} \begin{bmatrix} 1 & \mu \\ \mu & 1 \end{bmatrix} \begin{bmatrix} \kappa_x \\ \kappa_y \end{bmatrix} \tag{4.6}$$

where κ_x and κ_y are the bending curvature induced by the M_x and M_y respectively, as a schematic show in Figure 4.3.

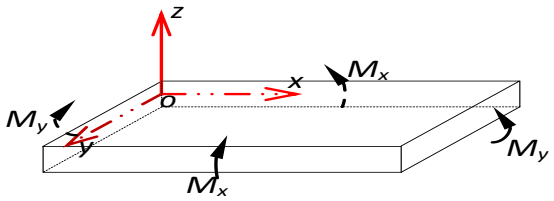

Figure 4.3 Schematic showing the bending moment induced by a temperature profile.

Equation (4.6) indicates that if the slab is weightless, M would make the slab deforme to a curve with curvature of κ. When the temperature variation occurs along z direction only (1-D model), $M_x = M_y = M$ and $\kappa_x = \kappa_y = \kappa$. Therefore, Equation (4.6) can be re-arranged to:

$$\kappa = \frac{12M^*}{h^3} \ . \tag{4.7}$$

where

$$M^* = M(1-\mu)/E \tag{4.8}$$

here M^* (m^2) is constant depending on the free stress profile. The curling induced by the bending moments is equal to a nominal linear temperature gradient ΔT_{eq}:

$$\Delta T_{eq} = -\frac{12M^*}{\alpha h^2} \tag{4.9}$$

Therefore, the linear stress can be computed by (Westergaard 1927; Bradbury 1938):

$$\begin{cases} \sigma_x = \dfrac{E\alpha\Delta T_{eq}}{1-\mu^2}(C_x + \mu C_y) \\ \sigma_y = \dfrac{E\alpha\Delta T_{eq}}{1-\mu^2}(C_y + \mu C_x) \end{cases} \tag{4.10}$$

where σ_x and σ_y are the stresses in the transverse and longitudinal directions, respectively; C_x and C_y are two variables of the stress correction factor (Bradbury 1938). These two variables are determined by the dimension of the slab and by the support of the subgrade. This dissertation uses the following parameters:

- Coefficient of thermal expansion $\alpha = 9\mu\varepsilon / °C$
- Young's modulus $E = 20GPa$
- Poisson ratio $\mu = 0.15$
- Slab dimension: *X*=3.6m (transverse); *Y*=6.0m (longitudinal);
- Modulus of subgrade reaction, *k*=50MPa/m

When these parameters are used, the stress correction factor for the slab's width and slab's length are $C_x = 0.62$ and $C_y = 1.01$, respectively (Westergaard 1927; Bradbury 1938). The stresses plotted and discussed in this dissertation are the longitudinal stresses, which are generally greater than the transverse since $C_y > C_x$ for most instances.

4.1.3 Impact of wind speed on the curling stress

4.1.3.1 Stress profile

The airflow helps mitigate the linear and self-equilibrating stresses (Figure 4.4). The linear stress significantly decreases when the wind blows across the pavement surface. This decrease occurs since the airflow-induced heat dissipation from the slab lessens the temperature difference between the top and the bottom and thus reduces the bending moment in the slab. The self-equilibrating stress also decreases due to an increased airflow. Since wind directly affects the surface only, this influence occurs more at the top than the bottom (compare Figure 4.4a and c).

The total stress is remarkably reduced when wind speed increased from 0 to 6m/s. It decreases more notably at daytime than at nighttime. At daytime, when wind speed is 0m/s, the compressive stress at the top and the tensile stress at the bottom are -3.6MPa and 2.2MPa, respectively; when the wind speed increase to 6m/s, these stresses would be -2.5MPa and 1.6MPa, respectively. At night, such decreases of the maximum tensile stress at the top are less notable (0.2MPa reduction with 6 m/s wind).

4.1.3.2 Stress contours

In less windy conditions, the slab bottom suffers from more tensile stress than the top. The top of the slab suffers from tensile stresses at nighttime while the bottom experiences tensile stresses at daytime. The bottom of the slab, despite experiencing lower absolute temperature variation, suffers from higher tensile stresses than the top (Figure 4.5a and c). This is because during the daytime, the slabs in less windy regions have more bending stress, resulting in the bottom of the slab suffering from a relatively higher tensile stress. An increase of wind speed lessens this bending stress and makes the stress bottom experienced less tensile stress (Figure 4.5b and c).

The effect of wind speed on the slab's stress distribution depends on the available solar radiation. At noon of a cloudy day, the tensile stress at the bottom is not

significantly influenced by the airflow speed (comparing Figure 4.5a and b). But on a sunny day, the impact of wind velocity on the stress distribution through the depth of the slab becomes pronounced in that the stress contours near the top and the bottom are densified. This is because during a sunny day, the wind speed dissipates a relatively more heat energy from the pavement surface. More heat dissipation leads to less temperature gradient near the surface and thus mitigates the stress gradient near the top.

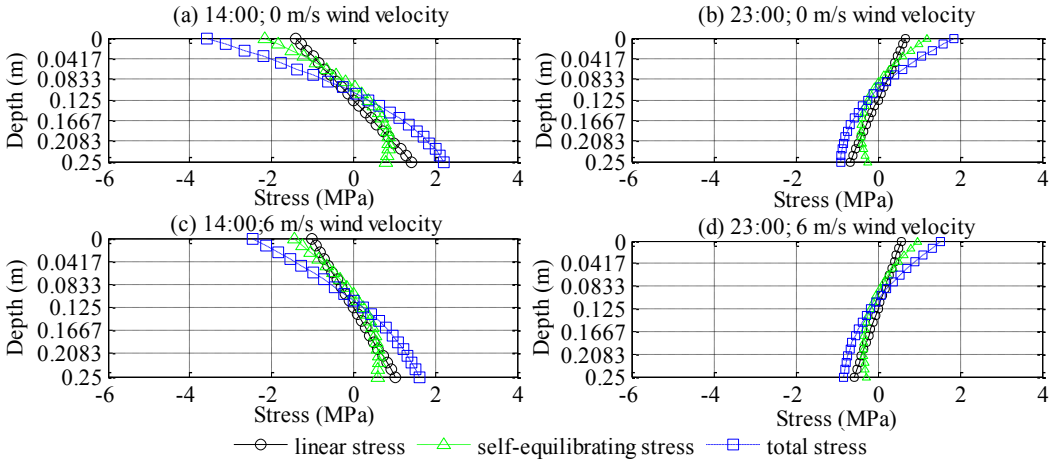

Figure 4.4 The predicted thermal stress profile through a slab on a sunny day. Note: negative—compressive; positive—tensile.

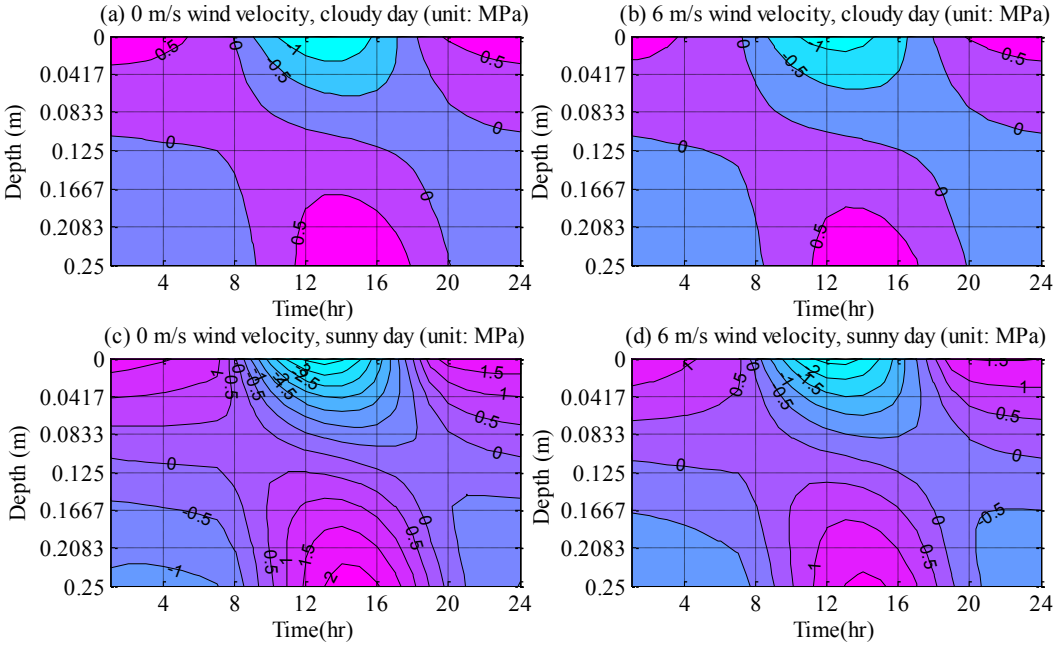

Figure 4.5 Predicted stress distribution in the slab for different wind velocities and weather conditions (contours at 0.5 MPa spacing).

4.1.4 Thermal stresses and wind velocity

Magnitude of maximum tensile stress to which the slab is subjected linearly decreases with an increase in the wind speed, as illustrated in Figure 4.6. The decreasing rates of these stresses on a sunny day are significantly higher than that for a cloudy day (Figure 4.6a and b). This rate at the slab's bottom is approximately one-and-half times that at the top, regardless of whether it is a sunny day or a cloudy day. This difference further suggests that the increase of wind speed decreases the tensile stress at the bottom more pronouncedly than it does to the tensile stress at the bottom. It also implies that in a less windy condition, the bottom of the slab is prone to fatigue damage.

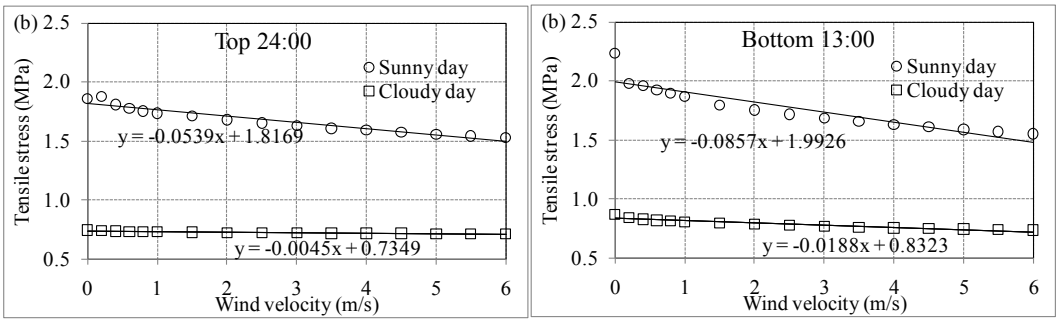

Figure 4.6 Maximum tensile stresses in the JPCP as a function of wind speed.

4.1.5 Heat convection coefficients in different models

Since the wind speed notably affects the temperature development and stress development of a JPCP slab, it is necessary to compare the heat convection coefficients used in different documented models. This coefficient used in the EICM model is computed by Eq. (3.8):

$$h_{conv} = 122.93 * [0.00144T_m^{0.3}w^{0.7} + 0.00097(T_s - T_a)^{0.3}] \quad (3.8)$$

Eq. (3.8) results in a free convection (no wind velocity) at the ground surface approaching zero because h_{conv} vanishes when $w = 0$. This zero free convection goes against the accepted heat transfer theory (Jiji 2009). The most unreliable factor of equation (3.8) is that the slab's surface temperature must be higher than the air temperature, otherwise h_{conv} would be a complex number. Because the sign of $T_s - T_a$ can be either negative of positive (Eq. (3.7) in Section 3.2.3.1), the way the EICM model computes the h_{conv} is questionable.

Priestley and Thurston (Priestley MJN 1979) recommends a simple formula to evaluate the heat convection coefficient as follows

$$h_{conv} = 13.5 + 3.88w \tag{4.11}$$

The free convection in Eq. (4.11) is 13.5W/m^{2o}C, approximately twice of the value (6.855W/m^{2o}C) computed in traditional heat transfer theory (Jiji 2009). This equation also demonstrates that the heat convection linearly increases with the wind velocity. Use of this relationship potentially overestimates the role of wind speed on the heat convection.

Bentz (Bentz 2000) use Eq. (3.9) to predict the heat convection coefficient for concrete:

$$\mathrm{h_{conv}} = \begin{cases} 5.6 + 4.0 \times \mathrm{w}, & \mathrm{w} \le 5\mathrm{m/s} \\ 7.2 \times \mathrm{w}^{0.78}, & \mathrm{w} > 5\mathrm{m/s} \end{cases} \tag{3.9}$$

In Eq. (3.9), the free convection at the pavement surface is 5.6W/m^2 ^{o}C. This value is close to the convection coefficient estimated in the traditional heat transfer theory (Jiji 2009). However, use of the rate of either $\mathrm{w}^{0.78}$ or w overrates the role of wind speed on the $\mathrm{h_{conv}}$.

The heat convection coefficients used in the Bentz model, EICM model, and the Modified Blasius model are plotted in Figure 4.7a. Visually, the coefficient computed from the EICM model is appreciably lower than that from the proposed model and Bentz models. Predicting the pavement temperatures by the use of these models to predict the convection will lead to different predicted results.

Use of the computed heat convection coefficient greatly affects the predicted temperature across the pavement. Figure 4.7b plots the wind velocity versus the slab's maximum temperature on a partly sunny day in July (maximum solar radiation intensity of 700 W/m^2). The slab is assumed in Reno, Nevada. Intuitively, in such a day the maximum temperature ranging from 51 to 55 ^{o}C is unreasonable but from 30 to 45 ^{o}C is more acceptable. In the EICM model, the wind velocity slightly affects the slab's maximum daily temperature. This insensitivity occurs because the heat convection coefficient computed from the EICM model is remarkably less than the other two models (Figure 4.7a). Among other two models, the effect of the heat convection computed from the Bentz model is more pronounced than that from the proposed model. The reason is that the increasing rate of the heat convection coefficient computed from the former model (Bentz model) is greater than the rate of the latter.

Use of the computed heat convection coefficient also influences the predicted maximum tensile stresses in a JPCP (Figure 4.7c and d). A distinction between these models is pronounced at two aspects: (1) the sensitivity of the stress to wind speed and (2) the magnitude of the predicted stresses. First, the maximum tensile stresses estimated from the EICM model become less sensitive to the wind velocity than other models. This is because compared to the other two models, EICM model results in the heat convection coefficient being insensitive to the wind speed. Second, the maximum tensile stress estimated in the EICM model is always higher than the other two models. During the

nighttime (Figure 4.7c, tensile stress at the top occurs at nighttime), this difference is relatively less pronounced because the $T_s - T_a$ during the night hours is comparatively lower. During the daytime (Figure 4.7d), the difference becomes more notable because a relatively high of $T_s - T_a$ (induced by the solar radiation) magnifies the role of the heat convection on the heat loss from the pavement.

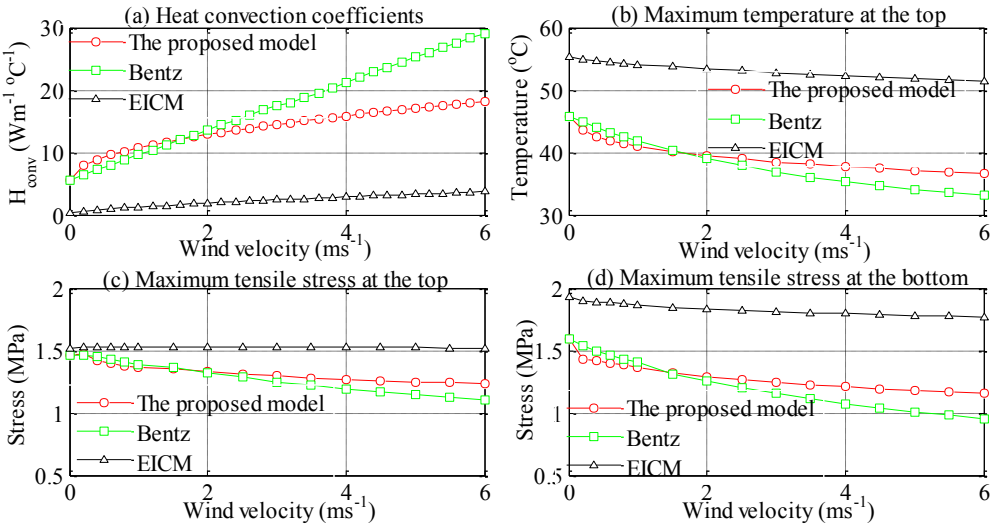

Figure 4.7 Difference heat convection coefficients and their impacts on the temperature and stress through a slab.

4.2 Discussion

4.2.1 What the ways to estimate the heat convection coefficient tell us?

The predicted pavement temperatures from the EICM model are insensitive to the wind speed but are sensitive to the slab's thermal properties, e.g. thermal conductivity. As plotted in Figure 4.7, the predicted results from the EICM model exhibits less variation in range of 0m/s to 6 m/s. The insensitivity may help explain, in part, the extreme sensitivity of the EICM model's prediction to the slab's thermal conductivity (J.E. Hiller and Roesler 2008; Johanneck and Khazanovick 2010). The higher the thermal conductivity, the lower temperature gradient developed in the pavement slab. A slab with higher thermal conductivity facilitates the absorbed heat downward propagating to the bottom of the slab, making the slab having a relatively uniform temperature gradient. Conversely, lowering the slab's thermal conductivity will greatly increase the temperature gradient development within a slab. The EICM model underestimates the heat loss from the pavement surface. It thus results in heat retentions at the top of the pavement, increasing the thermal gradient and subsequent thermal stress developed. Therefore, the predicted results from the EICM model are sensitive to the variations of the thermal conductivity.

The Bentz model tends to overstate the impact of wind velocity on the heat convection number. This may lead to underestimation of the thermal stresses in the slab, especially in high wind speed. As shown in Figure 4.7a, the h_{conv} computed from Bentz model linearly increases with the wind speed. It means that the wind speed can infinitely decrease the slab temperature. This goes against the accepted heat transfer theory. The proposed model should be a more accurate formula to evaluate the heat convection at the pavement surface. This is because it relies on site-specific parameters such as viscosity of the air, characteristic length of the JPCP slab, the air's thermal conductivity, air Prandtl number, and wind velocity. Use of the proposed model, however, may be troublesome when the airflow is at turbulent flow levels (>15m/s). Moreover, a specific value for the characteristic length for a pavement slab in a pavement still needs further investigation.

Wind velocity may be troublesome when placing concrete in a fresh state as it may cause significant plastic shrinkage cracking of the mix. Although the increase of the wind velocity in field can reduce the thermal gradients of the slab, it can also accelerate the moisture loss from the slab's top and induces higher undesirable drying shrinkage near the surface. These drying shrinkage-induced stresses are also significant and may compensate or exceed those thermal stresses reduced by the impact of wind. A deep understanding the role of airflow to the pavement performance needs a more sophisticated model capable to capture the wind velocity's impact on the moisture-temperature profiles of a JPCP slab. The role of wind speed on the moisture escape from the pavement slab would be discussed in Section 7.2.1.2.

4.2.2 Does wind speed still greatly influence both the thermal stress and temperature across the slabs in other regions?

Both the discussion in the above section and the predicted results in the Section 4.1 represent only the sensitivity of the slab temperature and slab thermally-induced stress to wind speed in Reno in July 12. In other regions and other seasons, they hardly directly reflect either slab-temperature distribution or slab-stress distribution. It thus merits discussing whether this impact is notable in other regions and other time. The discussion in the following two paragraphs assumes that the proposed model is used.

This impact in other regions depends strongly the available solar radiation. In lower latitude regions, the influence of wind speed on the heat convection at the pavement surface is magnified because the relatively higher solar radiation heats up the ground surface and increases the $T_s - T_a$. In higher latitude regions, the role of solar radiation declines because $T_s - T_$ is of a relatively less value. Temperature development within a slab primarily depends mainly on the air temperature fluctuation. Therefore, the impact of wind speed on temperature development and thermal-stress development relies on where the in-service pavement slab locates.

This impact in other seasons would be lower than that in July. This study uses the weather condition in July to distinct the role of wind speed on the pavement temperature distribution. In other seasons, the solar radiation wanes so that the $T_s - T_a$ decreases. The wind speed only carries limited heat from the pavement surface. It thus plays

unnoticeable roles on the slab temperature distribution and thus on the thermal stress developed through the slab.

4.3 Conclusions

The following points can be drawn through the simulation of the temperature development and stress development of JPCPs experiencing different wind speeds.

- The impact of wind velocity on the thermal stresses in JPCPs depends on the locations of the pavement. In lower latitude region, the solar radiation heats up the pavement surface and increases the difference between the slab surface temperature and the air temperature ($T_s - T_a$). A relatively higher $T_s - T_a$ facilitates the wind drawing more heat from the pavement and thus reduces the temperature gradient and thermal stress development through the slab.
- This impact varies seasonally. In summer the $T_s - T_a$ is maximal and the role of wind speed is magnified. In other seasons, the solar radiation wanes so that the $T_s - T_a$ decreases. The wind speed carries only a limited heat from the pavement surface. It thus plays unnoticeable roles on the slab temperature distribution and on the developed thermal stresses.
- In summer season with less windy conditions, the temperature gradients near the top increase greatly and thus remarkably raise the tensile stress at the bottom during the daytime. This stress exceeds the tensile stress at top during the nighttime. Therefore, pavement in less windy conditions potentially suffers from greater tensile stress at the bottom than the top.
- Use of the heat convection coefficient from the EICM to predict the temperature profile of a slab tends to produce increased thermal stresses in a JPCP. This may help explain some of the sensitivity of the coefficient of thermal expansion to the predicted fatigue cracking performance in JPCPs. Moreover, the EICM heat convection formula embeds an assumption that the temperature at the pavement surface must be higher than the air temperature. This assumption is not always true and results in the thermal stresses being less sensitive to wind speed. The proposed model considers the factors of the viscosity of the air, characteristic length of the JPCP slab, the air's thermal conductivity, air Prandtl number, and wind velocity. It tends to be more realistic in characterizing the heat convection coefficient for a JPCP structure.

Chapter 5 Impact of solar radiation[3]

Temperature distribution of in-service pavement slab depends on both the incoming solar radiation (SR) and the slab's short-wave surface absorptivity (Richardson and Armaghani 1987; Hermansson 2000). The available SR directly influence the pavement temperature because it heats up the slab surface directly (McCullough and Rasmussen 1999; Bentz 2000; Ge 2005). This absorbed heat is partially inherited and stored underneath the pavement surface layer (Asaeda et al. 1996). The inheritance reflects as a net heat loss in the winter season and a net heat gain in warmer seasons. Heat absorption at the pavement surface also depends on the slab's short-wave surface absorptivity (SA). This absorptivity determines the amount of the absorbed heat because it is directly multiplied to the available SR. For rigid pavement, the SA usually is not a constant. It ranges from 0.65 to 0.85, depending on the texture, color, and worn conditions of the pavement surface. The impact of the SR absorption on the slab pavement temperature distribution thus merits a deep investigation.

Further researches are still required to understand the detailed amount of daily solar radiation and to estimate the impact of heat history on a pavement slab. Firstly, the available SR to a numerical heat transfer model has not gained adequate attention. For short-term predictions, McCullough and Rasmussen (1999) proposed a SR of 300W/m^2 on cloudy days and 1000W/m^2 on sunny days. Use of these SR values overlooks the preceding-date thermal conditions of both the pavement surface layer and its underlying layers. For a long-term prediction, documented literature usually fails to provide details concerning the input of the available SR (Asaeda et al. 1996; Masad et al. 1996; Minhoto et al. 2005; Yavuzturk et al. 2005). At a specific site, the inputted SRs in a specific year should be parameters consisting of both deterministic and probabilistic factors. The deterministic factor is the monthly mean SR, a series ranging from a peak value in summer to a nadir value in winter. The probabilistic radiation swings between the observed monthly maximum and minimum SR. Secondly, the degree to which the SR history affects the temperature distribution and thermal-stress distribution through the slab needs further investigation. Asaeda et al (1996) studied the heat storage effects on the temperature profile across a concrete slab, but failed to study the resulting stresses developed in the slab. Kannekanti and Harvey (2006) used the EICM and MEPDG models to simulate the impact of absorptivity on the predicted pavement distress, but the degree of heat storage was neglected.

This chapter estimates the effect of the SR on the slab temperature distribution and thermal stress distribution through a JPCP slab. Temperatures through both the slab and underlying layers are evaluated by the one-dimensional heat transfer model proposed in Chapter 2. Yearly inputted SR at the pavement surface is computed by the combination of the monthly maximum, mean, and minimum SR observations in the field. This computation assumes that the SR variation during a month follows a random normal

[3] The Material contained in this chapter has been accepted for publication in KSCE Journal of Civil Engineering. The copyright permission is included in Appendix B.

distribution, whose standard deviation depends on the uncertainties of the field observation. Considering that the SR is available only between the sunrise/sunset times, this study also evaluates whether using different sunrise/sunset algorithms affects the predicted temperature through a slab.

5.1 Results and discussion

The following simulation assumes the pavement locates in Reno, Nevada, USA. It estimates the temperature distribution and thermal-stress distribution of a JPCP slab. Figure 5.1 plots the inputted air temperature, relative humidity, and wind speeds. Any data other than on the data-recording date is calculated by the use of cubic spline interpolation. The relative humidity is used to compute the dew point by use of the Eq. (2.5). The daily peak value of the inputted SR, computed by Eq. (2.14), is plotted in Figure 5.2. Due to the uncertainty of the field observations, the variations of the SR in some cases are out of the range between the $q_{max}$and q_{min}. The used SA is 0.85.

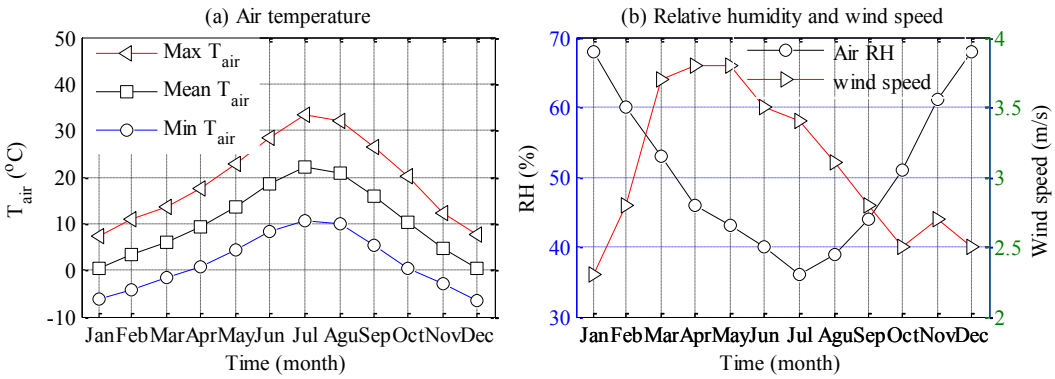

Figure 5.1. Inputted meteorological data for the pavement in Reno, Nevada, USA for (a) Air temperatures, and (b) air relative humidity and wind Speed.

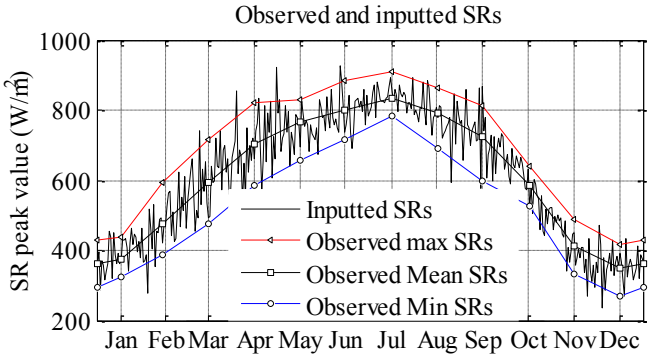

Figure 5.2. The observed and inputted solar radiation.

5.1.1 Slab temperature distributions during summer and winter seasons

SR dominates the slab temperature distributions. Figure 5.3 plots the predicted 24-hour temperatures through the depth of pavement during the maximum SR days in January and July, respectively. Pavement slab in a summer season (Figure 5.3b) is remarkably hotter and experiences higher temperature cycles, compared with the pavement during the winter time (Figure 5.3a). The maximum slab-surface temperatures are approximately 48°C in summertime and 16°C in wintertime. Although the air temperature amplitude (maximum – minimum monthly temperature) through the year is almost the same (Figure 5.2a), the pavement-surface temperature amplitudes are vastly different at 22°C in January and 34 °C in July. In summertime, this hotter state and higher daily-temperature amplitude are due to the increased SR notably amplifying the pavement temperature during the daytime.

Pavement in summer experiences greater temperature gradient than in winter. The maximum positive gradients are about 12°C in January but 18°C in July. The maximum negative gradients were -8 and -12°C in January and July, respectively. These different temperature gradients also present in the level of non-linearity of the temperatures. This level is much higher during the summer months in comparison to the winter month, as denoted by the spacing of the contour lines (Figure 5.3). This is because the absorption of SR increases pavement surface temperatures immediately but it takes a longer period of time to warm deeper portions of the slab.

5.1.2 Thermal stress regime of JPCP

The stress computed in this section uses the stress computational method proposed in the Section 4.1.3.1. All the used parameters are the same. Here, only the total thermal stress is concerned.

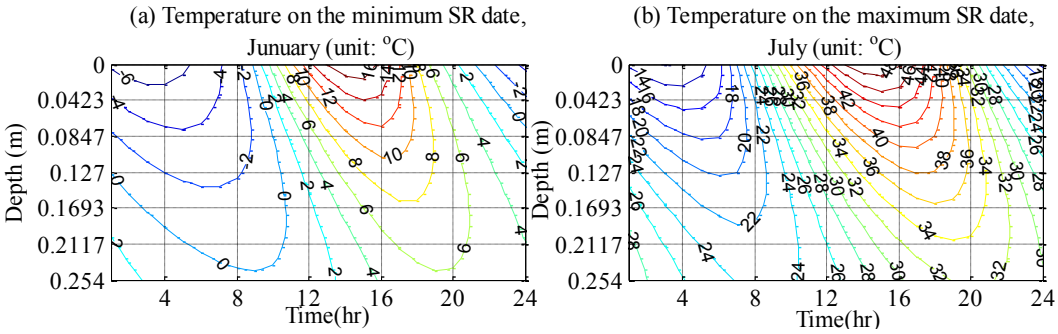

Figure 5.3. Slab's temperature distributions in the maximum SR days of both January and July.

5.1.2.1 Thermal stresses during a daily cycle

JPCP slabs in the summer season suffer from higher stress cycles than in the wintertime. Figure 5.4 plots the predicted slab stresses over a 24-hour period during the

maximum SR days in January and July. At the top of the slab, the maximum compressive stresses are -2.0 and -2.4MPa in January and July, respectively; the maximum tensile stresses, 0.8MPa and 2.0MPa. Similarly, the slab's bottom suffers from more aggressive stress state in July than in January.

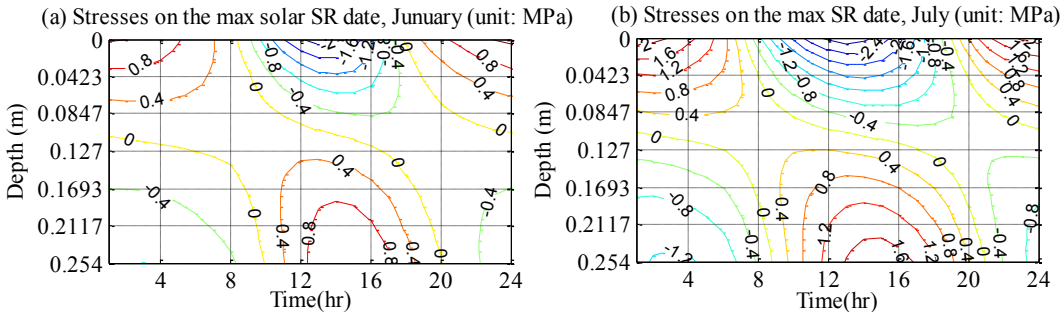

Figure 5.4. Predicted stress distribution in JPCP slabs during the maximum SR days in (a) January and (b) July (Tensile is Positive);

Both tensile and compressive stresses are lower than typical Portland cement concrete strengths. However, according to the exponential characteristic of the Paris Law (Paris et al. 1999), thermal stresses would greatly increase fatigue damage of the slab. This is because when combined with external loading stresses from traffic, the amount of tensile thermal stress makes the total stress of a slab close to the flexure tensile strength.

Figure 5.5 plots the monthly maximum thermal tensile stress in a JPCP slab. It indicates the following points:

1. The maximum tensile stresses are relatively lower in January and December. They gradually increase from the winter to summer seasons, having a 2.3MPa peak tensile stresses at the top of the JPCP slab in July.
2. The top of a slab undergoes higher maximum thermal tensile stresses than the bottom.
3. The pattern of maximum tensile thermal stresses that a slab suffers from is similar to the pattern of the inputted SR plotted in Figure 5.2.

More tensile stress occurring at the top of the slab verifies the dominated effect of the SR on the temperature distribution and stress distribution in a JPCP slab. Tensile stress at the bottom occurs during the daytime; that at the bottom occurs during the daylight. Because the temperature gradient during the daytime is greater than during the nighttime, the linear component of the temperature distribution should cause more tensile stress at the bottom than at the top. However, this is not the case as demonstrated in Figure 5.5. It means that the level of non-linearity is significant enough to create substantial self-equilibrating tensile stresses that are more prevalent at the top of the slab. This level can be verified the spacing of the contour lines in Figure 5.3, where the top has a denser temperature gradient. This denser gradient at the top further verifies the dominated effect of the SR on the temperature and stress distributions in a JPCP slab.

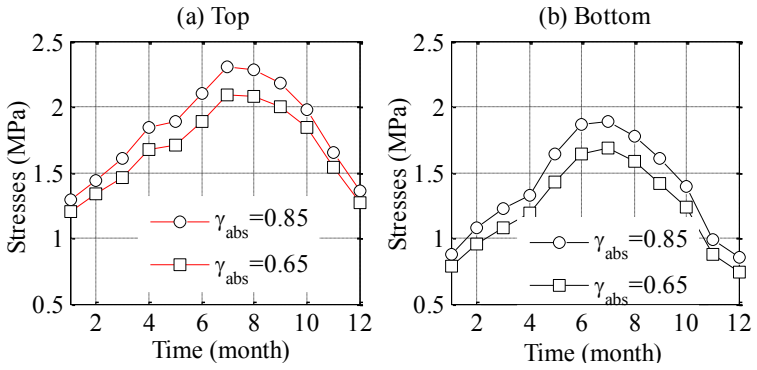

Figure 5.5. Maximum stresses of a slab with different solar absorptivities.

5.1.2.2 Impact of SA on thermal stress development

The solar absorption of slab depends not only on the available SR, but also on the SA. Figure 5.5 plots the influence of different SA (γ_{abs}=0.65 and 0.85) on the monthly maximum tensile stresses developed in a slab. An increase of the slab's SA results in the increase of the developed thermal stress up to approximately 10% in the summer months. At the top and bottom, the maximum stress difference between slabs with 0.65 and 0.85 SA occurs throughout a year. Its magnitude varies with time, having a nadir in January and a zenith in July. This variation further validates the dominated impact of the solar radiation on the stress developed within a slab because solar radiation also has a nadir in January and a zenith at July.

5.1.3 Effect of the used sunrise/sunset algorithm

5.1.3.1 Algorithms to compute sunrise/sunset times

There exist several ways to estimate the sunrise/sunset time of a specific region. The simplest method to compute these times are the used set parameters: sunrise 7:00 and sunset 19:00, sayed R7S19. They are unaffected by the time of the year. Another option is an estimated sunrise/sunset (ESS) time, neglecting solar ecliptic and solar mean anomalies. It is proposed at the algorithm of Eqs. (2.10) to (2.13). A more precise and complicated algorithm (Hill and Braun 2001) estimates the sunrise/sunset time by considering the solar mean anomaly, solar ecliptic, and other factors. This algorithm is noted as the Julian Date of sunrise and sunset (JDSS).

Here uses of these three ways to estimate the sunrise/sunset times in Reno, Nevada, USA (latitude = 39.52^o). Figure 5.6a plots the inputted sunrise/sunset times in Reno, Nevada, USA. The ESS times and the JDSS times are quite similar but are notably different from the constant R7S19 times. The maximum deviation of R7S19 times from JDSS times are approximately 1.5 hours, which potentially either over or underestimate the SR absorbed in a JPCP depending on the season.

5.1.3.2 Effect of different sunrise/sunset algorithms on the numerical results

The standard results can be set as the numerical results predicted by the proposed heat transfer model that uses the JDSS time. This is because the JDSS times precisely characterize the local time available for SR. These standard results are used to verify the feasibility of using either simpler ESS of R7S19 sunrise/sunset time model. When an individual sunrise/sunset time is used, the predicted slab's temperatures (one-hour intervals) can be saved as matrix with elements of $24 \times 21 \times 12$ (24—hours of a day, 21—the total discrete-element nodes of the slab, 12—the monthly maximum SR days). That is, three matrixes are obtained. Each of them is rearranged by the same arrangement method to be a vector. The calibration is conducted by use of the standard result as the X-coordinate and use of the other two vectors as the Y-coordinate.

Use of different sunrise/sunset models does not appreciably influence the slab's temperature prediction (Figure 5.6b). When slab's temperatures are predicted, using ESS as the inputted sunrise/sunset times obtains almost the same temperature predicted by the use of JDSS. The results predicted by use of the R7S19 model also agree well with by use of the JDSS model, although the scatter of predictions is slighter larger. Even though the highest source of error between these two methods occurs at extreme temperature approaching 50°C, these deviations count only for a small portion of the prediction, as demonstrated on the regression R^2 list on the Figure 5.6b. Therefore, the prediction using the R7S19 model is still fairly accurate even though these times deviated by almost 1.5 hours in extreme cases.

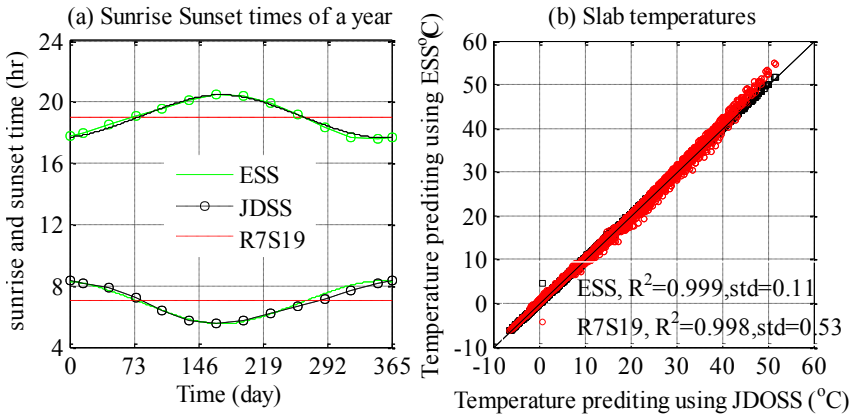

Figure 5.6 (a) Difference between sun time algorithms and (b) their impact on the temperature distribution of a slab.

Use of different sunrise/sunset models does not affect the slab's temperature prediction owning to three seasons. First, amount of the available SR to the slab surface is the same during a day period regardless of the used sunrise/sunset algorithm. This is because this amount is determined by the observed solar radiation is provided by q_{max}, q_{mean}, and q_{min} but not by the use of the sunrise/sunset algorithm. This same energy absorption results in the thermal budget of a pavement structure being unchanged even

though different sunrise/sunset times are used. Secondly, although the sunrise/sunset times computed from each algorithm are different, the specific times of the peak SR are almost the same (13:00). Thus, the maximum temperatures recording during the midday are similar. Finally, the available SR at or around the sunrise/sunset times are relatively low. Therefore, the SR-relative heat flux at the pavement surface around the sunrise/sunset times is minimal when compared with the heat convection and thermal irradiation near hour 13:00.

5.1.3.3 Applicability of the sunrise/sunset algorithm

Using the above algorithms to compute the sunrise/sunset times in high latitude regions (approximately > 65^o) can bring troublesome results. The R7S19 times are out of use in regions such as Alaska, which experiences polar night in winter and undergoes polar days in summer. The computation of the JDSS and ESS time requires Eq. (2.12), in which w_o must be in the range of -1 to 1 in order to satisfy the limitations of Eq. (2.10). However, if assuming the latitude φ is 68 ^{o} and sun declination is 23^o, $w_o = -1.21$ occurs and thus Eq. (2.12) provides unreasonable results. Therefore, all of these algorithms to compute the local sunrise/sunset times at high altitude regions should be used with caution.

5.1.4 Effect of SR history

Because SR dominates the slab's temperature distribution, it is necessary to investigate the influence of the SR history on the temperature dsitribution and stress distributions within a JPCP slab. Heat absorption of slab's surface is partially dissipated to the air and partially transferred downward to heat up the remaining portions of the slab (pavement bottom and underlying layers). Some fractions of the downward transferred heat possibly stores in the ground during the warm season and then dissipates in the subsequent cold season. The history of the SR potentially influences the thermal response of a rigid pavement.

To characterize this influence, a simulation of six continuous days with different weather conditions is conducted by replacing the six continual inputted peak SRs in Figure 5.2 with artificial peak SRs. As shown in Figure 5.7, the days of 1st (July 15) and 2nd day are set as sunny days, and the subsequent 3rd and 4th days are set to cloudy days (Note: 1—July 15, 2—July 16, etc; 1, 2, 5, 6 are Sunny Days; and 3, 4 are Cloudy Days). After the 4th day, the 5th and 6th day is set to sunny days. A sunny day has a SR peak value of 1000 W/m^2; a cloudy day, 300 W/m^2(McCullough and Rasmussen 1999).

5.1.4.1 SR history impact on temperature distributions

SR history affects the slab's temperature, most notably at the bottom**.** Figure 5.8 plots the temperatures at the top and bottom of a slab on the 3rd, 4th, 5th, and 6th date. For the cloudy days, the slab-top temperatures on the 3rd day, which is preceded by a sunny day, are slightly higher than that on the 4th day. For the sunny days, the slab-surface temperatures on the 5th date, preceded by cloudy day, are slightly lower than those on the

6th date. Compared to the top, the impact of the SR history on the slab-bottom temperature becomes more pronounced (Figure 5.8a and Figure 5.8b). For instance, the slab-bottom temperatures on the 4th date are approximately 3-4^{o}C lower than those on the 3th day.

This pronounced impact is due to the heat dissipation at the top being at a higher, more effective way than the bottom. One factor of the heat loss from the top is the heat convection and thermal irradiation. Another factor is due to the absorbed heat transferring downward to heat up deeper portions of the slab. Therefore, although the surface absorbed considerable levels of SR, the slab surface is only slightly affected by the SR history of previous days. Conversely, the heat loss and gain cycles of the bottom are blocked by both the slab and the underlying soils. They thus occur indirectly and slowly. This time-dependent process records the SR history (especially short-term SR history) at the bottom of the slab.

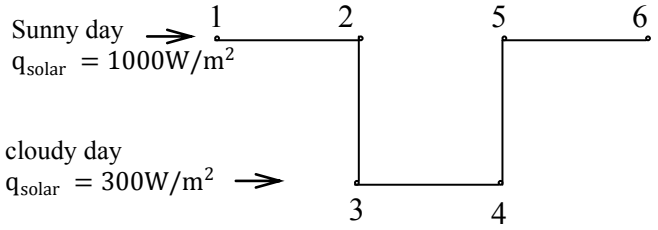

Figure 5.7 Simulated weather changes during a simulated 6-Day period.

5.1.4.2 SR history impact on JPCP thermal stress

The impacts of the SR history on the slab's thermal stress are visualized at Figure 5.9. At the top of the slab, the slab's thermal stresses on a day preceded a sunny day (σ_{3rd}, 3rd day) is 0.1-0.3MPa higher than those on a day preceded by a cloudy day (σ_{4th}, 4th day). At the bottom of the slab, this difference has an opposite sign, ranging from 0-0.1Mpa. Since the heat of slab on the 3rd day is inherited from the sunny 2nd day, this inheritance results in an equilibrated negative gradient being built in the slab for the 3rd day. This gradient leads to a higher tensile stresses at the slab top and a lower tensile stress at the slab bottom.

Conversely, a sunny day experiences higher thermal stresses at the top and less stress at the bottom if it is preceded by a cloudy day. In this case, an equilibrated positive gradient is built in the slab because the preceding two cloudy days cools the bottom of the slab. Compared with the thermal stresses on the 6th date (σ_{6th}), those on the 5th day (σ_{5th}) are lower at the top and higher at the bottom. For this simulation, the SR from the preceding day can result in thermal stress changes ranging from $\pm$0.3MPa at the top and $\pm$0.1MPa at the bottom of the JPCP slab.

Thermal stresses depend on the mechanical properties, e.g., Young's modulus and Poisson ratio; and they also rely on the construction conditions, e.g., slab thickness and slab dimension. The impact of the heat history on the thermal stress development through other slabs may be different from the stresses plotted in Figure 5.9. But the value of the

thermal stress will not vary appreciably. One reason is that both Young's modulus and Poisson ratio of normal Portland concrete slab does not vary greatly even though difference water-to-cement ratio is used (Mindness et al. 2002). Other reason is that the stress correction factor (C_x and C_y) is insensitive to variations of the slab thickness and slab dimension (Westergaard 1927; Bradbury 1938). In others words, C_x and C_y vary slightly when slab's thickness increases from 25cm to 30cm (normal thickness). Similarly, a slab with 3m*6m has almost equal C_x and $C_y$with other slab with 4m*7m (smaller dimension like 1m*1m slab are out of the scope of this study).

5.1.5 What the dominant role of SR on slab temperatures tell us?

5.1.5.1 Impact of SR on heat transfer model in long-term slab-temperature prediction

The impact of SR absorption on the slab temperature distribution suggests that selection of the inputted yearly SRs is crucial in numerically predicting the environmental loadings that rigid pavements suffer from (Qin and Hiller 2011c). Currently, the EICM model embedded in the MEPDG repeatedly uses the observed solar radiation as the SR input when long-term temperature profiles of a rigid pavement are predicted (MEPDG 2004). This repeated use ignores the occurrence of small probability events. Extreme cases such as a summer day with a maximum SR of 1200 W/m^2 or such as continual 10-or-even-30 sunny days may not occur during a particular year observation. But they may occur during a 10 or 20 year observation. Therefore, a rational prediction of the thermal loadings of the rigid pavements may need considering the probabilistic factors of the input solar SR.

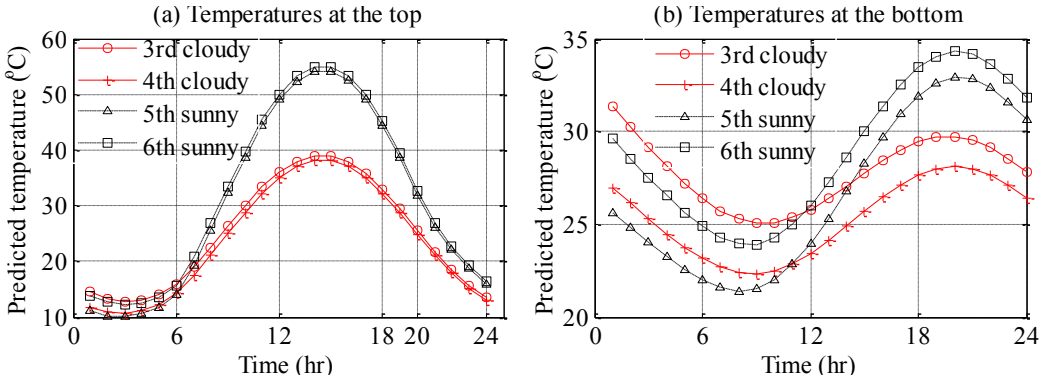

Figure 5.8. Influence of heat history condition of a JPCP on slab temperatures development.

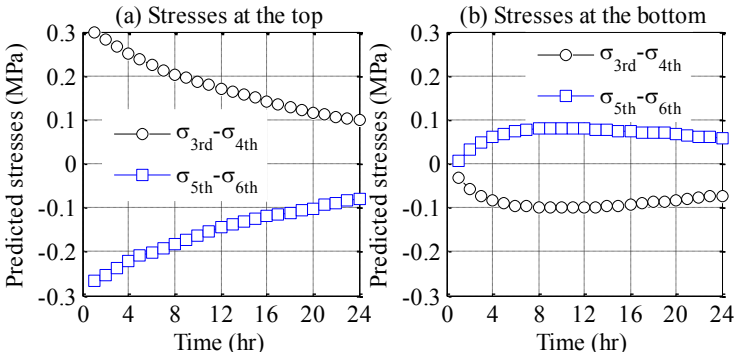

Figure 5.9. The effect of heat history on the stress developed in a JPCP slab (a) top and (b) bottom of a JCPC slab.

5.1.5.2 Estimations of pavement surface temperature

The negligible impact of the heat history on the pavement surface temperature delivers two signals. Firstly, estimation for the maximum/minimum yearly temperature at the pavement surface (such estimation is of extreme importance to asphalt pavements) requires only simulation of the temperature on the maximum/minimum SR days. Pavement surface temperatures are primarily controlled by the current SRs but are negligibly influenced by SR history. This suggests that the extreme pavement surface temperatures must appear on the extreme SR days. Estimate to the maximum pavement surface temperature, however, needs the long-term local SRs, which are influenced by the observational uncertainties of the climatic data.

Secondly, reproducing the observed temperature results of a pavement slab is possible. This type of reproduction can help verify the proposed numerical model which aims to simulate the pavement temperatures and subsequent thermal stresses. In documented literatures that model the pavement slab temperatures, details concerning inputted parameters such as solar radiation are usually not stated (Hermansson 2000; Minhoto et al. 2005). Since the inputted SR strongly affects the temperature distribution through a slab, any attempt to reproduce the results of a documented heat transfer model must estimate the inputted SRs. Reproduction of these models requires intelligent deductions for the peak solar radiation values assigned to the specific day by the use of the observed pavement surface temperature. This is because this temperature is less affected by the solar radiation history (Figure 5.8).

5.1.5.3 Evaluation of pavement surface's absorptivity

Correctly predicting the thermal loadings on rigid pavements also requires a rational estimate to the evolution of the slab-surface thermal properties. Use of a constant SA in EICM tends to overestimate the developed thermal stresses across the slab (not just JPCP) in the first serviced period of a pavement. Currently the EICM model assumes a 0.85 SA for rigid pavement slabs. However, measured SAs ranging from 0.5 to 0.65 have been observed (Levinson and Akbari 2002; Kannekanti and Harvey 2006; Gui et al.

2007). As materials become designed to limit urban heat island effects, the SA of the concrete surface will be designed to start and remain at a lower value. In the EICM, a lowered SA of an actual field pavement slab would lead to an over-prediction of the developed thermal stresses and to an unconservative design. The amount of the overestimation of this thermal stress depends on the available solar radiation.

An evolvable, variable inputted SA to the EICM model may be an alternative to allow better predictions of the temperature profiles and subsequent performance of a rigid pavement. According to experimental research (Levinson and Akbari 2002), the matured SA of an unexposed and abraded concrete slab depends on the albedos of the concrete's components including aggregates, cement, etc. Allowance of a flexible SA input will help the pavement engineer provide better input to the thermal model, according to the used concrete mixture. It also help estimate the subsequent predicted performance, e.g., faulting, transverse cracking, etc., of a rigid pavement.

To illustrate the effect of the SA on the slab's temperature distribution, this study artificially set the SA to 0.65 and 0.85. However, the process and rate of SA evolution of in-service concrete slabs remains unknown. This SA evolution may be affected by factors such as the abrasion of open traffic, the soiling and wetting of local climate, further hydration, aggregate polishing, carbonation, etc.

5.2 Conclusions

This chapter reaches the following conclusions:

- The SR absorption at the pavement surface dominates the temperature distribution and thermal-stress distribution through a slab. In summertime, pavement experiences higher temperature gradients and suffers from higher thermal stress, compared with winter months.
- The role of SR absorption on the slab surface becomes more pronounced when pavement surface became darkened. The maximum thermal tensile stress of a slab can increase up to 0.3MPa when the pavement surface's solar absorptivity rises from 0.65 to 0.85.
- Algorithms to predict the sunrise/sunset times through a given year do not influences the predicted temperature distribution and predicted thermal-stress distribution through a slab servicing in middle and low latitude regions. They may become unreasonable when the pavement temperatures at higher latitude regions require estimation.
- Heat history of slab can remarkably affect the temperatures of the bottom of a slab. When the weather shifts from a sunny day to a cloudy day, an equilibrated negative gradient is induced in the slab. Conversely, an equilibrated positive gradient develops in the slab when the weather shifts from a cloudy day to a sunny day. Multiple days of cloudy weather can amplify these gradients because continuous cloudy days lead to more cold energy stored under the slab. The SR from the preceding day can results in a $\pm$0.3MPa variation in thermal stress at the top and $\pm$0.1MPa at the bottom of the slab.

- Impact of the heat history on the pavement surface is negligible. The computation of the maximum pavement temperature thus requires only predicting the pavement temperature in the day with an extremely high solar radiation. However, estimates of this extreme solar radiation needs consideration due to the observed uncertainties of site-specific weather.

Chapter 6 Slab-moisture prediction: model development and verification[4]

Relative humidity (RH) of an in-service concrete slab is tied to both durability and performance of concrete including drying shrinkage, chloride ion ingression, sulfate attack, etc. Field observations of this internal humidity generally can lose its representation because the observation is concurrently affected by local weather conditions and their probabilistic nature. Extrapolation of this observation to other regions or other time periods potentially leads to delusive interpretation. Moisture distribution within a slab is thus more practical to be predicted through a numerical model, particularly for design purposes. Certainly, such a model involves determining the drying and wetting events on the slab surface. Drying cycles involve moisture loss from the slab, whereas wetting process governs the moisture gain. A model capable of credibly characterizing these loss and gain processes could then provide reasonable predictions of the pore moisture through the slab.

Numerical simulations have been extensively conducted to study the moisture transport within concrete (Z. Bažant and Najjar 1972; Xi et al. 1994; Bazant 2001); but only a few adopted a variable boundary condition. Bazant proposed a highly nonlinear formula to characterize the moisture transport within a concrete structure at both saturated and unsaturated states (Bazant and Najjar 1971; Z. Bažant and Najjar 1972; Bazant et al. 1982). These studies normally adopted a constant ambient air RH because the used concrete structure was shielded from cyclically-wetting and -drying events. However, this controlled boundary condition can not reflect the boundary of in-service concrete slabs. These slabs experience uncertain rainfall events, varying ambient air RH, and stochastic local wind speed. Inability to accommodate these environmental factors in a model aiming to predict slab's pore humidity impedes the understanding of stress distribution and performance in concrete pavements.

This study proposes a numerical model to simulate the moisture distribution within in-service concrete slabs, considering the occurrences of the wetting and drying cycles. The model accommodates the local wind speed, ambient air relative humidity, rainfall pattern, etc. It is verified by use of the observed pore humidity of concrete prisms and by use of field recorded RH through an in-service slab.

6.1 Model development

6.1.1 Moisture transport equation

A one-dimensional finite element model suffices to simulate the moisture transport within the concrete slab because the width and length of the slab is typically an order of magnitude greater than its thickness. The moisture content within concrete can be termed

[4] The material of this chapter, excluding the Section of 6.2.3, has been submitted to journal of Construction Building Material for considering publication.

as RH (unit, 1). According to the law of mass conservation, the moisture transport equation can be expressed as (Jin-Keun Kim and Lee 1999):

$$\frac{\partial RH}{\partial t} = div(D \cdot grad(RH)) - \frac{\partial RH_s}{\partial t} \tag{6.1}$$

where $RH = RH(t, z)$ is a function of time and depth; moisture diffusivity D (m^2/s) is a function of both humidity and porosity of concrete (Jin-Keun Kim and Lee 1999; Chunqiu Li et al. 2008a); and t is time, s; $\partial RH/\partial$□ is the RH's dissipation rate, which depends on the hydration rate for early age concrete. For hardened concrete, $\partial RH/\partial t = 0$.

At saturation, capillary suction dominates the moisture transfer within concrete, whereas at unsaturated conditions, vapor- and gas-pressure gradients govern (Hall 1989). Slab moisture diffusion thus depends on the pore moisture. This non-linear moisture transport can be characterized by an effective diffusivity (Z. Bažant and Najjar 1972):

$$D = D_0(\alpha_0 + \frac{1-\alpha_0}{1+(\frac{1-RH}{1+RH_c})^n}) \tag{6.2}$$

where D_0 is the moisture diffusivity at saturation; n is a regression coefficient describing nonlinearity of the diffusivity with respect to RH, ranging from 6 to 16 for concrete (Leech et al. 2003); $\alpha_0 = D_1/D_0$, where D_1 is the diffusivity of concrete with 0% RH; RH_c, typically ranging from 0.75 to 0.80, is a bifurcate below which the moisture migration occurs owning to gas pressure but above which the migration is driven by capillary suction (Figure 6.1).

Eq.(6.1) needs to be transformed to a normalized equation in order to reasonably simulate the moisture transport within a concrete slab. Moisture diffusivity is orders of magnitude lower than the dimension of the slab, making the condition number of FEM stiffness matrix too large to ensure the transient moisture prediction to be correct and efficient. To circumvent this problem, a dimensionless scale is applied to rearrange Eq.(6.1). This rearrangement begins by introducing the following dimensionless variables:

$$\bar{t} = \frac{t}{t_0}, \bar{z} = \frac{z}{l_0} \tag{6.3}$$

where $\bar{z}$ is a dimensional scale denoting the depth within the slab $0 \le \bar{z} \le 1$; l_0 is the thickness of the slab; t_0 (s) is the characteristic time of the diffusivity, $t_0 = l_0^2/D_0$, $\bar{t}$ is therefore a dimensionless scale referring to the time. Substituting Eq. (6.3) into (6.1) yields:

$$\frac{\partial RH}{\partial \bar{t}} = \frac{\partial}{\partial \bar{z}}(\frac{1}{Pe_m}\frac{\partial RH}{\partial \bar{z}}) \tag{6.4}$$

where Pe_m is the Péclet number regarding mass transport, defined as:

$$Pe_m = \frac{Dt_0}{l_0^2}. \tag{6.5}$$

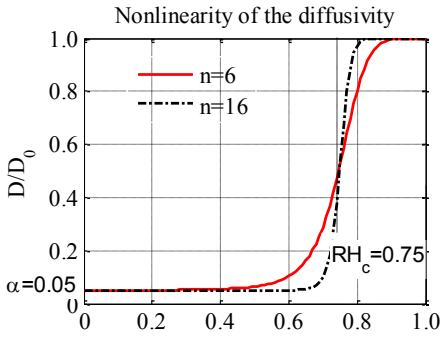

Figure 6.1 Diffusivity and RH according to Eq. (6.2). Note: $\alpha = 0.05$, RH=0.75.

Eq. (6.4) becomes easier to adapt the element length and time step to ensure the convergence of the mass transport Eq. (6.1) (Zdeněk Bažant and Kim 1991). It thus overcomes the singularity of the stiffness matrix in the mass transport model under the finite element framework.

6.1.2 Boundary conditions

For in-service slabs, moisture transport in soil deep in the subgrade is driven by the temperature gradient, capillary force, moisture gradient, etc. The existence of an asphalt or gravel base beneath the concrete slab tends to separate the moisture migration between the PCC pavement slab and the underlying soils. Therefore, modeling the moisture migrations at the slab surface and at the slab bottom is sufficient to estimate the RH through the slab depth.

A numerical solution to Eq. (6.1) thus needs specify a proper boundary condition to both the bottom and the top of a pavement slab. Moisture at the bottom is relatively stable and less affected by the moisture exchange between the slab and the underlying layers, owning to the separated effect of the subbase or subgrade (Chunqiu Li et al. 2008a). In this regard, the bottom of a pavement slab can be considered as a Neumann boundary with null moisture flux ($gradRH = 0$).

The occurrence of wetting and drying cycles complicates the mass transport at the pavement surface. During the drying cycles, the top of the slab is treated as a convection boundary. The moisture convection at the slab surface depends on the ambient air RH, wind speed, RH value at the top of the slab, etc. During the wetting cycles, RH at the top can be set to $RH = 1$ (Z. Bažant and Najjar 1972). The set is practical because although the absorption may dominate the moisture intake in the top and the case of RH>1 may occur therein, the wetting front penetration usually locates at a depth of <1cm in a normal rain event (Z. Bažant and Najjar 1972). An estimate for the upper boundary thus requires:

(1) determination of when the wetting or drying events occur around a year cycle; and (2) characterization of the moisture evaporation rate during the drying cycles.

6.1.2.1 Determination of wetting time and wetting intensity

The time and duration of a specific rainy event need to be known to determine when the top of the slab is wet. Usually, meteorological data collected from weather stations provides the rainfall intensity at that location. Sophisticated statistical models have been proposed to predict the rainfall duration of a specific location (Menabde et al. 1997; Sivapalan and Blöschl 1998; Fife and Nokes 2002). However, these algorithms are fairly complicate and not commonly used by pavement engineers. For concrete slabs, the impact of wetting and drying cycles on the moisture distribution within concrete has typically been limited to laboratory studies (Chrisp et al. 2002) and by arbitrarily setting wetting and drying cycles in laboratory conditions (Kefei Li et al. 2009; Lin et al. 2010).

To remedy this issue, this study proposes a new, simple algorithm to compute occurrence of wetting and drying events. This algorithm is based on a weighted function that uses the observed monthly rainy data as the local rain duration. For example, if the expected annual rain hours are 100hr and if each rain event last only 1 hour, then the probability of rain event in any given hour is 100/8760 provided that the observed monthly rain distribution is uniform. In this case, a specific rainy hour is determined by using the uniform distribution to randomly generate a number from 0-1 and by specifying an hour as a rainy hour if the number is not greater than 100/8760.

However, determination of rainy events at a local site tends to be more complex due to the variation of the rain duration (generally not equal to 1 hour) and due to the non-uniformity of rain distribution. For a specific weather station, the annual precipitation provides both the precipitation-event number and the monthly rainfall intensity. But the duration of each rainy event remains unknown (Western-Regional-Climate-Center 2010). Thus, to determine the rain distribution around a given year, two factors are still required: (1) the duration of each rain event and (2) the annual distribution of these rain events.

6.1.2.1.1 Assumptions to duration of each rain events

This study assumes the rainy duration $l_r(I)$ as follows:

- Rain with 0.254mm intensity (I) keeps the slab surface wet for 1 hour;
- Rain with 1.27mm intensity, for 4 hours;
- Rain with 12.7mm intensity, for 8 hours;
- Rain with 25.4mm intensity, for 10 hours (e.g., $l_r(0.254) = 1$; $l_r(1.27) = 4$, etc.).

6.1.2.1.2 Algorithm to compute the annual distribution of these rain events

Annual distribution of the on-site rainy events is obtained according the local observed monthly rain intensity function $f(t)$ (Western-Regional-Climate-Center 2010), as shown in Figure 6.2a (black dotted line). Here, the steps to determining the rainy event hour r_i in the case of $I = 1.27$ (keep the slab surface wet for 4 hours) are illustrated:

- Randomly produce a 8760-element vector $\{RI_i, i = 1,2 \ldots 8760\}$ according to the uniform distribution (This distribution is applied because the rainy probability in any individual hour should be the equal before knowing the $f(t)$);
- Discretize $f(t)$ to a 8760-element vector $\{\mathrm{f_i}, \mathrm{i} = 1,2, \ldots, 8760\}$ by use of a cubic spine interpolation method; this step adds the seasonal precipitation distribution;
- Compute the percentage p_i of each element in the vector, $p_i = f_i / \sum f_i$ and $\sum p_i = 1$; this step normalizes the seasonal precipitation distribution;
- Determine the rain event index $r_i = \begin{cases} 1 \; l_r * \mathrm{p_i} \leq RI_i \\ 0 \; l_r * \mathrm{p_i} > RI_i \end{cases}$, where $r_i = 1$ and $r_i = 0$ signify that slab surface is wet and dry, respectively. This step detects whether a specific hour is rainy or not;
- Consider the duration of a specific rainy event. If $r_i = 1$, then $r_n = 1, n \in [i-2, i+2)$; this means that if the *i*th hour is detected to be a rainy hour and the rain keep the slab surface wet for 4 hours ($I = 1.27$). This step considers the rainy duration of a specific rainy event.
- Determine the next rainy event by increasing the indices of i from i to $i+2$ (because this rainy duration is 4hr).

In the cases of $I = 0.254mm$, *12.7mm*, and *25.4mm*, the rainy index parameter r_i can be obtained by the same algorithm provided above. For an individual hour, summation of r_i at each case of I yields the annual rainy index R_i (the sum of r_i at $I > 0.254\mathrm{mm}$, $I > 1.27\mathrm{mm}$, $I > 12.7\mathrm{mm}$, and $I > 25.4\mathrm{mm}$). It should be noted that $R_i > 1$ may occur for a specific index i. This occurrence means that the computation of r_i at different I is overlapped. The overlap, however, has a small probability because from most locations, the total wetting events are one order of magnitude less than the total drying events. Despite this, a method to circumvent the overlap issue is provided when the feasibility of the algorithm is verified.

6.1.2.1.3 Verifications of the rainy-duration assumptions and of the proposal algorithm

Verification pertaining to the rainy events in Rantoul, Illinois is conducted to test the feasibility of the proposed method. Figure 6.2 (dotted black data) plots the annual precipitation in this region, while Table 6.1 tabulates the number of annual rainy events. Use the algorithm provided above to compute the rainy events of this region yields the inputted rainy hours series R_i. A regression analysis between the total monthly rainy hours and the monthly rainfall intensity results in a coefficient of determination (R^2) of 0.921. This agreement signifies the feasibilities of the algorithm and that of the rainy duration assumption.

It merits noting that the regression coefficient of determination is a random number because the RI_i is a random 8760-element vector. In this case, denoting a threshold, e.g. $R^2 > 0.90$, could minimize the problem of $R_i > 1$.

Table 6.1 Number and intensity of annual rainy events in Rantoul, Illinois

Location	Number of rainy days (time)			
	I>0.254mm	I>1.27mm	I>12.7mm	I>25.4mm
Rantoul, IL	99	69	26	9

6.1.2.2 Drying condition

6.1.2.2.1 Moisture convection formulation

Moisture convection during the drying process ($R_i = 0$) controls the mass flow at the pavement surface. Its magnitude depends on the concrete's porosity, air humidity, RH of pavement surface, in-situ wind velocity, etc. Influences of these factors on the moisture evaporation of the concrete surface are encapsulated in a widely-used formula named Dalton's formula (Dalton 1802), which is defined as:

$$E_w = F(w)\left(e_{top} - e_a\right) \tag{6.6}$$

where E_w= weight (kg) of water evaporated (kgm^{-2}hr^{-1}),

e_{top}= pressure of saturated vapor pressure at the concrete surface (kPa),

e_a= pressure of vapor pressure of the surrounding air (kPa), and

$F(w)$= wind function at which the local wind speed measured at 0.5m above the evaporating surface (m/s).

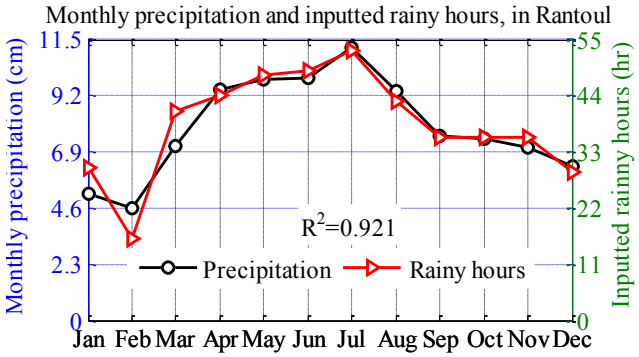

Figure 6.2 Monthly rainfall intensity in Rantoul, Illinois, and the computed monthly rainy hours.

Initially, Eq. (6.6) was used to compute the bleed water escaping from the concrete surface. Its application was then extended to the moisture evaporation over a hardened concrete surface covered by water and to the convection of the moisture when the hardened concrete surface was free from water content (Mather 1985; Yuan and Wan 2002). In this drying case, the difference between air RH and concrete-surface humidity

is regarded as the driving force because in an isothermal condition, RH linearly correlates to the vapor pressure. Using this force, the moisture convection equation becomes:

$$f = g(w)\left(RH_{top} - RH_a\right) \tag{6.7}$$

where f is a dimensionless scale specifying the moisture loss from the slab surface; $RH_{top}$and RH_a are the RH of the pavement surface and the surrounding air, respectively; and for an isothermal problem, $g(w)$, called moisture convection coefficient, is only a function of the wind speed.

$g(w)$ may have a complicate analytical solution. However, it can be approximated to a linear function, as shown in Eq. (6.8), if a direct Taylor expansion as a derivative point of w_0 truncates the higher order terms.

$$g(w) = A(B + w) \tag{6.8}$$

where $AB = g(w_0) - g'(w_0)w_0$ and $A = g'(w_0)$; A and B stands for the capacities of surface emissivity and free evaporation. The use of Eq.(6.9) yields:

$$f = A(B + w)\left(R\square_{top} - RH_a\right) \tag{6.9}$$

6.1.2.2.2 Computation of the near-surface wind speed

Eq. (6.9) raises a question: how to input the wind speed read from a local weather station into the equation? The speed used in Eq. (6.9) should be near a concrete specimen surface (0.5m), whereas both weather stations and local airports often collect wind data at 9m above a flat ground surface. A transformation of the collected wind speed to the wind speed at 0.5m above ground surface can be roughly estimated by Eq. (6.10) (Uno 1998).

$$w = w_{rec}(z/z_{rec})^{1/7} \tag{6.10}$$

where w_{rec} is the recorded wind speed provided by a weather station; z_{rec} (m) is the height at which the wind speed is measured by weather stations, $z_{rec} = 9$; and z (m) the height of the required wind speed w thus $z = 0.5$. Eq. (6.10) thus becomes:

$$w = 0.662w_{rec} \approx 2/3w_{rec} \tag{6.11}$$

Eq.(6.11) indicates that the recorded wind speed provided by a local weather station is one and a half times larger than the wind speed at 0.5m above the ground surface. Therefore, Eq.(6.9) can be rewritten as:

$$f = A(B + 2/3w_{rec})\left(RH_{top} - RH_a\right) \tag{6.12}$$

6.2 Modeling verification

With the moisture diffusivity in Eq. (6.2) and the boundary condition provided in the section 2.2, the analytic solution to both Eq. (6.4) and Eq.(6.1) is unique. Achieving such a solution, however, is difficult and typically has to be solved to a numerical approximation method, such as finite element analysis. In this study, the finite element method used is based on the Galerkin weak-solution framework. The specimen is discretized by 40 quadratic elements. The time step size is chosen as *1hr* as the moisture mass transfer is relatively slow process for low diffusivity materials such as concrete. The cubic spline interpolation is used when an interpolation is needed. The initial RH within the slab is assumed to be 1 throughout the depth of the slab. The Crank-Nicolson method is used to implicitly solve Eq. (6.4) and convergence tests are conducted to verify the accuracy of the results (Ainsworth and Oden 1997). Numerical code for this simulation can be referred to **Appendix D**.

6.2.1 Verification using laboratory data

Laboratory data of concrete prisms observed by Kim *et al* is used to verify the moisture diffusion Eq. (6.4). Details relative to the laboratory observation can be referred to (Jin-Keun Kim and Lee 1999). The predicted values coincide visually and statistically with the observed data, having R^2 values generally over 0.95 (Figure 6.3). This coincidence signifies that the proposed model can accurately predict the moisture diffusion within the concrete specimens. Table 6.2 notes the moisture diffusivity parameters D_0 used to obtain the best fits between experimental and predicted values. With no wind speed in this lab experiment, the verification of the parameters in Eq. (6.12) yields $A \times B = 2.157$. Exact values for A and B require further verification relative to the concrete slabs exposed to natural weather conditions.

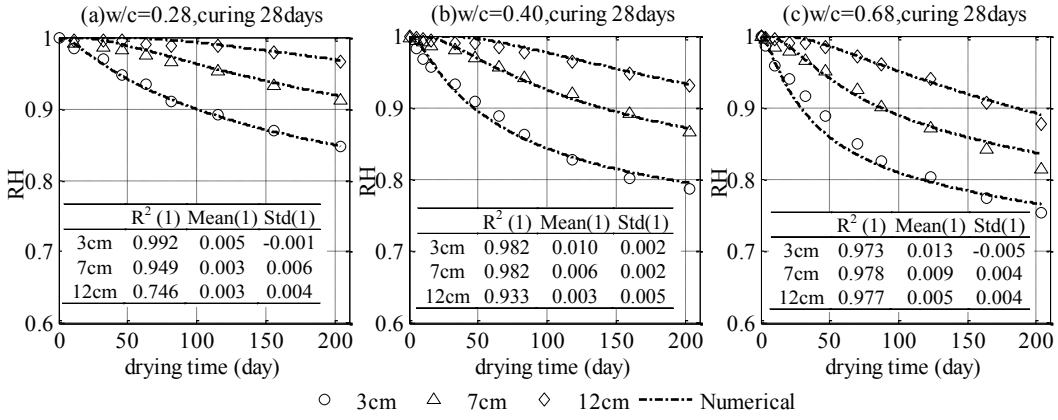

Figure 6.3 Predicted RH compared to the laboratory observed values at different depths; Note: measured data is reproduced from Kim et al (Jin-Keun Kim and Lee 1999).

Table 6.2 Regressed moisture diffusivities (units: $m^2/h*10^{-6}$)

	w/c=0.28	w/c=0.40	w/c=0.68
D_0	0.86	1.59	2.57

6.2.2 Verification using field observed data (isothermal model)

To provide further verification of the proposed numerical model, this study applies relative humidity observed in an in-service concrete pavement at Rantoul, Illinois (Kohler 2005). Weather data in Rantoul is used to compute the wetting and drying condition at this site. The monthly rain hours of this region has been plotted in Figure 6.2. Other weather conditions including the wind speed and ambient air RH are illustrated in Figure 6.4. The initial pore RH through the slab is assumed to be 1.0 uniformly. Due to the use of fly ash in the concrete mix (Kohler 2005), an equivalent water-to-cement ratio of 0.32 was used to interpolate the moisture diffusivity the slab.

The verification indicates that the proposed model can also reliably predict the RH for in-service concrete slabs (Figure 6.5). The verification considers the on-site wind variations and thus the calibration obtains parameter A=40.32. Recalling that $A \times B = 2.157$ in the above section, one can obtain that $B = 0.0537$. Therefore, during the drying cycles, the Eq. (6.12) becomes the following:

$$f = 186.67(0.012 + 0.216 \times 2/3w_{rec})(RH_{top} - RH_a) \tag{6.13}$$

The arrangement of Eq. (6.13) with a term of $0.2162 \times /3w_{rec}$ is used to compare with Menzel's formulas, as shown in Eq.(6.14), that has been widely used to compute the evaporation rate occurring at concrete surface covered with water.

$$E = \alpha(0.253 + 0.216 * 2/3w_{rec})(e_{top} - e_a) \tag{6.14}$$

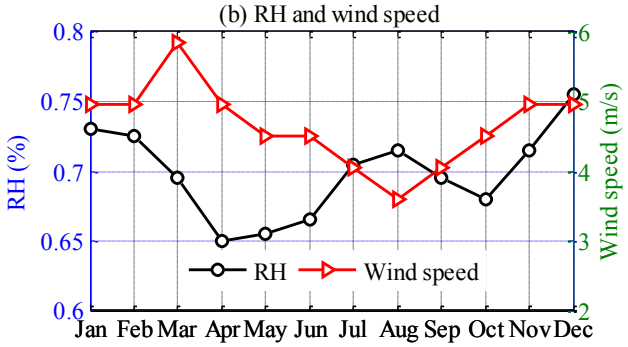

Figure 6.4 Local wind speeds and seasonal ambient air relative humidity in Rantoul, IL.

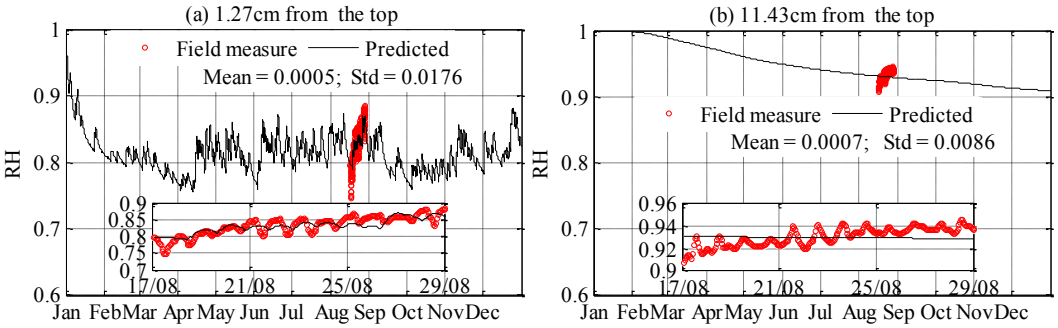

Figure 6.5 Field observation of internal RH and the predicted values. Note: Field data is reproduced from Kohler (Kohler 2005).

6.2.3 Verification using field observed data (couple model)

The verification plotted in Figure 6.5 is based on the moisture predicted from the isothermal model. It means that the daily variation of the local relative humidity is independent to the daily temperature variation. Such verification thus fails to characterize the wiggle of the daily RH variation because the pore humidity increases with temperature.

6.2.3.1 Theoretical basis

Diffusivity D varies with temperature. Theoretically their correlation obeys the rate process theory and can be characterized by the following equation:

$$\frac{D_T}{D_0} = \frac{T}{T_0} exp\left(\frac{Q}{RT_0} - \frac{Q}{RT}\right) = \Phi(T) \tag{6.15}$$

where T is absolute temperature; T_0 is reference temperature (^0K), normally is selected as room temperature; D_T and D_0 are the values of saturated diffusivity at temperatures T and T_0, respectively; Q is the activation energy (enthalpy) of diffusion process. The value of the activation energy was found to be roughly 1300cal/mole for harden concrete.

The pore humidity varies with temperature as well. Because the moisture-diffusion process is orders of magnitude less than the thermal-diffusivity process, the water content within a pore could be seen as a constant during a short period such as an hour. But the temperature during this hour may greatly change. Thus, RH within a slab varies the temperature. The correlation can be characterized by the hydrothermic coefficient κ ($^oC^{-1}$). It obeys the following equation:

$$\frac{dRH_{eq}}{dt} = \frac{dRH}{dt} - \kappa\frac{dT}{dt} \tag{6.16}$$

where the RH is the local pore RH; RH_{eq} is the equivalent pore humidity at temperature of T_0. It merits noting that at varying T and RH, the saturated diffusion D_T should be

estimated by use of RH_{eq} (Z. Bažant and Najjar 1972). That is, the local saturated diffusivity has to be estimated by the Eq. (6.17)

$$D_T = D\left(RH_{eq}\right)_{T_0}\Phi(T) \tag{6.17}$$

In a numerical simulation that considers the varying T, the RH has to be estimate by use of the Eq. (6.16) at each nodal point and at each time step. This estimation still needs the value of hydrothermic coefficient κ (Z. Bažant and Najjar 1972).

This coefficient is always positive because the water content is known to decrease with T at constant RH. The approximate dependence of the κ upon RH can be roughly evaluated by use of Eq.(6.18), according to Bazant (Z. Bažant and Najjar 1972)

$$\kappa = 0.0135RH(1 - RH)/(1.25 - RH) \tag{6.18}$$

A plot pertaining to RH and κ is demonstrated in Figure 6.6. It illustrates that the pore RH is insensitive to temperature variation in both total-unsaturated and saturated states and becomes greatly sensitive when RH ranges approximately from 0.6 to 0.8.

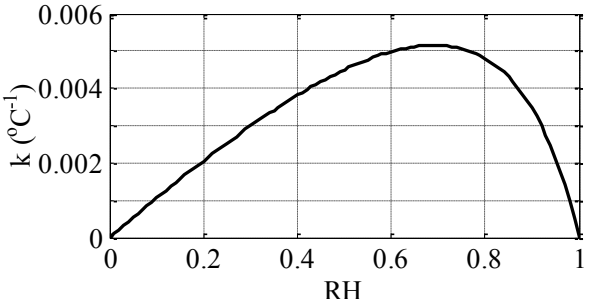

Figure 6.6 Approximated value of hydro-thermal coefficient at different RH.

6.2.3.2 Verify the field measure by use of couple model

The verification, first of all, requires to validate whether the predicted slab temperature coincide with the observed temperature. The validation uses the weather conditions including the wind speed, air temperature, and solar radiation in Rantoul, Illinois, to predict the slab temperature. The verifications are conducted to verify the temperature at depth of 1.27cm and 11.43 cm (Figure 2.5).

Use of the coupling thermal- and moisture- transfer model to predict the pore RH through a slab requires the following procedures (coupled in series):

(1) Predict the slab's temperatures around a specific year;
(2) Provide an initial RH_{eq} through the slab;
(3) Use the predicted temperatures and the previous time-step RH_{eq} to compute the saturated moisture diffusivity D_T by use of Eqs.(6.15) and (6.17);

(4) Input the D_T values (D_T is different across the slab) to Eq. (6.1) and then use the wetting and drying boundary conditions to simulate the RH_{eq} in the next step;

(5) Use the predicted RH_{eq} to estimate the real RH in Eq. (6.16);

(6) Repeat the steps from (3) to (5) to estimate all the RH at all time steps.

Using of the coupling model greatly increases the confidence of the validation (Figure 6.7). In Figure 6.7, the embedded graph manifests that the variation of the predicted RH coincides with the prediction. The statistical regressions also demonstrate better agreement than the results from the isothermal model, which is plotted Figure 6.5.

6.2.4 What the verification tell us?

The drying evaporation rate (Eq.(6.13)) is used to compute the moisture convection at the in-site concrete surface during a drying cycle; the Menzel formula, however, commissions to compute the water evaporation from a bleed water surface. Similarity between both formulas lies in that a coefficient of $0.216 * 2/3$ is multiplied to the observed wind speed from a weather station. The Similarity suggests that in both drying and wetting cases, the wind speed plays a similar role to the water loss from the concrete surface. Both equations have a constant value of f/E if the wind speed is set to zero. This constant is the rigid transform parameter between the vapor water pressure and the relative humidity. The difference between the two formulas reflects in the terms of 0.012 and 0.253. These two constants characterize the free convection coefficients of drying surface and wetting surface, respectively. Therefore, free convection during wetting cycles may be appreciably different from that during drying cycles.

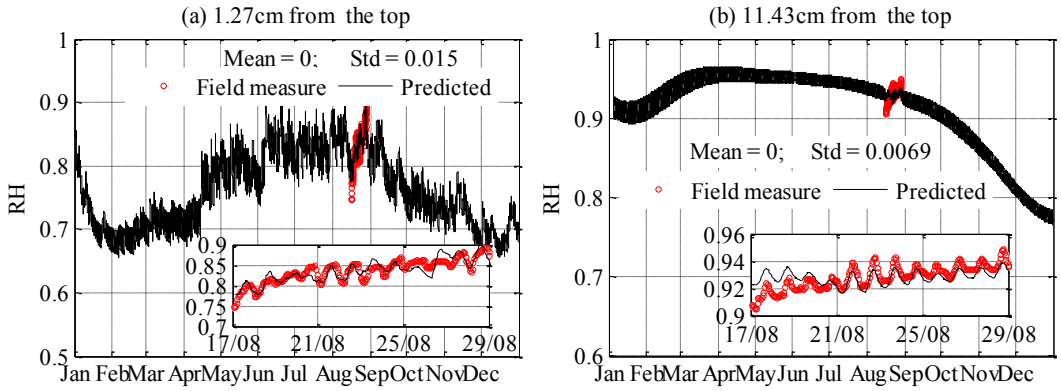

Figure 6.7 Field observation of internal RH and the predicted values by the use of coupled thermal transfer and moisture transport model.

In the case of free convection, evaporation from the concrete surface occurs appreciably during wetting cycles whereas the escape of moisture from a drying concrete surface is negligible. For the wetting condition, both terms of 0.253 and $0.216 * 2/3\mathrm{w_{rec}}$ are similar in magnitude for a range of normal wind speed (w_{rec} = 0~6 m/s). This infers that not only windy weather can lead to rapid water loss from the slab surface, but

free convection can also be significant. Conversely, for the drying condition, free convection plays a secondary role to the decrease of the near-surface moisture. As 0.012 is one-order of magnitude lower than $0.216 * 2/3\mathrm{w_{rec}}$ at lower wind speeds, the escape of moisture from a drying concrete surface is minimal in the case of free convection. This negligible role is verified by the difference between the RH drops in the lab specimen and in on-site concrete slab. For laboratory specimens, Figure 6.3a and b demonstrate that a RH drop from 0.98 to 0.95 needs about 20-40 days at a 3cm depth (*w/c*=0.40 in Figure 6.3b). For in-service concrete slabs, a similar drop of the RH at 1.27cm requires only about 1-2 days (Figure 6.4a). This difference in drying-time scales confirms that during the drying cycle, wind dominates moisture loss from the concrete surface whereas water loss caused by free convection plays a secondary role.

This different role is most pronounced during the period immediately after the wetting concludes. During this time, the difference between RH_{top} and RH_a ($RH_{top} - RH_a$) magnifies the influence of the wind speed on the moisture escape from the surface, as demonstrated in Eq.(6.13). After this time, $RH_{top} - RH_a$ is close to zero and makes the moisture loss less sensitive to the wind velocity.

6.2.5 Differences among pore RH, isothermal RH, and equivalent RH

Until now, the study predicts the RH distribution through in-service slabs using the RH predicted by the isothermal RH (RH_{iso}), the equivalent RH (RH_{equ}), and the real pore RH (RH). Figure 6.8 plots the entire-year predictions that include these three types of RHs at 1.27 and 11.43cm depths of the slab in Rantoul, Illinois. Difference pertaining to these humidity merits notating.

The prediction of RH_{iso} includes an assumption that the temperature within a slab is uniform distribution and is 22^{o}C everywhere. This is not the case even in a region with a calm seasonal temperature pattern. In the case that the activation energy (enthalpy) Q of diffusion process is a lower magnitude such as 100 (J), the diffusivity of concrete depends less on the temperature variation. The moisture predicted from the isothermal model can be close to the equivalent relative humidity of the slab. As show in Figure 6.8, the RH_{iso} is roughly equal to the RH_{equ} when the $Q = 1300$ is used.

The RH_{equ} experiences only a seasonal variation and exhibits negligible daily variations. This is because the heat transfer process with a slab is several orders-of-magnitude greater than the moisture diffusion. In the regard, the RH_{equ} signifies the slab's pore water content, because variation of such content is minimal during a day period.

The RH is the pore RH that can be logged by a moisture sensor such as psychrometer. It reflects the real pore humidity within a slab. This means that under the same water content, an increase of temperature would increase the RH_{real}, and vice versa. As demonstrated in Figure 6.8, during the colder season, the predicted RH_{real} is greatly lower than both RH_{iso} and the RH_{equ}. But during the summer, the RH_{real} is slightly

higher those two because the average daily temperature across a slab is usually larger than 22°C, room temperature.

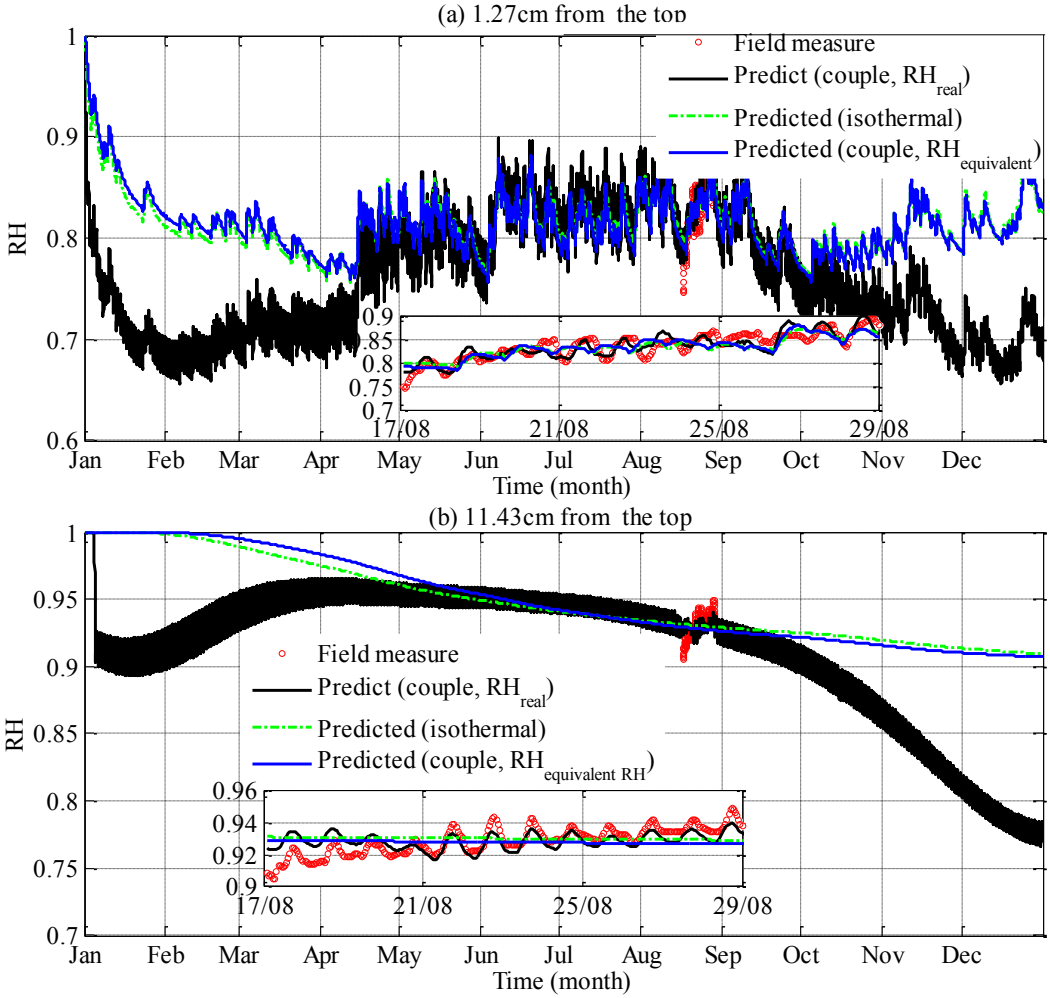

Figure 6.8 RH predicted by the isothermal model, the equivalent RH, and the real RH.

6.3 Conclusions

1) The wind speed observed from a weather station cannot be directly inputted into the Menzel's formula to compute the evaporation rate of bleed water from a casting concrete surface. The observed wind speed of weather stations in most locations (e.g. airports) generally is one-and-half greater than the wind velocity used in Menzel's formula due to the height of the measurements.

2) During wetting conditions, both wind speed and free evaporation (zero wind speed) significantly affect the moisture escape from the concrete surface. During the drying cycle, wind velocity dominates the moisture loss at slab surface, especially during

the transition time that the relative humidity at the top approaches the ambient air humidity. Free evaporation at a drying concrete surface plays a secondary role to the moisture escape in cases with wind at the surface.

3) Variation of the temperature strongly influences pore RH through an in-service slab. Not only does the slab's diffusivity depends on the temperature, but the pore relative humidity strongly varies with the temperature variation. Uses of the relative humidity predicted by the isothermal model or by the equivalent relative humidity (a relative humidity estimated at room temperature) potentially overestimate the slab relative humidity during the cold seasons.

Chapter 7 Slab-moisture prediction: sensitivity study[5]

Relative humidity through the depth of an in-service concrete slab depends on the combined effect of local weather factors including wetting/drying events, ambient air relative humidity, wind speed, etc. Some of these factors may perform a determinative role whereas others possibly act as a secondary role. An investigation to these different roles can help to predict the slab's RH-associated performance in terms of sulfate attack, chloride ion ingress drying shrinkage, warping/curling, and its associated stress development.

Numerical studies of concrete moisture distribution rarely consider a variable ambient RH upper boundary condition (Z. Bažant and Najjar 1972; Bazant 2001; Kefei Li et al. 2009). Lab calibrations of moisture distribution models typically use a constant controlled RH to assess its effect on concrete specimens. However, this stable ambient RH does not properly mimic scenarios for in-service pavements, which experience not only variable air humidity but also wetting/drying cycles. The role of such cycles on the RH in concrete has been cursorily studied by artificially adopting fixed wetting and drying cycles, such as 15 days or 60 days (Kefei Li et al. 2009; Lin et al. 2010). This adoption of fixed cycles neglects the probabilistic nature of the local weather conditions and, to a great extent, fails to truly reflect the impact of unpredictable weather timing on the concrete's RH distribution. It is thus necessary to simulate the impacts of these cycles on the moisture budget of in-service slabs.

This study uses the model proposed in Chapter 6 to simulate moisture distributions through the depth of in-service concrete pavement slabs. It examines the impact of external factors including the rainfall pattern, wind speed and its daily variation, and ambient air RH and its daily variation on the internal RH distribution. It also investigates the impact of internal factors like the water-to-cement ratio (w/c ratio) and examines the sensitivity of the predicted moisture to the adoption of the numerical boundary conditions. The subsequent discussion to the predicted results centers on the following:

- Why the seasonal air RH plays a dominant role on the slab's moisture distribution whereas the other weather factors act only in secondary roles?
- What do these different roles imply with respect to the predicted in-service concrete pavement performance?

7.1 Site information

This study simulates the RH though the depth of a concrete pavement slab located in Reno (RE), Nevada to assess the influence of weather condition. This simulation uses the following parameters, unless otherwise noted:

- Monthly precipitation distribution and inputted rainy hours plotted in Figure 7.1a.

[5] The material of this chapter has been submitted to journal of Construction Building Material for considering publication.

- Ambient air RH and local wind speed shown in Figure 7.2b. During a specific day, the local wind speed and RH is regarded as constants.
- A w/c ratio of 0.45. This ratio is used to interpolate the moisture diffusivity. Other parameters for the diffusivity include $\alpha = 0.10$,$n = 6$, and RH_c=*0.75* are utilized (See in Chapter 6).

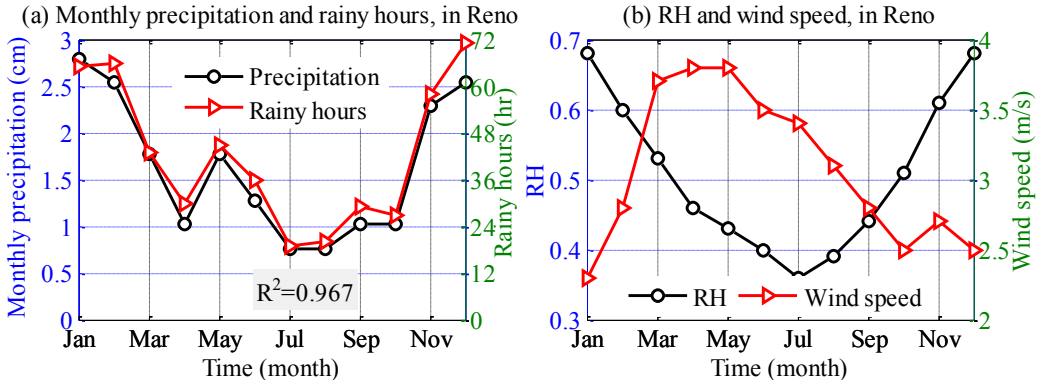

Figure 7.1 Rainfall distribution, air RH, and wind speed in Reno, Nevada.

7.2 Results

Five-year simulations are conducted to examine the evolution of the RH through the slab, beginning with the end of the curing. The curing is assumed terminating at the end of June 30. The initial RH through the slab at this time is 1.0 uniformly. Usually, the RH profiles at the half-time (December 30, 2nd year) and full-time (June 30, 5th year) of the prediction are plotted to demonstrate the difference between the predictions that use different boundary conditions.

7.2.1 Effect of external factors

Relative humidity within a slab serviced in Reno is compared to that Los Angeles (LA) in order to study the impact of the environmental factors on the moisture distribution within in-service slabs. Environmental factors in LA are shown in Figure 7.2. The reason of selecting these two regions is due to their discernable seasonal weather patterns. First, Reno's rainfall pattern (Figure 7.1a) is more uniform than the LA's (Figure 7.2a) whereas the accumulated rainfall amount in both regions is almost the same (seen from the integral of two curves). Second, the total number of rain events in both regions are roughly the same, as tabulated in Table 7.1. Third, both wind speed and seasonal air RH in Reno is consistently lower than those in LA.

The notable distinction of weather conditions in both regions leads to remarkably different moisture distributions through the slabs during a five-year simulation (Figure 7.3). The slab in Reno has a lower RH than the slab in LA. Notable differences embody not only the near-surface moisture (Figure 7.3c) but also deeper in the slab (Figure 7.3d

and e). They infer that the external weather information considerably influences the entire moisture profile of the slab.

However, since all the weather factors including rainfall pattern, wind speed, and air RH are different in both regions, the impact of each of these individual factors on pore moisture cannot be discerned. Therefore, an analysis to separate these factors is presented in the following.

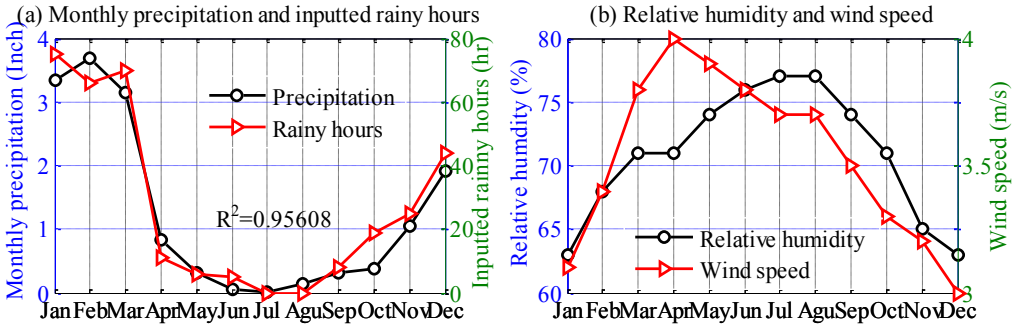

Figure 7.2 Rainfall distribution, air RH, and wind speed in Los Angeles (LA), California.

Table 7.1 Number and intensity of rainy events

Location	Number of rainy days (time)			
	I>0.254mm	I>1.27mm	I>12.7mm	I>25.4mm
Reno, NV	52	21	3	1
Los Angeles, CA	35	23	10	4

7.2.1.1 Impact of rainfall pattern

To assess the impact of the rainfall pattern on the slab-moisture distribution, the rainfall patterns of LA is entered into the simulation model with the other weather conditions of Reno. This modified "LA rainfall pattern" can then be compared to the model predictions for Reno by use of its own weather factors. The rainfall pattern does show some small influence on the near surface moisture distribution, but shows little impact on the deep-slab moisture (Figure 7.4). The near-surface RH difference is partially due to the contrasting rainfall distribution of the two regions. However, at a closer look, it is primarily due to the probabilistic factors of a local rain event resulting in a different rainy duration and intensity. That is, even if the same rain pattern is used, rain occurring during a specific hour in the previous year does not necessarily indicate that rain would happen during the same time in the next year. Despite these probabilistically-induced deviations, the statistical mean difference between the prediction is 0.005, demonstrating that the rainfall pattern does not appreciably affect the moisture profile of concrete slabs in the field.

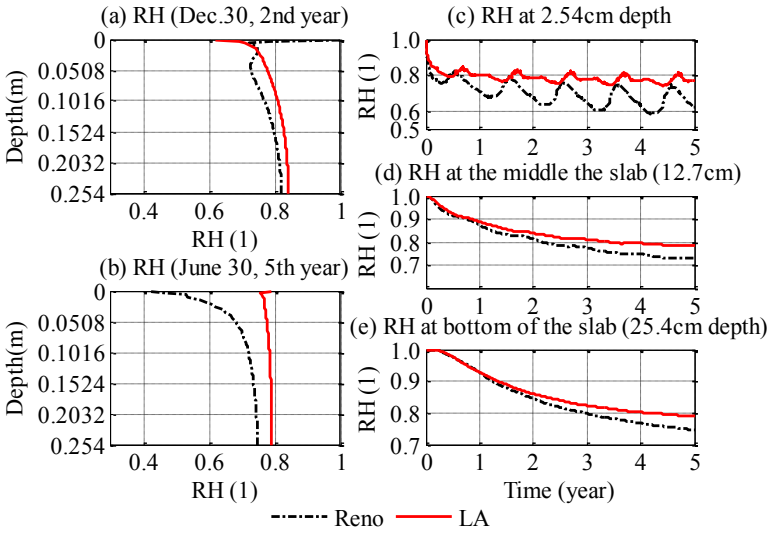

Figure 7.3 Predicted RH distributions in slabs in Reno and LA with time and depth.

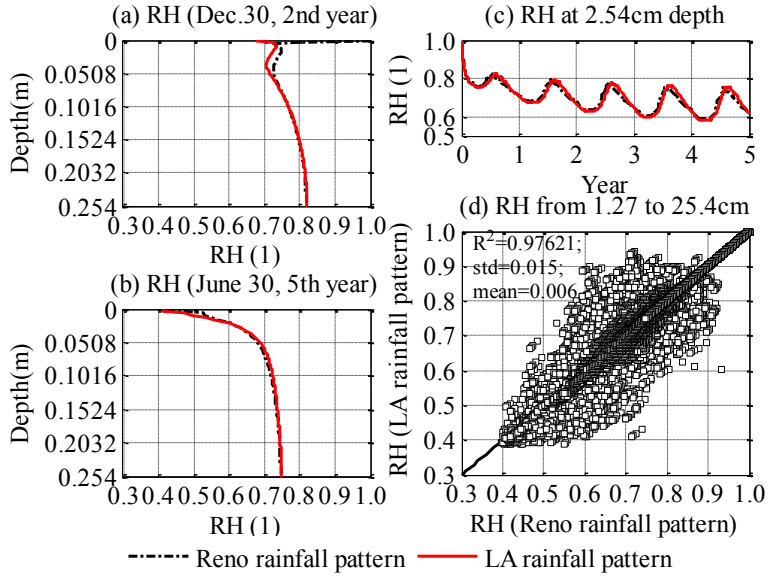

Figure 7.4 Impact of seasonal rainfall pattern on the moisture distribution within a slab.

7.2.1.2 Impact of wind speed

To assess the impact of wind speed on the predicted moisture distribution, a similar exercise is performed where the measured wind speed for LA is substituted for Reno wind speeds in the Reno climate. The prediction indictes that seasonal wind speed plays a negligible role on the moisture distribution of in-service pavement slab as illustrated in Figure 7.5. This is true even though the mean monthly wind velocity in LA is always 0.2-

1.0m/s greater than the wind speeds in Reno. Overlaps of the RH profile in Figure 7.5a (summer day) and Figure 7.5b (winter day) verify the neglegible role of the sesaonal wind pattern on an in-service slab's moisture distribution. Unlike the deviation of the predicted near-surface RH illustrated in Figure 7.4 when substituting rainfall patterns, two RH series at 2.54cm depth exhibit higher agreement when wind speed is exchanged in the model. Both the agreement and the statistical analysis demonstrate excellent agreement between the two swapped wind speeds (Figure 7.5d), further suggesting that the seasonal wind speed pattern plays a minimal effect on the moisture within a slab.

The negligible role of seasonal wind pattern on the slab-moisture profile may further imply that the daily variation of the wind speed works as a secondary role as well. To confirm this implication, a random number is specified to the daily wind speed according to a standard normal distribution. Use of this random number does not alter the monthly average wind speed, but vary the wind speed at any specific time.

Predicted results indicate that the daily wind speed notably influences near-surface RH in some cases, but does not affect the RH at greater depths. As illustrated in Figure 7.6a, predicted RH sparingly deviates from the line of equality when considering RH at all depths of the slab, inferring the impact of the daily wind speed variation. However, a truncated view of the RH from depths of 1.27cm to 25.4cm, as plotted in Figure 7.6b, yields regression coefficient of 1.0; standard deviation of the difference between hourly and daily RH variation of 0.001; and maximum deviation of RH from these two methods of 0.0016. This statistical agreement, together with the sparse deviation shown in Figure 7.6a, demonstrates that hourly wind speed does affect the near-surface moisture content, but does not influence the moisture budget at even small depths of a concrete slab.

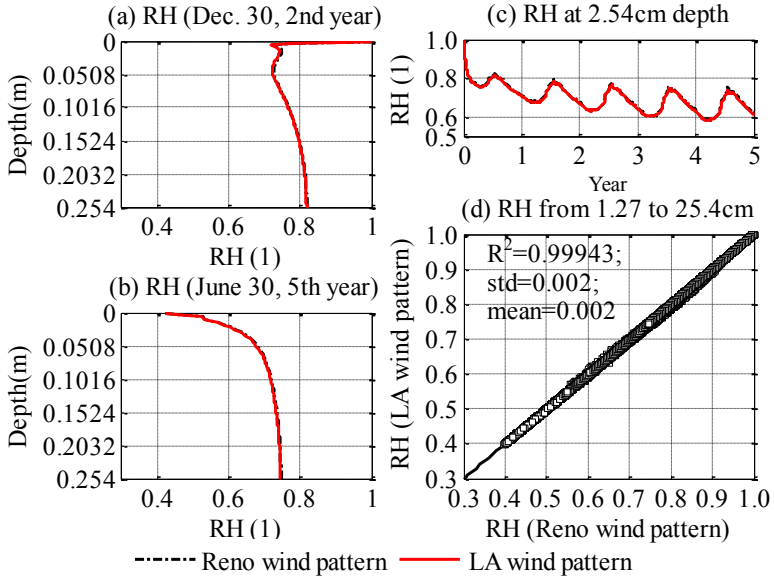

Figure 7.5 Impact of the seasonal wind speeds on the pore RH through in-service concrete slabs.

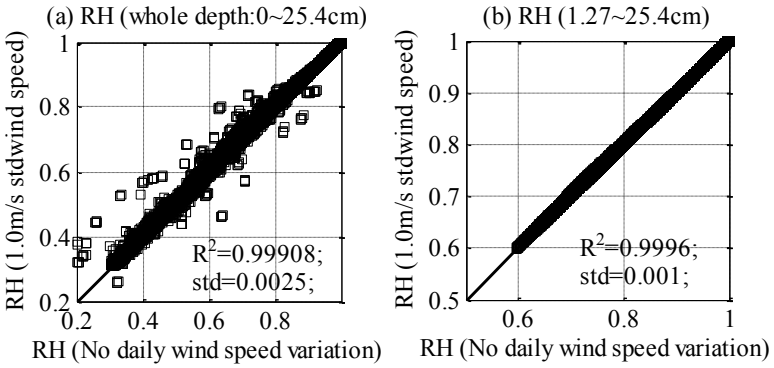

Figure 7.6 Impact of daily wind variation on the RH distribution within a slab.

7.2.1.3 Impact of the ambient air RH

Seasonal ambient air RH decisively controls the moisture distribution within in-service slabs (Figure 7.7). Data labeled with "LA RH pattern" are from the simulation that adopts all the weather parameters in Reno except the seasonal air RH, which is supplanted by the seasonal air RH pattern in LA. Comparison of the simulated results distinguishes the difference between the predicted RH of these two slabs. The plotted moisture profiles at both December 30, 2nd year and June 30, 5th year exhibit greatly differences, when compared with the data plotted at Figure 7.4 or Figure 7.5. These differences infer that the seasonal air RH primarily determine the moisture distribution within in-service slabs.

The determination also can be seen from the similarity between the seasonal near-surface RH and the seasonal air RH. A relatively larger difference between the RHs of the two simulations takes place around June, whereas a relatively less difference occurs around December (Figure 7.7c). Similarly, the differences between the seasonal air RHs of two regions also have a zenith around June and a nadir around December (Figure 7.1b and Figure 7.2b). Such coincidences further infer that the ambient seasonal air RH chiefly controls the moisture budget of in-service concrete slabs

Although the seasonal ambient RH plays a primary role on the RH within a slab, slab's moisture is not distinctly influenced by the daily variation of ambient air RH. In this study, a sinusoidal wave of amplitude 0.08 is utilized for daily air RH changes to approximate the monitored ambient RH provided by the weather station at the Reno airport. Adoptions of this amplitude in the predicted model result in a band-shape deviation along the line of equality, with a standard deviation of 0.041 and maximum deviation of 0.007 (Figure 7.8a). A truncated comparison (Figure 7.8b) focusing on only the RH values from 1.27 to 25.4cm depth exhibits a better agreement. Therefore, the daily variation of the air RH slightly affects only the very near-surface moisture distribution.

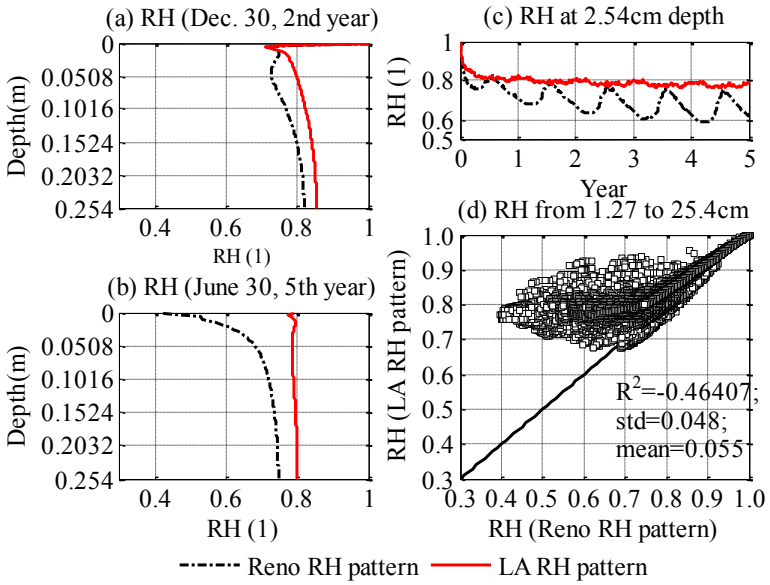

Figure 7.7 Impact of the seasonal air RH on the RH within in-service slabs

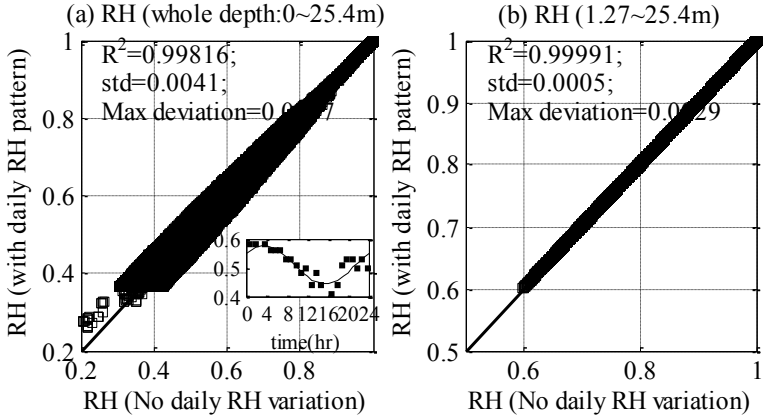

Figure 7.8 Impact of the daily air RH variation on the moisture distribution within slabs.

7.2.2 Effect of w/c ratio

While external factors such as wind speed and ambient RH have varying impacts on a slab-RH profile, controllable factors such as the w/c ratio can also potentially play a major factor. This study investigates the impact of concrete material properties on the internal RH distribution by use of concrete slab with three w/c ratios (0.30, 0.40, and 0.50). The saturated diffusivity of the concrete with a specific w/c ratio is computed on the basis of spline interpolating the diffusivity in Table 6.2.

Low w/c-ratio concrete has capacity to avoid a rapid moisture escape from the surface, but high w/c-ratio concrete does not. The difference between the RHs at specific depths of a slab is not proportional to the difference in the w/c ratio (Figure 7.8a and b). Lower

w/c ratio concrete slabs have greater pore RH and are less affected by the wetting and drying cycles at the slab surface. Unlike the impact of the local weather conditions, a variation of the water-to-cement ratio influences the deep-slab moisture greatly but affects the near-surface moisture unremarkably. This is primarily because the deep-slab RH is primarily controlled by the slab moisture budget but the near-surface moisture depends mainly on the boundary condition. As the used boundary is the same, so the near surface exhibits less difference. Concrete slab with a higher w/c ratio, however, has a greater diffusivity and thus results in the moisture deeper in the slab being easier depleted.

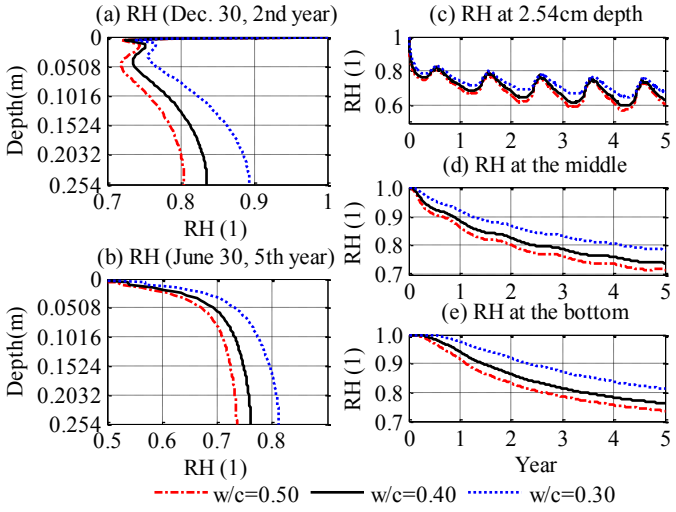

Figure 7.9 Impact of water-to-cement ratio on the moisture distribution within slabs.

7.2.3 Effect of the treatments of the upper boundary conditions

7.2.3.1 Wetting cycles

While ambient air RH is shown to have a pronounced effect on RH profiles in concrete slabs, wetting cycles must also be considered in the numerical model to understand the daily variation of the RH profile on a daily and even hourly basis. Figure 7.10 plots two data sets: one marked by "with wetting cycle" considers the wetting cycle whereas the other does not. Notable divergences of the plotted profiles (Figure 7.10a and b) confirm the remarkable impact of the wetting cycles on the moisture distribution of in-service slabs. More deviation appears at winter time (Figure 7.10c, X=0.5, 1.5, etc) because in Reno this time period signifies the rainier season of this location. This infers that the occurrence of wetting events appreciably impacts the moisture budget within a slab. This impact visualizes in the statistical analysis illustrated in Figure 7.10d. The analysis demonstrates that when the wetting cycles go unaccounted for, the underestimation of the RH of the whole step with a standard deviation of 0.028 (Figure 7.10d).

7.2.3.2 Use of Dirichlet and Neumann upper boundaries during drying cycles

From a numerical point of view, the specification of the upper boundary conditions may lead to different predicted results. The formulation of the upper boundary condition is either to fix the moisture value of the variable on the slab surface (Dirichlet type boundary condition, representing perfect moisture transfer) or to impose the moisture flux normal to the surface (Neumann boundary conditions). Currently, debate still centers on whether the upper boundary should be treated as a Dirichlet boundary or a Neumann boundary (Torrenti et al. 1999; IDIART 2009).

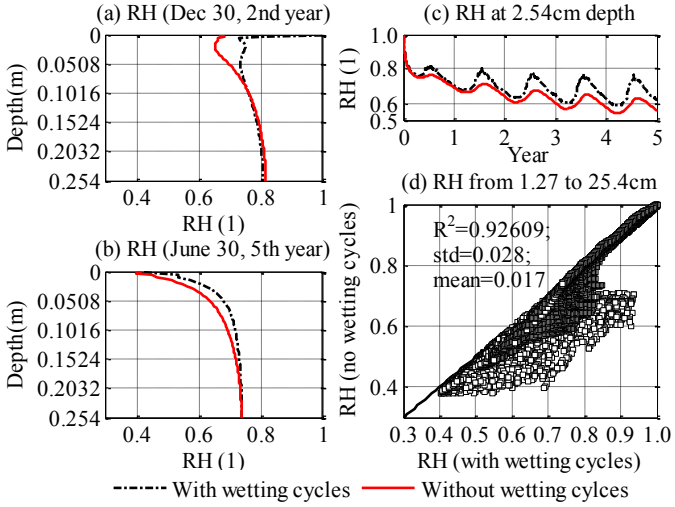

Figure 7.10 Effect of wetting cycles on moisture profiles in a concrete slab.

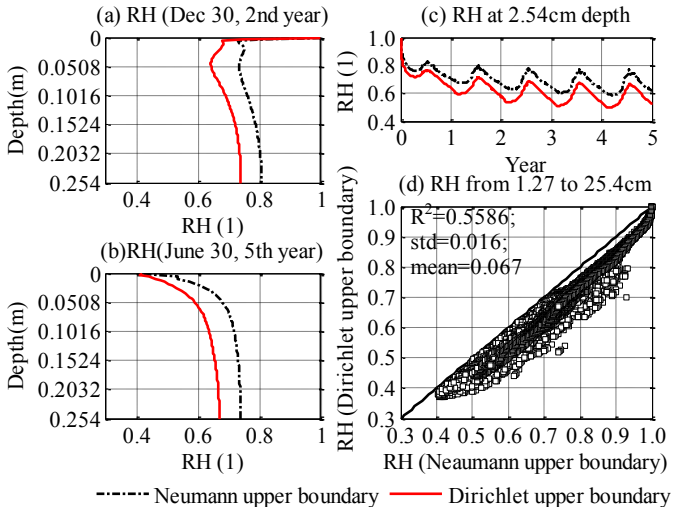

Figure 7.11 RHs within an in-service slab under different boundary conditions.

The RHs predicted from a model that uses a Neumann upper boundary are compared to that uses a Dirichlet upper boundary, in order to highlight the impact of the adopted boundary on the predicted results. A model adopting a Neumann upper boundary results in a higher more profile compared to the model using a Dirichlet upper boundary (Figure 7.11a and b). The RH series at depths of 1.27cm also exhibits discernable deviations when different upper boundary conditions are specified (Figure 7.11d). The statistic deviations of the entire-slab RH have a standard deviation of 0.021 and a mean deviation of 0.05 (Figure 7.11d). These considerable deviations confirm that the adoptions of the upper boundary condition in a numerical model that aims to predict in-service slab's RH greatly influences the predicted results.

7.3 Discussion

7.3.1 Why the roles of each weather pattern on the moisture of in-service slab are different?

The data from Figure 7.3 to Figure 7.11 reflect only the moisture distribution within in-service slabs in Reno and partially, in LA. In the followings, the discussion will not refer to any specific weather pattern and any specific region so that the discussion can be extended to the other regions.

7.3.1.1 Decisive role of seasonal air relative humidity

Seasonal ambient air RH is the determinative factor affecting the moisture budget of a slab. This determination can be analyzed from the convection formula shown in Eq.(6.12):

$$f = A(B + 2/3w_{rec})\left(RH_{top} - RH_a\right) \tag{6.12}$$

Details regarding the physical meanings of the parameters in the Eq.(6.12) can be referred to in Chapter 6. In this case, $A = 186.67$ and $B = 0.0537$.

After the curing terminates or a wetting event ends, the slab has a greater RH than the surrounding air. Moisture within the slab escapes from the surface to the air. However, this moisture outflow cannot maintain at a certain non-zero constant or wiggle around a positive constant; otherwise the moisture within the slab will be rapidly depleted to 0. That is, the moisture exchange will eventually move toward a state that moisture inflow roughly balances moisture outflow. At such a state, the wetting processes lead to moisture gain and the drying events result in moisture loss. The data plotted from Figure 7.3 to Figure 7.11 indicates that the time from the end of the curing to such a stable state lasts a period of 5 or more than 5 years.

This long period means that after a wetting event terminates, the moisture outflow must follow an exponential decline and then become negligible; otherwise, the stable state will quickly achieve. Usually the interval of the exponential decline lasts 3-5 hours (Al-Fadhala and Hover 2001; Hover 2006). Therefore, at most of the time the state of $f \cong 0$ holds in Eq.(6.12) because accumulative time of these intervals and of wetting events are orders of magnitude less than accumulative drying time. That is, at most of the time the RH_{top} must wiggle around the RH_a because the condition of $f \cong 0$ is satisfied

only when $RH_{top} - RH_a \cong 0$. Therefore, the seasonal air RH mainly dominates the pore RH at the top of the slab.

As the moisture diffusion within a slab is a boundary-value problem, this domination infers that RH_a dominates the resulting RH profile. This is because the drying period is typically one-order of magnitude greater than wetting period. Therefore, seasonal ambient air RH dictates the moisture distribution within in-service concrete slabs regardless of the regions.

7.3.1.2 Role of wind speed

Seasonal wind speed acts a secondary role on the slab-moisture distribution, but this mechanism needs to be examined during wetting and drying time in order to clarify its impact in other regions. During the wetting time, slab surface is wet and $RH_{top} = 1$ such that the role of wind speed is eliminated. During the drying cycle, the condition is relatively complicated. Here, this drying period can be divided into two scales: transition time ($f > 0$) and total-drying time ($f \cong 0$). During this transition time, variation in wind speed alters the moisture outflow f. However, an increase of wind speed only shortens the length of the transition time, and vice versa. For instance, windy weather after a rain event accelerates the moisture loss from a slab surface, making the surface drying faster; but it cannot vary the total amount of the evaporation required because this amount is determined by the free vapor content at the slab surface. During the total-drying time, $f \cong 0$ diminishes the role of wind speed on the slab-surface moisture exchange.

The analysis regarding the transition time infers that daily wind variation affects the near-surface RH. In Eq.(6.12), a great variation of wind speed w_{rec} for instance from 2 to 15m/s (a gust) can appreciably change the value of f by one order of magnitude. During the transition time, the term of $RH_{top} - RH_a$ is greater than that during the drying time, thereby magnifying the role of daily wind variation on moisture convection at the slab surface.

7.3.1.3 Influences of wetting cycles and rainfall pattern

It seems a self-contradiction that the occurrence of wetting cycles influences the moisture distribution within a slab, but the rainfall pattern does not affect the slab's moisture budget. To clearly explain this mechanism, it merits noting that the wetting cycle characterizes whether the slab surface is wet or dry whereas the rainfall pattern depicts the rainfall distribution in a specific region.

Nonlinearity of the concrete's diffusivity (Figure 6.1) results in the slab's RH being easily influenced by the wetting cycles, although the measure of the wetting time is one-order magnitude lower than that of the drying time. During the wetting cycles, absorption and permeability dominate the moisture intake. Capillary force makes the concrete surface rapidly absorb free water at the surface. The moisture transport during these wetting cycles is significantly higher than the water vapor migration during the subsequent drying cycle. During the drying cycles, the concrete surface rapidly becomes dry whereas the concrete below the surface is still wet. Drying of the surface lowers the

near-surface diffusivity, thereby blocking the rapid evaporation of the moisture absorbed during the wetting time. In other words, concrete easily absorbs moisture when wetting but does not lose it when drying as easily. This phenomenon of the diffusivity leads to the wetting cycles greatly affecting the magnitude of the moisture budget within an in-service slab, even if the wetting cycles accounts only for a small probability of occurrence (e.g., approximately 180/8760 in Reno),

Moisture budgets of in-service slabs are unremarkably influenced by the local rainfall pattern because the slab surface has adequate time to absorb the moisture at each wetting event. Usually, the transition time requiring for $f \cong 0$ is 3-5hr (Al-Fadhala and Hover 2001; Hover 2006), shorter than time between two adjoining rainy events. This is always the case. According to our common knowledge, normally the ground becomes drying rapidly after a specific rainy event, and the subsequent rain comes following a relatively longer period. This normal phenomenon possibly fails to hold owning to the probabilistic characteristic of rainy event in some abnormal cases; e.g., the occurrence of two adjacent rains is too close, such as 2hr. These cases, however, are small probability events. In this regard, concrete surface has sufficient time to absorb the moisture during each individual rainy event. Therefore, once the total rain events are known, the effect of wetting cycles on the slab-moisture intake is determined regardless of the seasonal rainy-events distribution. Therefore, the rainfall pattern, seasonal rainy-events distribution, acts only a secondary role on the moisture budget of an in-service slab.

7.3.1.4 Effect of w/c ratio

As the concrete's moisture diffusivity controls the moisture transport within the slab, the w/c ratio affects the entire moisture profile of the slab. During casting, the internal RH is initially 1.0 due to free and bleed water appearing in the slab. However, the monthly ambient air RH is definitely less than 1. This difference results in a negative moisture budget after casting the slab. Concrete with higher w/c ratio has a greater diffusivity and becomes easier prone to loss its internal moisture.

7.3.1.5 Why the treatments of the surface boundary influences the predicted results remarkably?

A specification of the Dirichlet upper boundary uses a lower boundary value, leading to an underestimation of the RH within in-service slabs. It is noteworthy that a sole analysis to the plotted data in Figure 7.11 is inadequate to confirm this underestimation. Analysis to this underestimation needs refer to the model verification in Chapter 6 (Figure 6.7), which uses a Neumann upper boundary and results in visual, statistical agreement between the predict results and the observed values. Therefore, the verification will result in the predicted results being lower than the observed data if the verification uses a Dirichlet upper boundary. This is because the predicted RHs from a model with a Dirichlet upper boundary are always less than those from a model with a Neumann upper boundary (Figure 7.11).

This underestimation is due to two reasons. First, the use of Dirichlet upper boundary neglects the transition time as RH_{top} approachesRH_a. During the drying cycle, the RH_{top} is slightly greater than RH_a ($RH_{top} - RH_a \cong 0\ but > 0$). Therefore, the wetting cycles still influence the near-surface moisture intake for a relatively long period after the wetting commences. Secondly, the use of Dirichlet upper boundary also ignores the moisture boundary layer existing at the slab surface; the difference between the RH_a and RH_{top} exists in this layer. This ignorance is equal to assuming that the wind velocity at the ground surface is infinite and that thickness of the boundary layer vanishes. In fact, the existence of this layer makes the slab relatively less sensitive to the daily fluctuation of the ambient air RH. In addition, existence of this layer results in the RH_{top} being generally slightly greater than the RH_a so that the negative moisture budget lasts 5year or more (Figure 7.3-Figure 7.11). Therefore, adoption of Dirichlet upper boundary uses a lower-boundary value and thus consistently under-predicts the RH profile within a slab.

7.3.2 What do the sensitivity studies imply?

These sensitivity studies and their working mechanisms have implications on the construction season selection and optimum w/c ratio design.

7.3.2.1 Construction designs

Construction of a pavement slab during a season with a low probability of precipitation is not necessarily ideal. As shown in Figure 7.10b, a slab in Reno has a lower RH within the slab when sheltered from rain. A relatively steep moisture gradient is then formed through the slab and would result in greater differential drying shrinkage strain. Alternatively, concrete material design that promotes more reversible shrinkage and higher creep may help alleviate some of these moisture-induced shrinkage stresses.

Selection of proper construction seasons can also elongate the longevity of a concrete pavement slab. For example, in Reno, the ambient air RH is lowest during the summer. Due to the determinative role of the ambient air RH, construction of concrete pavement slabs during these seasons can lead to the rapid evaporation of bleed water at the pavement surface (Jeong and Zollinger 2003). In this case, adequate curing would be critical to avoid the over-development of undesirable drying shrinkage during early ages, and to prevent the rapid moisture loss occurring at the surface. In addition to needing adequate curing during the early ages of the concrete, a pavement slab in arid climates may require greater thickness or shorter joint spacing than in wetter regions to resist this differential drying shrinkage.

7.3.2.2 Optimum w/c ratio design

Designs using a low diffusivity concrete in marine region may be crucial to insulate the ingression of chloride ions to the concrete. This type of concrete reduces the ion's penetration depth during the wetting cycle and declines the moisture exchange between the concrete and the external environment.

Design of a moderate w/c concrete in mountainous desert regions is decisive to help ensure the long-term performance of a slab. On one hand, a high w/c ratio concrete tends to make the concrete prone to the variation of the environment factors such as wetting and drying cycles. It also facilitates the moisture loss from the concrete and induces a great amount of undesirable shrinkage during the service of the slab. On the other hand, a lower w/c ratio concrete probably increases the self-desiccation or autogenous shrinkage of the slab. Both of them increase the uniformly distributed shrinkage-induced stress within the slab and widen the pavement's cracking or joints space.

7.4 Conclusions

Moisture distribution within in-service slabs is affected by both external and internal, controllable factors. Predictions of these RH profiles are also affected by modeling parameters such as the treatment of the upper boundary condition. Proper characterization and understanding of these factors have distinct implications on the performance of concrete pavement slabs.

1) Seasonal ambient air relative humidity (RH) plays a dominant role on the moisture distribution within an in-service slab. The seasonal rainfall pattern, monthly wind speed, and variation of daily RH influence the slab's internal RH profile in a secondary role. To offset the moisture gradients in arid climates, increasing thickness or reducing joint spacing may need to be applied in comparison with wetter regions.

2) Daily variation of the local wind speed notably affects the near-surface RH because this helps accelerate the escape of water immediately after a wetting event ends.

3) Use of a Dirichlet upper boundary greatly underestimates the moisture profiles within a slab. This is because this boundary assumes that the pavement surface dry immediately after a wetting event ends. After a wetting cycle, there exists a transition time during which the moisture escape from the pavement surface exponentially declines to zero. Conversely, use of a Neumann convective boundary is more appropriate to model moisture movement during drying cycles.

4) Concrete easily absorbs moisture when wetting, but typically loses water much slower due to the non-linearity of slab's moisture diffusivity. Therefore, although the probability of precipitation is typically one order of magnitude less than drying in many locations, magnitude of the wetting events still control the moisture budget of in-service slabs to a large degree.

Chapter 8 Total environmental loadings developed through in-service slabs

Environmental loadings that in-service pavement slabs suffer from include not only thermally-induced stresses (curling stress) but also moisture-induced stress (warping stresses). Different from the curling stress, the warping stress exhibits a less-regular swing of amplitude. These changes in warping stresses depend mainly on the slab moisture diffusion and slab mechanical parameters, e.g., creep compliance. The dependency on the moisture diffusion suggests that the warping stress potentially remains in a higher stress state immediately after the curing ends. This is because during this period, the moisture loss from the slab surface is significantly greater than the other period. The dependency on the mechanical parameters suggests that this greater stress state may relax progressively since concrete slab have a viscosity properties. An investigation to the evolution of the total environmental loadings developed through in-service slabs potentially serves as the basis for a credible estimate the performance of in-service concrete pavement slabs.

Moisture-induced stresses within concrete specimens have been investigated in laboratory conditions, for which both moisture distribution and temperature distribution within the specimen are controllable. Series studies of Bazant's group have been dedicated to the shrinkage-induced stress through lab specimens (Bazant and Raftshol 1982; Bazant and Chern 1985; Bazant 1998; 2000). These studies consider both the basic creep behavior and Pickett effect of concrete slab. The stress-strain response of the varying moisture distribution within the slab can be regarded as both elastic and viscous behavior, which for concrete, can be characterized by use of a simple Maxwell model (Bazant and Asghari 1974; Bazant and Tsubaki 1980; Bazant and Chern 1985). Nevertheless, these studies do not center on the environmental loadings developed through in-service concrete pavement slabs. The stress-strain response of these slabs is relatively complicated because they experience both moisture variation and temperature variation. The total environmental loadings developed through an in-service slab may exhibit a totally different scenario from the thermally-induced stress when the component of the moisture-induced stress is added to the total environmental stress. In extreme cases, this total environmental stress may be higher than the bending tensile stress of a slab.

This chapter estimates the total environmental loadings developed through in-service slabs. These concrete slabs are regarded as a viscoelastic material, which is characterized by use of a Maxwell model. The viscoelasticity of the concrete includes the basic creep and drying-induced creep components. The total stresses and the thermal stress are analyzed to highlight their differences. The study focuses on the stress developed immediately after the curing ends and on relaxation history of the total stress. It also concentrates on the influences of the construction season, pavement location, mechanical parameters (Young modulus, Poisson ratio, etc.), local weather conditions, and the concrete mix properties on the total stress developed through a jointed plain concrete pavement slab.

8.1 Computational theory to warping and curling stresses

8.1.1 Creep and relaxation

The elastic method used to compute the curling stress overlooks the stress relaxation and creep behavior of concrete. In the short-term, this assumption may not lead to a significant reduction of the curling stresses but possibly reduces these stresses during a long period. Therefore, this time-dependent behavior should be considered during the computation of the total environmental loadings that in-service pavement slabs suffer.

An alternative is to regard the slab as a viscoelastic material. Viscosity of a concrete slab can be described by several viscoelastic models including the Maxwell chain model (Figure 8.1a), Kelvin chain model (Figure 8.1b), or the combination of these model like the standard linear solid model (Figure 8.1c). Although the standard linear solid model is more accurate than the Maxwell and Kelvin-Voigt models in predicting material time-dependent stress responses, it mathematically more difficult to assess than the other two models. The developed stress cannot be seen as a constant as thermal stresses vary rapidly as shown in Chapter 4. Thus, in-situ pavement slabs experience more stress relaxation than creep. Therefore, the Maxwell model, capable to more accurately predict the relaxation phenomenon, is suitable to estimate the stress behavior of the in-service pavement. One added benefit of a simple Maxwell model is the ability to estimate the time-dependent stress behavior through a single variable, the viscosity of the concrete.

For hardened concrete, relaxation of concrete can be computed from the following equation modeling the Maxwell chain (Figure 8.1a):

$$\frac{\dot{\sigma}}{E} + \frac{\sigma}{\eta} = \dot{\varepsilon_T} \tag{8.1}$$

where η is the viscocity of the concrete $(Pa \cdot h)$, $\dot{\sigma}$ is the time derivate of the thermal stress (referred hereinafter that any variable with a dot above stands for the time derivate of the variable).

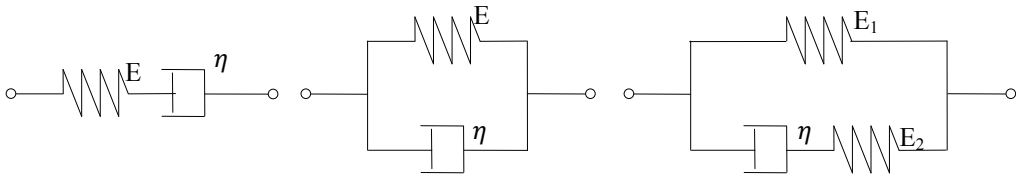

a) Maxwell model b) Kelvin-Voigt model c) Standard linear solid model

Figure 8.1 Schematic representations of different viscoelastic models.

8.1.2 Warping stresses

Shrinkage contributes a great portion of the concrete deformation, especially for an early-age concrete slab. The shrinkage of a slab depends on the time elapsed and on the internal RH distribution of pores within a concrete slab. This shrinkage can be computed by the following equation according to the B3 model (Bazant 2000):

$$\epsilon_{sh}(t_d, t_0) = -\epsilon_{sh\infty} k_h S(t_d) \tag{8.2}$$

where $\epsilon_{sh\infty}$ $(\mu\varepsilon)$ is the total or ultimate shrinkage; t_0(day) is the time the slab begins service, usually $t_0 = 3 - 7$ days (Bazant 2000); t_d is the day at which the shrinkage stress is concerned; k_h represents the term of the reversible shrinkage; and $S(t_d)$ represents the irreversible shrinkage. They can be computed by the following equations (Bazant 2000):

$$k_h = \begin{cases} 1 - RH^3 & RH \le 0.98 \\ 0.2 & RH = 1 \\ RH & RH \in (0.98, 1) \end{cases} \tag{8.3}$$

$$S(t_d) = tanh \sqrt{\frac{t - t_0}{\tau_{sh}}} \tag{8.4}$$

where τ_{sh} (day) stands for size dependence and usually $\tau_{sh} = 600$ days is used (Bazant 2000).

Another parameter needed in Equation (8.2) is the ultimate shrinkage $\epsilon_{\square h\infty}$ $(\mu\varepsilon)$. According to Mindess et al (2002), it ranges from 415 to 1070 $\mu\varepsilon$ for normal Portland concrete and $\epsilon_{sh\infty} = 780$ $\mu\varepsilon$ is recommended if a measured value not available.

Creep behavior has to be considered when warping stresses of a pavement slab are computed. Unlike the curling stresses, the warping stresses have longer periods which are usually 10-90 days in length. This longer period allows the shrinkage-induced stress to relax to some degree depending on the viscosity of the concrete material in the slab at that time. Considering the viscosity of concrete, the stress-strain correlation due to shrinkage can be characterized by Eq. (8.1), in which, for this case, the $\dot{\varepsilon_T}$ is replaced by the $\dot{\epsilon_{sh}}$.

8.1.3 Drying creep (Pickett effect)

The deformation of a concrete specimen under sustained loads exceeds the summation of a load-free specimen's drying shrinkage and of the deformation of a specimen that does not dry. This phenomenon was first observed by Pickett (Pickett 1942). Its mechanism has been thoroughly studied by Bazant et al (Bazant and Chern 1985; 1998).

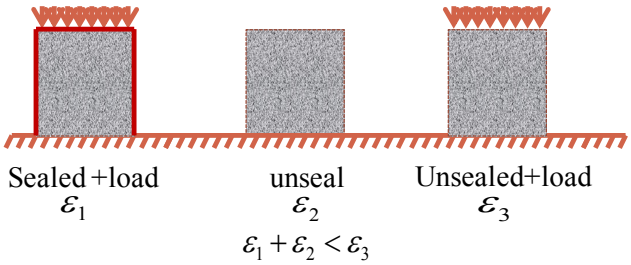

Figure 8.2 Pickett effect (drying-induced shrinkage.

Considering this phenomenon, the computation of the environmental loading-induced stresses through an in-service pavement slab has to be modified as (Bazant and Chern 1985):

$$\frac{\dot{\sigma}}{E} + \frac{\sigma}{\eta} = \dot{\varepsilon} - \dot{\varepsilon_{sh}} - \dot{\varepsilon_{temp}} \tag{8.5}$$

where $\dot{\varepsilon_{sh}}$ and $\dot{\varepsilon_{temp}}$ stand for the relaxation rates that are induced by $\dot{RH}$ and $\dot{T}$, respectively. They can be estimated by Eq. (8.6) and Eq. (8.7):

$$\dot{\varepsilon_{sh}} = \epsilon_{sh\infty}\varphi(1 - r\sigma)\dot{RH} \tag{8.6}$$

$$\dot{\varepsilon_{temp}} = \overline{\alpha}(1 - \rho\sigma)\dot{T} \tag{8.7}$$

where for hardened concrete $\varphi = d(1 - RH^3)/dt$; r and ρ ranges from $0.1/f_t$ to $0.3/f_t$, in which $f_t(MPa)$ is the bending tensile stress of concrete; $\overline{\alpha}$ is an empirical constant and usually $\overline{\alpha} = 0.063\mu\varepsilon$ is used (Bazant and Chern 1985). It should be noted that when both the combination of warping and curling stresses are computed, $\dot{\varepsilon} = \dot{\epsilon_{sh}} + \dot{\varepsilon_T}$ is used in Eq. (8.5).

The stress development through the slab is still based on the Mohamed and Hansen method (1997), which has been proposed from Eq. (4.1) to (4.10). That is, one can obtain the total stress developed through a slab by use of algorithm from Eq. (4.1) - (4.10) to compute the redistribution of the free strain at Eq.(8.5). It should be noted that the method used to calculate the free stress is viscoelastic-based but the method used to compute the real stresses (the re-distribution of the free stress) is elastic-based. The stress redistribution can be computed from the elastic theory because the redistribution occurs simultaneously with the development of free stresses.

8.2 Simulation details

This study computes the total stress in Eq. (8.5) using the explicit central difference method, a method can be referred to any normal numerical analysis textbook (Burden and Faires 2000). This method is also used to evaluate rates of moisture- and temperature-variations in Eq. (8.6). The viscosity of concrete is a time-dependent function, ranging from $0.7*10^6$ to $1.4*10^6$ $MPa \cdot h$ as demonstrated in Figure 8.3 (Bazant 2000).

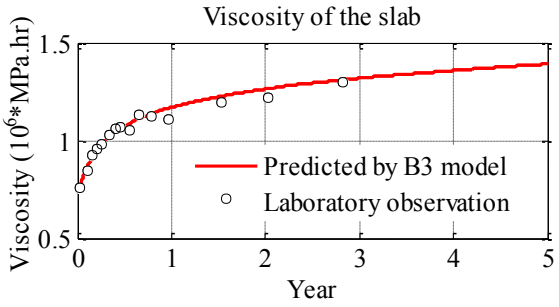

Figure 8.3 Evolution of the viscosity of a slab. Note: Laboratory observed data is reproduced from Bazant (Bazant 2000).

The curing of the concrete is concluded after 3 days the slab casting, i.e. $t_0 = 3$. The simulation assumes the slab is cast at 3 day before April 1, July, 1, and October 1, respectively, in order to analyze the influence of the construction season on the developed stress. It uses the thermal stress at 12:00AM as the initial stresses. The concrete is assumed having a water-to-cement ratio of 0.45. The bending tensile strength of concrete is assumed as 4.6MPa; i.e. $f_t = 4.6$. This simulation estimates the total stress evolutions during 5 years after the curing commences. Numerical code for this simulation can be referred to Appendix E.

8.3 Results

8.3.1 Stress evolution immediately after the curing

After the curing commences, the top of the concrete slab almost suffers from tensile stress even if the slab curing terminates at the hottest season (Figure 8.4). In such weather, during the daytime, the slab surface is hot and results in positive temperature gradient across the slab. Compressive stress develops at the top if the through-depth slab RH is uniform. However, this positive temperature gradient is overwhelmed by the ongoing shrinkage, which induces tensile stresses. Therefore, after the curing ends, the top of the slab suffers from tensile stress all day round.

This increase of tensile stress near the top results in the increase of compressive stresses developed the bottom; however, the bottom experiences relatively less stress than the top of the slab. The total stress at the slab's bottom cycles between approximately -

1.5 to 1.5 MPa for the slab in Reno and between -1.0 and 1.0 for the slab in Los Angeles (Figure 8.4). One reason for the stress amplitude differences between the slabs of these two regions is that the temperature variation in Reno is relatively greater and leads to more thermal stress developed within the slab. The other reason is that Reno has a comparatively lower ambient relative humidity and results in the slab undergoing more rapid moisture loss and subsequent drying shrinkage.

The concrete slab in Reno experiences stress relaxation over daily cycles whereas that in Los Angeles does not. In both regions, the tensile stresses at the slab top immediately increase after the curing terminates. This is because the rapid moisture escape from the slab surface leads to a sharp negative RH gradient near the top. For the slab in Reno, the wiggle of daily-maximum tensile stress at the top in some time exhibits a plateau (Figure 8.4a). This infers that the developed stress is greater than the bending tensile stress; thus the top of the slab experience stress softening. In Los Angeles, stress softening does not occur at the top, even though the total stress is greatly higher than the thermal stresses.

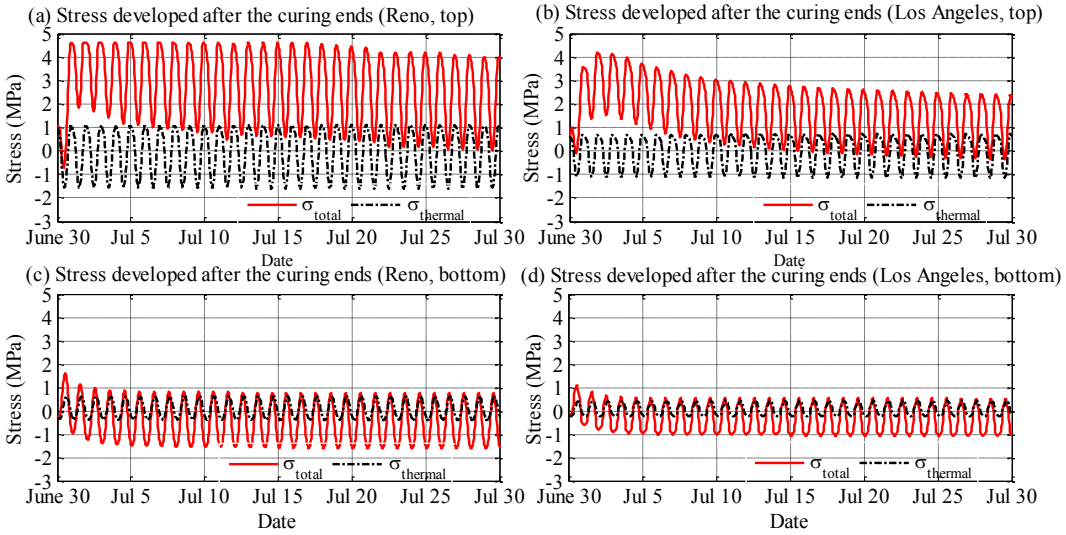

Figure 8.4 Stress developments at the top and bottom of the slab for one month after the curing ends. Note: tension is positive.

8.3.2 Long-term stress developments

The stress plotted in **Figure 8.4** exhibits reduction of both tensile stress at the top and compressive stress at the top. These reductions suggest that the stress developed through the slab can possibly relax progressively. To show this stress relaxation, Figure 8.5 plots the daily maximum tensile stress at the top and the daily maximum compressive stress at the bottom over a five-year period following concrete casting and curing.

The developed stresses exponentially decline after the curing ends. They become stable approximately 3-6 months after the casting of the slab. The exponential decrease of the developed stress is conspicuous for the stress near the slab surface. The developed

tensile stress drops to a nadir after approximately 6 months duration. After this period, the shrinkage-induced stresses become stable since the subsequent nadirs and zeniths appear roughly at the same time and in same magnitude (Figure 8.5).

The duration required for this stabilized time is not significantly affected by the weather conditions. Reno has both lower ambient relative humidity and fewe rain events, but experiences higher wind speed than Los Angeles. These aggressive weather conditions make the concrete slab in Reno experience a quicker moisture loss after the curing ends. However, in both regions, the time required for the total stresses to become cyclically stable coincides well (Figure 8.5). The reason behind this phenomenon is that only a notable moisture-varying rate can lead to warping stress. However, an inconspicuous rate does not result in distinguishable stress difference as both the Pickett effect and relaxation behavior of the slab can immediately relax the stresses induced by this slight moisture varying rate. This means that the shrinkage-induced stress progressively loses its domination. Therefore, after several months the stresses induced by the moisture variations are minimal because the stress relaxation dissipates these stresses.

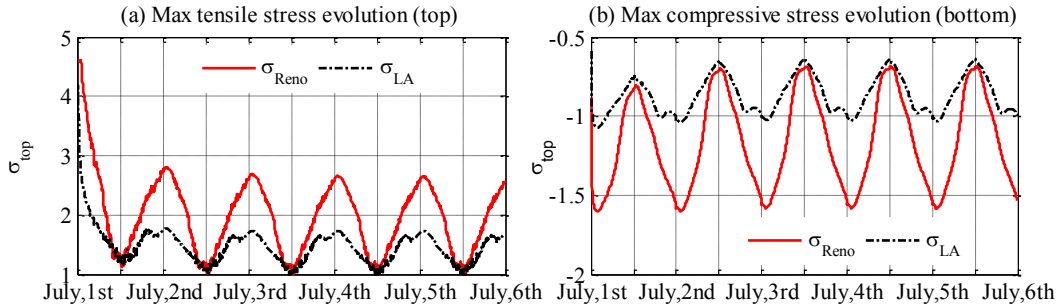

Figure 8.5 Stress relaxation during 5 years after the curing ends.

8.3.3 Does the stress at the stable state converge to the thermal stress?

The stress at the cyclically-stable state diverts from the thermal stress. This is because the slab pore RH strongly relies on the temperature variation. Daily variations of the temperature result in the swing of the internal concrete pores' RH and thus in the swing of total stress. To illustrate this issue, the total-stress profile and thermal-stress profile are plotted (Figure 8.6) and the daily total-stress contour and thermal stress contour on June 30, 5th year are depicted (Figure 8.7).

At the stable state, the stress during daytime coincides with the thermal stress whereas the stress during the nighttime does not. During daytime (top is compressive stress), the temperature at the top is greater than the room temperature (usually 22^{o}C). The RH near the top thus slightly increases such that the total compressive stress at the top should be slightly greater than the thermal stress. But at the cyclically-stable state, the estimated total stress coincides with the thermal stress and, in some cases, slightly higher than the thermal stress (Figure 8.6). This is because the creep effect and Pickett effect make the

elastically-developed stress relax to some degree. During the night time (top is tensile stress), the top of the slab is at a lower temperature and the bottom of the slab remains relative hot. This different thermal condition results in contraction occurring at the top and develops tensile stress therein. The estimated total tensile stresses are remarkably greater than the computed thermal stresses (Figure 8.6).

At the cyclically-stable state during the summer months, the top of the slab suffers from a total tensile stress greater than the thermal stress owning to two reasons. First, both terms of $1-\rho\sigma$ and $1-r\sigma$ in Eq.(8.6) are less than 1 when the local slab is in tension; but these terms are greater than 1 when in compression. This difference results in a greater portion of the developed compressive stress being relaxed during the day hours (compressive at the top) than the night hours. Secondly, during the night time, the RH declines within the slab as the temperature drops (Eq. (6.16)). The decline of the pore RH through the slab magnifies the term of $1-h^3$ in Eq. (8.6). It thus increases the reversible component of the shrinkage during this time and enlarges the developed tensile stress near the top of the slab. These two reasons result in the developed stress relaxing to a lesser magnitude during the night hours, and results in the estimated total stress diverging from the thermal stress during the nighttime.

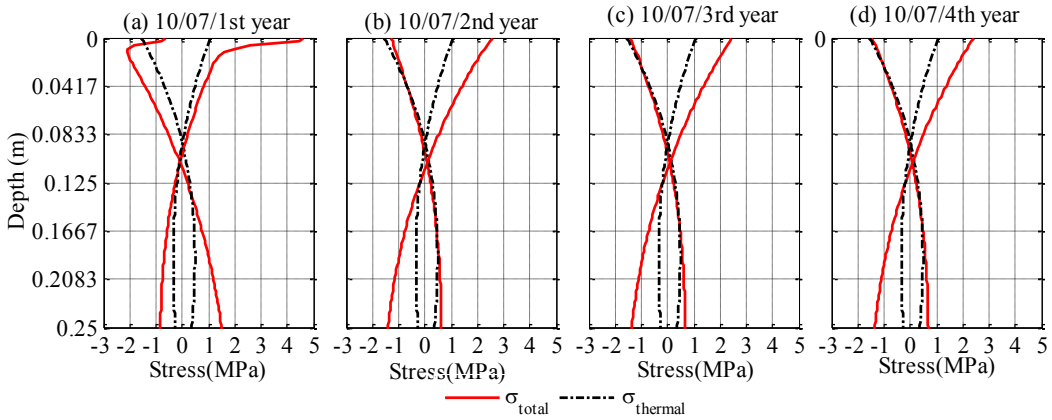

Figure 8.6 slab-stress profiles at the cyclically-stable time suggest that the total stresses divert from the thermal stress; maximum tensile stress at the bottom appears 13:00PM, maximum compressive stress the top at night time (In Reno).

8.3.4 Impact of construction season on the developed stresses

Stress relaxation depends on the RH, stress, slab's viscocity, etc. This dependency suggests that construction season may greatly influence the stress developed within a slab. To illustrate this influence, this study assumes that pavement slabs in Reno and Los Angeles are cast and commencing curing on at March 30, June 30, and September 30, respectively.

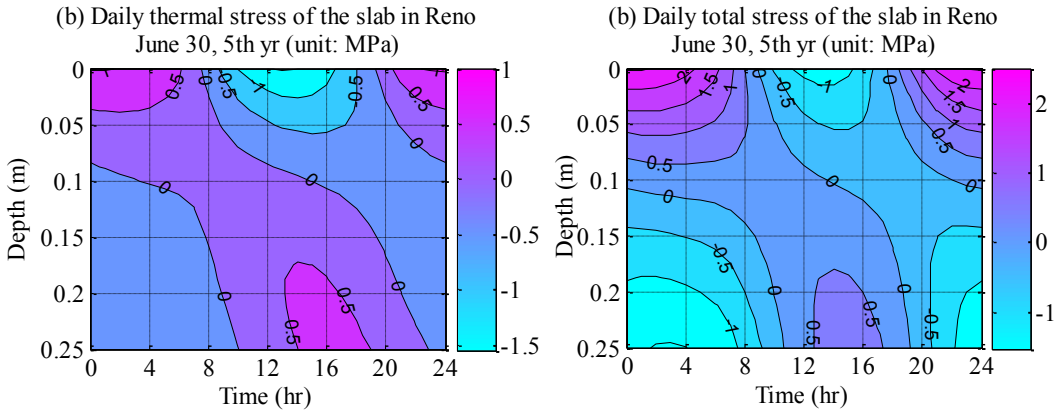

Figure 8.7 Thermal stress versus total stress on June 30, 5th year (In Reno).

The developed total stresses after the curing ends are greatly affected by the construction seasons (Figure 8.8). In Reno, the slab built in June experiences largest stress whereas slabs paved in September potentially suffer from the lowest total stresses (Figure 8.8a). In Reno, the ambient RH from September to December is relatively higher. Another reason for this phenomenon is that the autumn season in Reno is less-windy than April and July (Figure 7.1b). Therefore, the slab built in September experiences a lower rate of moisture escaping from the surface. It thereby suffers from less moisture-induced stresses developing within the slab when compared to the slab paved in October. However, this does not necessarily mean that any slab built in October will be subject to less environmental loadings over the course of its service life. For instance, in Los Angeles, a slab paved in March tends to suffer from greatest stress but that one paved in June experiences a relatively lower stress, especially immediately after the curing ends (Figure 8.8b). This is because in Los Angeles the ambient RH in June is at its zenith, resulting in a lower rate of moisture escaping from the surface and thus in a less tensile stress at the top. Therefore, it is critically important to note the site-specific ambient RH patterns to construct concrete pavement slabs that undergo lower total stress development, thereby promoting long-term pavement performance with respect to fatigue cracking development.

8.3.5 Environmental loadings of concrete slabs in different regions

8.3.5.1 Stress developed in coastal and arid regions

The concrete slabs in the region within less air RH tend to experience higher stress. Figure 8.9 plots the daily maximum-tensile stress developed through slabs in Reno, Nevada; Las Vegas, Nevada; Los Angeles, California; Astonia, Oregon. The former two regions attribute to lower ambient RH, arid regions. Concrete pavements in these arid regions tends to experience more stress across the slab. The latter two regions are coastal locations with a higher ambient RH. The slabs built in these regions undergo less stress;

the softening of stress does not occur at the top under the assumed geometry and construction date.

An interesting result is that the slab in Las Vegas suffers from less total stress development compared to the slab in Reno, Nevada (Figure 8.10a). Since Las Vegas has lower seasonal ambient RH, this is contradicting to the conclusion that the slabs in regions with lower ambient RH experience higher total stresses. This phenomenon occurs for distinct three reasons.

First, moisture escaping from the slab in Reno occurs more rapidly than in Las Vegas. In Las Vegas, the ambient RH is lower than that in Reno (Figure 8.10b). Thus, the RH near the top of slab dramatically drops because the ambient RH directly controls the RH near the surface. The drop of slab-surface RH reduces the near-surface diffusivity and thus blocks rapid moisture escape from the surface. This is because the slab moisture diffusivity highly decreases at lower pore RH (Figure 6.1). Thus, after the curing ends, the slab in Las Vegas tends to suffer from less shrinkage stress.

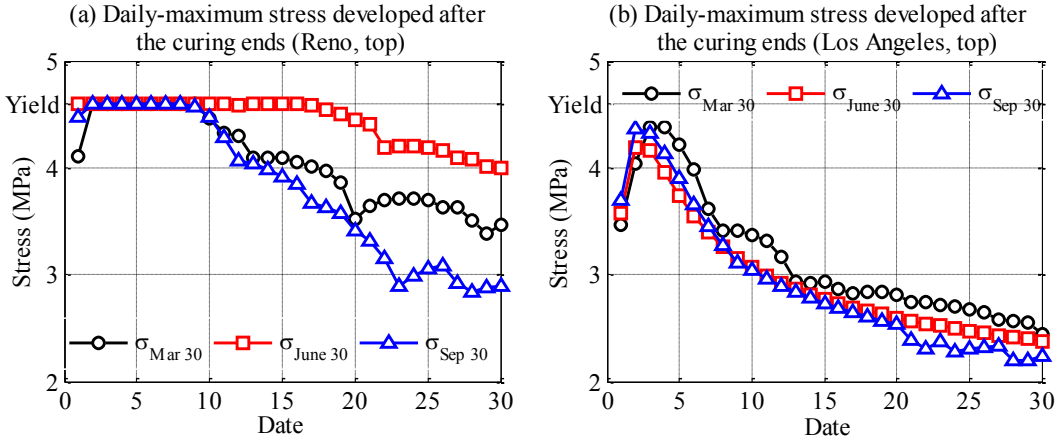

Figure 8.8 Influence of the slab-constructed seasons on the stress developed within slab after the curing ends.

Secondly, the RH of the slab in Reno is more easily affected by temperature variations. The hydrothermic coefficient reveals that the internal concrete RH is sensitive to temperature variation when the RH ranges from 0.4-0.6 (Figure 6.6). This sensitivity forces the slab in Reno to incur higher tensile stresses because the daily reductions of the RH near the top of the slab are relatively larger. This reduction is dramatic during the nighttime, as shown in the temperature decrease of the slab in Reno (Figure 3.3b).

Finally, the windier climate in Las Vegas (Figure 8.10c) reduces the thermal stress developed through the slab and reduces the diffusivity of the slab. The wind speed in Las Vegas is typically 1.0-1.5 m/s greater than in Reno. This windy climate in arid regions can reduce the environmental loading developed through a slab due to three reasons.

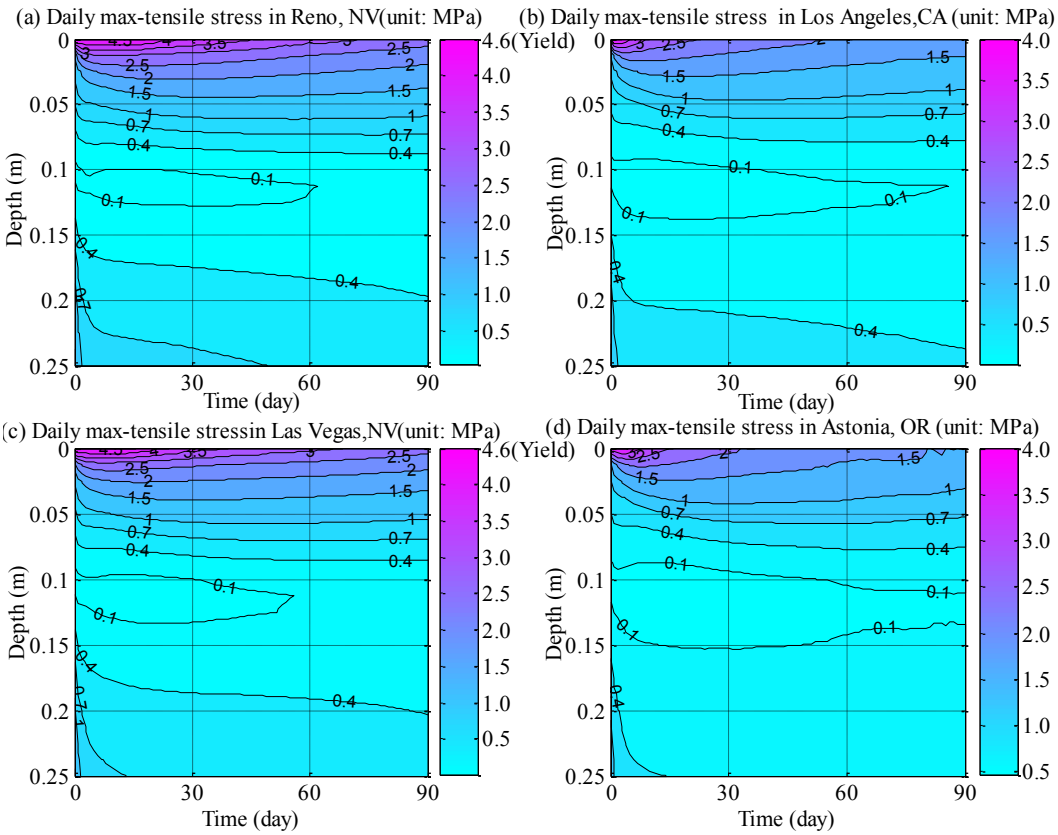

Figure 8.9 Daily maximum slab-tensile stresses developed in different regions.

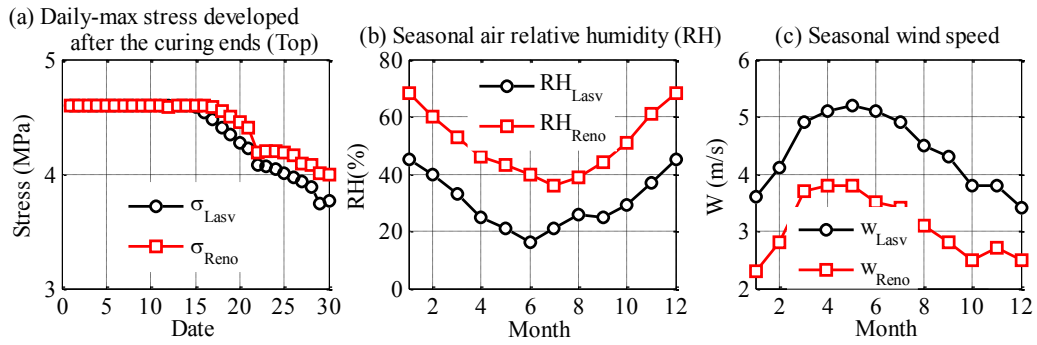

Figure 8.10 Slab's stress development and weather conditions.

1. First, this windy climate reduces the nonlinearity of the temperature gradient near the top and lessens the bending stress across the slab. It thus reduces the thermal stress developed and thus the total stress.

2. The windy climate in Las Vegas reduces the temperature across the slab. It thereby decreases the moisture diffusivity of the slab since the slab moisture diffusivity increases with temperature (Eq. (6.15)).

3. The windy climate in Las Vegas does not notably affect the moisture distribution within the slab. As there are very few rain events occurring in either region, the slab surface is in drying conditions most of the time. These conditions make the slab moisture distribution insensitive to the wind speed, as illustrated in Chapter 7.

These three reasons confirm that the windy climate in Las Vegas can decrease the total environmental loadings developed through the slab therein.

8.3.5.2 Application to other regions

Although the data from Figure 8.4 to Figure 8.8 reflects only the moisture distribution within in-service slabs in Reno and partly represent that in Los Angeles, the predicted total stress developed within the slabs can be extended to other regions.

A rapid escape of moisture from the slab surface is the main reason resulting in the larger tensile stress near the surface. After the curing ends, concrete pavement slabs are satured through their depth regardless of region; whereas the surrounding air has relatively lower RH. This difference results in a rapid moisture loss from the slab surface and induces tensile stress at the top. In regions with a relatively higher ambient RH (e.g. RH>0.75), the moisture escape occurs for a shorter duration because the moisture diffusion within a saturated slab is greater than within an unsaturated slab. Therefore, the developed stress relaxes soon after the curing terminates (Figure 8.8 and Figure 8.9). In regions with a lower ambient RH (e.g. RH<0.75), the moisture near the concrete slab's surface would quickly equilibrate to the ambient RH. However, the portion of the slab deeper in the slab is still saturated because the lower RH near the slab surface (less diffusion near the surface) blocks the continuous, rapid loss of moisture from the slab surface. A greater negative RH gradient thereby develops near the surface. This formation of this gradient results in the stress softening occurring at the slab surface, but the deeper portions of the slab remain at a relatively lower stress state (Figure 8.9a and c).

Arguments in the above paragraph confirm that the developed stress through slabs in other regions still experience similarly developed total stresses to those in Reno and Los Angeles. That is the following:

- Tensile stresses at the top would be close to the bending tensile strength. This is the case since the moisture escape is so quick that the rate of the shrinkage-induced stress development overwhelms rate of stress relaxation.
- The relaxation of the stress to a cyclically-stabilized state lasts several months. The rate of moisture loss reduces several days after the curing terminates. This is because in regions with higher ambient RH, the moisture loss declines. This is also because in regions with less ambient RH, the nonlinearity of the moisture diffusion impedes the moisture loss rates exponentially. When the

rate of stress relaxation is quasi-balanced with the rate of the shrinkage-induced stress, the total stress reaches a cyclically-stabilized state.

- The total stresses at the cyclically-stable state possibly divert from the thermal stresses. The degree of the divergence may exhibit different scenarios, depending on the daily temperature amplitude of the slab. In regions where the slab undergoes a relative lower temperature variation, the total stress may eventually converge to the total stress because $\dot{T}$ and $\dot{h}$ in Eq. (8.6) are minimal so that the Pickett effect and the viscosity behavior can relax the developed stress immediately.
- The construction season influences the developed stresses after the curing ends. This influence may also exhibit different scenarios than what is plotted in Figure 8.8. This is because other regions have different seasonal ambient relative humidity, wind speed, solar radiation, etc. It also may not reach a solution that a slab paved in September would be result in a lower stress developed immediately after the curing ends. However, it can be concluded that paving a slab in a season with less daily temperature amplitude and with higher ambient RH increase the likelihood of better performance of in-service slabs due to the reduced environmental stresses developed.

8.4 Discussion

8.4.1 Sensitivity of the developed total stress to the pavement slab

The simulation in this study hardly exhausts the possible factors that influence the total stresses developed through a slab. These factors can be divided into four sets: pavement structure constraints; slab mechanical parameters; slab shrinkage characteristics; and environmental factors.

8.4.1.1 Slab mechanical parameters

The total stress development also relies on the slab's mechanical parameters such as the viscosity of the slab. An increase of the viscosity will elongate transition time that the developed total stresses become stable. Conversely, a reduction of the slab's viscosity reduces the shrinkage-induced stress. In this case, the plateau of the stress curve in Figure 8.8a may not be present, meaning that the softening of the total stress would not occur. Therefore, the detailed magnitudes of the total stress strongly rely on the mechanical parameters of the slab.

Dependency of the total stress development on the elastic mechanical parameters is relatively complicated. Intuitively, an increase of the Young's modulus raises the estimated total stress and thermal stress; whereas increase of the Poisson rate declines those stress. A rise of Young's modulus from 20GPa to 30GPa would results in a 1.5 factor increase of the plotted stresses shown in Figure 8.4 to Figure 8.8. However, this

factor actually acts in a more complicated behavior because increase of these stresses promotes the drying shrinkage of the slab (Hansen and Almudaiheem 1987). This is because the variation of the stress alters both the creep effect and the Pickett effect of the slab. Nonlinearity of these effects complicates the role of the elastic mechanical parameters on the total stress development.

8.4.2 Slab mixture properties

Decrease of water-to-cement ratio reduces the total stress developed through in-service concrete slabs. This study does not refer to those slabs mixed with cementitious materials such as fly ash and only considers the mixture properties of normal Portland cement concrete. Provided that all the other conditions are the same, the slab containing different water-to-cement ratio results in different estimated total stresses. A lower w/c ratio concrete slab impedes a faster moisture escape from the concrete slab so that there should be less shrinkage-induced stress after the curling ends. Such a slab also has a less ultimate shrinkage ϵ_{sh} (Hansen and Almudaiheem 1987; Bissonnette et al. 1999). It thus has less reversible and irreversible shrinkage and experience relatively less environmental loadings. However, extremely low water-to-cement ratios (< 0.30) may exacerbate the autogenous shrinkage component within the ultimate shrinkage level.

A lower water-to-cement ratio concrete slab also results in the final total stress diverging to a lesser degree from the thermal stress. In the cyclically-stabilized state, the equivalent relative humidity (RH_{equ}) of a slab is stable such that the daily moisture-varied rate of the pore RH depends on the daily temperature cycle, but not on the variation of the pore water content. This means that in a specific region, the $\dot{\epsilon_{sh}}$ depends only on the ultimate $\epsilon_{sh\infty}$ (Eq. (8.2)). A decrease of the water-to-cement ratio thus reduces the $\dot{\epsilon_{sh}}$ and according to Eq. (8.2), leads to the reduction of the warping-induced stress.

8.4.3 Impact of wetting cycles

The occurrence of the wetting events reduces the shrinkage-induced stress. This is the case if the events occur after the curing ends and after the stabilized state reaches. Undoubtedly, the occurrence of wetting events after the curing ends reduces the rate of moisture loss and thus diminishes the shrinkage induced tensile stresses. After the cyclically-stabilized state is reached, a rain event can make the slab suffers from less thermal gradient and less daily variation of slab's RH. The latter reduces the warping stress. Also, rainy events increase the near surface moisture content and RH. This reduces the term of reversible shrinkage because the term of the reversible shrinkage (k_h in Eq.(8.3)) decreases as RH increases. Therefore, a rainy event during the cyclically-stabilized state decreases both thermal stresses and the shrinkage-induced stresses.

8.4.4 What does the estimation of total-stress evolution tell us?

A sophisticated model is needed to estimate the total environmental loadings that an in-service slab is subjected to. Without a credible model, these loadings would potentially be improperly characterized, especially the tensile stress near the top. First, a sole analysis to the thermal stress may delude us to believe that after the curing ends, the hot climate makes the slab surface slab compressed, but this is not the case. The developed shrinkage-induced tensile stress is so great that the tensile stress overwhelms the compression resulting from the temperature increase. Secondly, even when moisture evolution within a slab is in a quasi-balanced state, the dependency of the slab's RH on the temperature variation still results in the total stress at the stable state diverting from the thermal stress.

8.5 Conclusions

This study estimates the total warping and curling stress developed through in-service slabs after the curling ends. The following conclusions can be drawn:

(1) Immediately after the curing is terminated, the shrinkage-induced stress overwhelms the thermal stress. During several days after the curling, the slab top still suffers from only tensile stress but not compressive stress, even during a hot season. The total tensile stresses during the night time can be greater than the bending strength of normal Portland concrete, inducing slab surface softening through microcracking at shallow depths. However, this stress softening only occurs near the top; it may not occur in the regions with higher surrounding air RH.

(2) Decrease of water-to-cement ratio reduces the total stress developed through in-service concrete slabs. A lower w/c ratio concrete slab impedes a faster moisture escape from the concrete slab so that there should be less shrinkage-induced stress after curling ends. Such a slab typically also has a less ultimate shrinkage, unless extremely low w/c ratio concrete is placed. It thus has less reversible and irreversible shrinkage and experiences less environmental loadings. A lower water-to-cement ratio concrete slab also results in the final total stress diverging less from the thermal stress because of the lower ultimate shrinkage of this slab.

(3) Dependency of the total stress development on the elastic mechanical parameters is relatively complicated. Intuitively, an increase of the Young's modulus raises the estimated total stress and thermal stress; whereas increase of the Poisson rate reduces those stresses. The role of these two parameters, however, acts in a more complicated behavior since an increase of these stresses promotes the drying creep of the slab. This is because the variation of the stress alters both the creep effect and the Pickett effect of the slab. Nonlinearity of these effects complicates the role of the slab's elastic mechanical parameters on the total stress development.

(4) The developed stress through the slab relaxes exponentially. Approximately 3-6 months are required to make this stress cyclically-stabilized. At the cyclically-stabilized state, the total stress does not converge to the thermal stresses. This is because the RH

through a slab varies the temperature fluctuation across the slab. Variation of temperature leads to variations in both the internal pore RH and reversible shrinkage rate, which make the total tensile stress divergent from the thermal stress. Thus, it may lead to delusive results if the environmental loadings that the in-service slab subjects to are estimated by a model that solely analyzes the thermal stress.

Chapter 9 Conclusions and future works

This dissertation investigates the total environmental loadings that in-service slabs are subjects to by estimating the thermal- and shrinkage-induced stresses. The thermally-induced stress is evaluated by use of a 1-D dimensional heat transfer model to predict the temperature distribution through the slab and by use of the elastic theory to compute the stress induced by the predicted temperature profile. The shrinkage-induced stress is evaluated by use of the visco-elastic theory to compute the stress induced by the moisture gradient developed though the slab. Moisture distribution is predicted by a proposed model that considers the wetting and drying cycles occurring at the pavement surface. The computation of the total environmental loadings considers the relaxation behavior and Pickett effect of the concrete.

9.1 Conclusions

(1) Air temperature

The daily temperature amplitude affects the temperature distributions across a pavement slab during the daytime more than during nighttime. Pavements in regions with higher daily temperature amplitudes experience greater negative temperature gradients during the nighttime hours. Using a sinusoidal approximation function as an input of air temperature in a numerical model does not compromise the prediction, even if a sudden air temperature drop or increase occurs. There exists several correlations between air and sky temperatures. Uses of different correlations result in different temperature distributions through a concrete slab. Methods that directly link the sky emissivity to dew point are recommended in a numerical model commissioning to predict pavement temperatures.

(2) Wind speed

Impact of wind velocity on the thermal stresses in JPCPs depends on the climatic location of the pavement. In lower latitude regions, the solar radiation heats up the pavement surface and thus increases the difference between the slab-surface temperature and the air temperature ($T_s - T_a$). A relatively higher $T_s - T_a$ facilitates the wind drawing more heat from the pavement and thus reduces the temperature gradient and thermal development through the slab. This impact varies seasonally. In summer, the $T_s - T_a$ is maximal and the role of wind speed is magnified. In other seasons, the solar radiation wanes so that the $T_s - T_a$ factor decreases. The wind speed only carries a limited heat away from the pavement surface. It thus plays un-notable role on the slab temperature distribution and thus on the developed thermal stress.

Using the heat convection coefficient from the EICM to predict the temperature profile of a slab tends to overestimate thermal stresses in a JPCP. This may help explain some of the sensitivity of the thermal expansion coefficient to the predicted fatigue

cracking performance in JPCPs. Moreover, the EICM heat convection formula embeds an assumption that the slab surface temperature must be higher than the air temperature. This assumption is not always true. Furthermore, the heat convection coefficient estimate from the EICM model is significantly less than the value computed from accepted heat transfer theory. Use of this model potentially results in the thermal stresses being less sensitive to wind speed. The proposed modified model considers the factors of the viscosity of the air, characteristic length of the JPCP slab, the air's thermal conductivity, air Prandtl number, and wind velocity. It tends to be more realistic in characterizing the heat convection coefficient for a JPCP structure.

The wind speed observed from a weather station cannot be directly inputted into the Menzel's formula to compute the evaporation rate of bleed water from a casting concrete surface. The observed wind speed of weather stations in most locations (e.g. airports) generally is one-and-half times greater than the wind velocity used in Menzel's formula. This is because the heights of the measurements are different than wind speeds that affect the surface directly.

During wetting conditions, both wind speed and free evaporation (zero wind speed) significantly affect the moisture escape from the concrete surface. During the drying cycle, wind velocity dominates the moisture loss at slab surface, especially during the transition time that the relative humidity at the top approaches the ambient air humidity. Free evaporation at a drying concrete surface plays a negligible role to the moisture escape in cases with wind at the surface.

(3) Solar radiation (SR)

The temperature distribution and thermal-stress distribution through a slab are mainly determined by the SR absorption at the pavement surface. Because more SR energy is available during the summer season, the pavement experiences higher temperature gradients and thus suffers from higher thermal stress in comparison with winter months. The impact of the heat history on the pavement surface is negligible. Computation of the maximum pavement temperature thus needs only to predict the pavement temperature in the day with the extremely high solar radiation. The estimate of this extreme solar radiation, however, needs to consider the observed uncertainties of the local weather.

The role of SR absorption on the slab surface becomes more pronounced when with darken pavement surfaces. The maximum thermal tensile stress of a slab can increase up to 0.3MPa when the pavement surface's solar absorptivity rises from 0.65 to 0.85.

(4) Internal relative humidity of concrete

Seasonal ambient air relative humidity (RH) plays a dominant role on the moisture distribution within an in-service slab. The seasonal rainfall pattern, monthly wind speed, and variation of daily relative humidity influence the internal RH profile of the concrete in a secondary role. To offset the moisture gradients in arid climates, increased thickness or reduced joint spacing may need to be applied in comparison with wetter regions.

Concrete easily absorbs moisture when wetting. It typically loses water much slower due to the non-linearity of moisture diffusivity. Thus, although the probability of

precipitation is typically one order of magnitude less than drying in many locations, the magnitude of the wetting events still control the moisture budget of in-service slabs to a large degree.

Variation of the temperature strongly influences pore RH of an in-service slab. Not only does the slab's diffusivity depend on the temperature, but also the pore RH strongly varies with the temperature variation. Use either of the RH predicted by the isothermal model or of the equivalent relative humidity (a relative humidity estimated at room temperature) potentially overestimate the slab RH during the colder seasons.

(5) Total environmental loadings that in-service slabs suffer from

Immediately after the curing terminates, the shrinkage-induced stress overwhelms the thermal stress such that several days after the curling, the slab top suffers from only tensile stress but not compressive stress, even in a hot season. The total tensile stress during the night time can be greater than the bending strength of normal Portland concrete and make the slab surface undergo softening. However, this stress softening only occurs near the top; it may not occur in the regions with higher air RH.

Decrease of water-to-cement ratio reduces the total stress developed through in-service slabs. A lower w/c ratio concrete slab impedes a faster moisture escape from the concrete slab so that there should be less shrinkage- induced stress after curling ends. Such a slab also has a less ultimate shrinkage, except in extremely low w/c ratio cases. It thus has less reversible and irreversible shrinkage and experiences relatively lower environmental loadings. A lower water-to-cement ratio concrete slab also results in the final total stress diverging less from the thermal stress because of the lower ultimate shrinkage of the concrete.

Dependency of the total stress development on the elastic mechanical parameters is relatively complicated. Intuitively, an increase of the Young's modulus raises the estimated total stress and thermal stress; whereas an increase of the Poisson rate declines those stress. The role of these two parameters, however, is played in a more complicated behavior because an increase of these stresses promotes the drying shrinkage of the slab. This is because the variation of the stress alters the creep effect and the Pickett effect of the slab. Nonlinearity of these effects complicates the role of the elastic mechanical parameters on the total stress development.

The developed tensile stress at the top relaxes exponentially. Approximately 3-6months are required to make this stress stabilized (cyclically). At the stabilized state, the total stress does not converge to the thermal stresses. This is because the pore RH through a slab varies with the temperature variation. Variation of temperature leads to variations in both the pore RH and reversible shrinkage rate, which make the total tensile stress divergent from the thermal stress. Thus, it may lead to delusive results if the environmental loadings that the in-service slab subjects to are estimated by solely analyzing the thermal stress.

(6) What is needed to be done at the next step?

It is needed to develop a sophisticated model to estimate the total environmental loadings that in-service concrete slab are subject to. Without a credible model, these loadings would potentially be improperly characterized, especially the tensile stress near the top. First, a sole analysis to the thermal stress may delude us to believe that after the curing ends, the hot climate make the slab surface slab compressed. But this is not the case. The developed shrinkage-induced tensile stress is so great that the tensile stress overwhelms the compression resulting from the temperature increase. Second, even when moisture evolution within a slab is in a cyclically stable state, the dependency of the relative humidity on the temperature variation still results in the final stress diverting from the thermal stress.

9.2 Future works

(1) Characterize the built-in curling

This dissertation centers on the temperature distribution and moisture distribution through in-service hardened concrete pavement slabs. The hydrating concrete is out of consideration. However, in-service slabs usually have a built-in curling, which is induced by non-uniformity of the hydrating heat releasing during the hydrating state. This heat normally results in a negative built-in temperature gradient because the released heat is trapped at the bottom of the slab but effectively escapes from the pavement surface. Only this gradient results in a tensile stress occurring at the near surface. That is, the computation of the thermal stresses should be super-positioned with the built-in curling. Although the built-in curling will eventually relax to some degree, neglecting this built-in curling stress may either underestimate or overestimate the thermal stress developed through the slabs.

(2) Compute the stress-strain relationship after the stress-softening takes place.

This dissertation does not consider the stress-softening of the slab. When the stress is greater than the bending tensile strength of the concrete, stress yield is assumed. Actually, this yield leads to damage and may initialize micro-cracking. The post-yield stress-strain correlation is thus more complicated. For instance, micro-cracking may take place so that the bending stress across the slab is relaxed dramatically. Further investigations need to be dedicated to this post-yield stress-strain response and to how this stress softening may initiate larger structural cracks under external traffic loadings.

(3) Estimate the fatigue damage of rigid pavement

Estimating the total environmental loadings that the slab is subject to is not the ultimate goal. In practice, the fatigue damage of the rigid pavement is of greater concern. The environmental loadings themselves, especially in the long term, do not lead to the cracking or even failure of the slab in most cases. Accumulation of fatigue damage is of primary concern especially in that both these loadings are of seasonal and daily cycles. Future researches need to center on this topic.

(4) Developed 2-D model to predicted the moisture and temperature through the slab

The models proposed in this dissertation are based on 1-D dimension heat and mass transfer theory. Use of these models means that edge of the slab has the same boundary as the middle of the slab. This leads to some errors because the media near the edge can have different thermal properties and different diffusivity than the media beneath the center of the slab.

(5) Considering the soaking effect on the moisture distribution within the slab

The proposed mass transfer used to simulate the pore RH distribution through in-service slabs adopts $RH = 1$ when the slab surface is wetting. In fact, the wetting concrete surface has RH>1. This means that the proposed mass transfer model uses a lower upper boundary value and possibly underestimates the moisture uptake during the wetting condition. The underestimation of the upper boundary may lead to some underestimation of the moisture distribution through the slab, although the total wetting time is an order-of-magnitude lower than the drying time. Future studies expect a model considering the soaking effect during the wetting time.

Reference

Ahren CD. 2007. Meteorology Today: An Introduction to Weather, Climate, and the Environment. 8edition. Belmont, CA, USA: Thomson Higher Eduction. p. 537.

Ainsworth M, Oden JT. 1997. A posteriori error estimation in finite element analysis. Computer Methods in Applied Mechanics and Engineering 142(1-2):1-88.

Al-Fadhala M, Hover KC. 2001. Rapid evaporation from freshly cast concrete and the Gulf environment. Construction and Building Materials 15(1):1-7.

Andersland OB, Ladanyi B. 1994. An Introduction to Frozen Ground Engineering. New York: Chapman&Hall. p. P352.

Andrade C, Sarría J, Alonso C. 1999. Relative humidity in the interior of concrete exposed to natural and artificial weathering. Cement and Concrete Research 29(8):1249-1259.

Armaghani JM, Larsen TJ, Smith LL. Temperature response of concrete pavements. Transportation Research Record; 1987; Washington D.C.: National Research Council. p. 23-33.

Asaeda T, Ca VT, Wake A. 1996. Heat storage of pavement and its effect on the lower atmosphere. Atmospheric Environment 30(3):413-427.

Bazant Z, Raftshol WJ. 1982. Effect of cracking in drying and shrinkage specimens. Cement and Concrete Research 12(2):209-226.

Bazant Z, Chern J. 1985. Concrete creep at variable humidity: constitutive law and mechanism. Materials and Structures 18(1):1-20.

Bazant Z. 1998. Mathematical modeling of creep and shrinkage of concrete. Chichester, West Sussex, United Kingdom: John Wiley&Sons Ltd.

Bazant Z. 2000. Creep and Shrinkage Prediction Model for Analysis and Design of Concrete Structures: Model B3. Farmington Hills, Michigan: Am. Concrete Institute.

Bažant Z, Najjar L. 1972. Nonlinear water diffusion in nonsaturated concrete. Materials and Structures 5(1):3-20.

Bažant Z, Kim J-K. 1991. Consequences of diffusion theory for shrinkage of concrete. Materials and Structures 24(5):323-326.

Bazant ZP. 1970. Delayed thermal dilatations of cement paste and concrete due to mass transport. Nuclear Engineering and Design 14(2):308-318.

Bazant ZP, Najjar LJ. 1971. Drying of concrete as a nonlinear diffusion problem. Cement and Concrete Research 1(5):461-473.

Bazant ZP, Asghari A. 1974. Computation of age-dependent relaxation spectra. Cement and Concrete Research 4(4):567-579.

Bazant ZP, Tsubaki T. 1980. Weekly singular integral for creep rate of concrete. Mechanics Research Communications 7(5):335-340.

Bazant ZP, Chern J-C, Thonguthai W. 1982. Finite element program for moisture and heat transfer in heated concrete. Nuclear Engineering and Design 68(1):61-70.

Bazant ZP. 1983. Mathematical model for creep and thermal shrinkage of concrete at high temperature. Nuclear Engineering and Design 76(2):183-191.

Bazant ZP, Prasannan S. 1988. Solidification theory for aging creep. Cement and Concrete Research 18(6):923-932.
Bazant ZP. 2001. Prediction of concrete creep and shrinkage: past, present and future. Nuclear Engineering and Design 203(1):27-38.
Bentz DP. 2000. A computer model to predict the surface temperature and time-of-wetness of concrete pavements and bridge decks. National Institute of standards and technology, NISTIR 6551.
Berdahl P, Fromberg R. 1982. The thermal radiance of clear skies. Solar Energy 29(4):299-314.
Bissonnette B, Pierre P, Pigeon M. 1999. Influence of key parameters on drying shrinkage of cementitious materials. Cement and Concrete Research 29(10):1655-1662.
Bradbury RD. 1938. Reinforced concrete pavement. Washington D.C.: Wire Reinforcedment Institute.
Burden RL, Faires JD. 2000. Numerical analysis (7 Edition). Pacific Grove, California, United States: Brooks Cole. p. 864.
Burkan Isgor O, Razaqpur AG. 2004. Finite element modeling of coupled heat transfer, moisture transport and carbonation processes in concrete structures. Cement and Concrete Composites 26(1):57-73.
Centeno V M. 1982. New formulae for the equivalent night sky emissivity. Solar Energy 28(6):489-498.
Chrisp TM, McCarter WJ, Starrs G, Basheer PAM, Blewett J. 2002. Depth-related variation in conductivity to study cover-zone concrete during wetting and drying. Cement and Concrete Composites 24(5):415-426.
Chung Y, Shin H-C. Characteristics of coefficient of thermal expansion of PCC pavement. Transportation Research Record 2009 Annual meeting CD-ROM; 2008; Washington D.C.: National Academy Council. p. 1-18.
Dalton J. 1802. Experimental Essays on Evaporation. Preceedings of the Manchester Literary and Philosophical Society 5:536-602.
Dempsey BJ, Herlach WA, Patel AJ. 1985. The Climatic-Material-Structural Pavement Analysis Program, Final report. Washington D.C.: Federal Highway Administration.
Dreyfus M, Hilleary DT. 1962. Clear sky emissivity. Aerospace Engineering 21:42-42.
Fife JP, Nokes SE. 2002. Evaluation of the effect of rainfall intensity and duration on the persistence of chlorothalonil on processing tomato foliage. Crop Protection 21(9):733-740.
Ge Z. 2005. Predicting temperature and strength development of field concrete. [Amers, Iowa]: Iowa State University. p. 215.
Goering DJ, Kumar P. 1996. Winter-time convection in open-graded embankments. Cold Regions Science and Technology 24(1):57-74.
Grasley Z, Lange D, D'Ambrosia M. 2006. Internal relative humidity and drying stress gradients in concrete. Materials and Structures 39(9):901-909.

Gui J, Phelan PE, Kaloush KE, Golden JS. 2007. Impact of Pavement Thermophysical Properties on Surface Temperatures. Journal of Materials in Civil Engineering 19(8):683-690.
Hall C. 1989. Water sorptivity of mortars and concretes: a review. Magazine of concrete research 41(147):51-61.
Hansen W, Almudaiheem JA. 1987. Ultimate drying shrinkage of concrete--influence of major parameters. ACI Material Journal 84:217-223.
Hanzic L, Ilic R. 2003. Relationship between liquid sorptivity and capillarity in concrete. Cement and Concrete Research 33(9):1385-1388.
Heath AC, Roesler JR, Harvey JT. 2003. Modeling Longitudinal, Corner and Transverse Cracking in Jointed Concrete Pavements. International Journal of Pavement Engineering 4(1):51 - 58.
Hermansson Å. 2000. Simulation Model for Calculating Pavement Temperatures Including Maximum Temperature. Transportation Research Record: Journal of the Transportation Research Board 1699(1):134-141.
Hill RD, Braun MJ. 2001. Geolocation by Light Level--The Next Step: Latitude. Dordrecht, Netherland: Kluwer Academic Press.
Hiller JE. 2007. Development of mechanistic-empirical principles for jointed plain concrete pavement fatigue design. [Urbana,IL]: University of Illinois at Urbana-Champaign. p. 317.
Hiller JE, Roesler JR. Mechanistic-Empirical Thickness Design Methods and Predicted Critical Fatigue Locations. Proceedings of the 9th International Conference on Concrete Pavements; 2008; San Francisco, CA.
Hiller JE, Roesler JR. 2010. Simplified nonlinear tempeature curling analysis for Jointed concrete pavement. Journal of Transportation Engineering 131(8):654-663.
Hong AP, Li YN, Bazant ZP. 1997. Theory of Crack Spacing in Concrete Pavements. Journal of Engineering Mechanics 123(3):267-275.
Hover KC. 2006. Evaporation of Water from Concrete Surfaces. ACI Material Journal 103(5):384-389.
Huang CLD, Siang HH, Best CH. 1979. Heat and moisture transfer in concrete slabs. International Journal of Heat and Mass Transfer 22(2):257-266.
Huang YH. 2004. Pavement analysis and design. Upper Saddle River, NJ: Pearson Education, Inc.
IDIART AE. 2009. Coupled analysis of degreation processes in concrete specimens at the meso-level. [Barcelona]: UNIVERSITAT POLITÈCNICA DE CATALUNYA. p. 224.
Ioannides AM, Khazanovich L. 1998. Nonlinear Temperature Effects on Multilayered Concrete Pavements. Journal of Transportation Engineering 124(2):128-136.
Janssen DJ. 1987. Moisture in portland cement concrete. Transportation Research Record: Journal of the Transportation Research Board 1121:40-44.
Jean C, Jean-Marie K. 2005. Thermal conductivity of base-course materials. Canadian Geotechnical Journal 42(1):61-78.

Jensen OM, Hansen PF. 1999. Influence of temperature on autogenous deformation and relative humidity change in hardening cement paste. Cement and Concrete Research 29(4):567-575.
Jeong J-H, Zollinger D. 2003. Development of Test Methodology and Model for Evaluation of Curing Effectiveness in Concrete Pavement Construction. Transportation Research Record: Journal of the Transportation Research Board 1861(-1):17-25.
Jeong J-H, Zollinger DG. 2005. Environmental Effects on the Behavior of Jointed Plain Concrete Pavements. Journal of Transportation Engineering 131(2):140-148.
Jiji LM. 2009. Heat Convection (Second Edition). Berlin Heidelberg: Springer.
Johanneck L, Khazanovick L. Comprehensive Evaluation of Effect of Climate in MEPDG Predictions. TRB 89th Annual Meeting Compendium of Papers DVD 2010; Washington, D.C.: Transportation Research Board. p. 1-19.
Jooss M, Reinhardt HW. 2002. Permeability and diffusivity of concrete as function of temperature. Cement and Concrete Research 32(9):1497-1504.
Kannekanti V, Harvey J. 2006. Sensitivity Analysis of 2002 Design Guide Distress Prediction Models for Jointed Plain Concrete Pavement. Transportation Research Record: Journal of the Transportation Research Board 1947(-1):91-100.
Kapila D, Falkowsky J, Plawsky JL. 1997. Thermal effects during the curling of concrete pavement. ACI Materials Journal 94(2):119-127.
Khan MI. 2002. Factors affecting the thermal properties of concrete and applicability of its prediction models. Building and Environment 37(6):607-614.
Kim J-K, Lee C-S. 1999. Moisture diffusion of concrete considering self-desiccation at early ages. Cement and Concrete Research 29(12):1921-1927.
Kim K-H, Jeon S-E, Kim J-K, Yang S. 2003. An experimental study on thermal conductivity of concrete. Cement and Concrete Research 33(3):363-371.
Kohler ER. 2005. Experimenal Mechanics of Crack Width in Full-Scale Section of Continuously Reinforced Concrete Pavements. [Urbana]: University of Illinois at Urbana-Champaign. p. 173.
Ladanyi OBAaB. 1994. An Introduction to Frozen Ground Engineering. New York: Chapman & Hall.
Leech C, Lockington D, Dux P. 2003. Unsaturated diffusivity functions for concrete derived from NMR images. Materials and Structures 36(6):413-418.
Leivo V, Rantala J. 2005. Moisture behaviour of a massive concrete slab with a low temperature floor heating system during the initial drying period. Construction and Building Materials 19(4):297-305.
Levinson R, Akbari H. 2002. Effects of composition and exposure on the solar reflectance of portland cement concrete. Cement and Concrete Research 32(11):1679-1698.
Li C, Li K, Chen Z. 2008a. Numerical Analysis of Moisture Influential Depth in Concrete and Its Application in Durability Design. Tsinghua Science & Technology 13(Supplement 1):7-12.

Li C, Li K, Chen Z. 2008b. Numerical Analysis of Moisture Influential Depth in Concrete During Drying-Wetting Cycles. Tsinghua Science & Technology 13(5):696-701.
Li K, Li C, Chen Z. 2009. Influential depth of moisture transport in concrete subject to drying-wetting cycles. Cement and Concrete Composites 31(10):693-698.
Liang RY, Niu Y-Z. 1998. Temperature and Curling Stress in Concrete Pavements: Analytical Solutions. Journal of Transportation Engineering 124(1):91-100.
Lin G, Liu Y, Xiang Z. 2010. Numerical modeling for predicting service life of reinforced concrete structures exposed to chloride environments. Cement and Concrete Composites 32(8):571-579.
Lu S, Ren T, Rong Y, Horton R. 2006. An improved model for predicting soil thermal conductivity from water content at room temperature. Soil Science Society of America Journal 71(1):8-14.
Luca J, Mrawira D. 2005. New Measurement of Thermal Properties of Superpave Asphalt Concrete. Journal of Materials in Civil Engineering 17(1):72-79.
Masad E, Taha R, Muhunthan B. 1996. Finite-Element Analysis of Temperature Effects on Plain-Jointed Concrete Pavements. Journal of Transportation Engineering 122(5):388-398.
Mather B. 1985. Discussoin on paper by Z. berhane: "evaporation of water from fresh mortar and concrete at different evironmental conditions. ACI Journal 82(6):931-932.
McCullough BF, Rasmussen RO. 1999. Fast track paving, Concrete temperature control and traffic opening criteria for bonded concrete overlays,. U.S Department of Transportation.
Menabde M, Seed A, Harris D, Austin G. 1997. Self-similar random fields and rainfall simulation. Journal of Geophysical Research Atmosphere 102(D12):13509-13515.
MEPDG. 2004. Guide for Mechanistic-Empirical Design of New and Rehabilitated Pavement Structures--Final Report Part 2 Design Input Chapter 3 Environmental Effects. In: NCHRP, editor. Champaign, IL. p. 1-49.
Mindness S, Young JF, Darwin D. 2002. Concrete. Upper Saddle River, NJ: Prentice Hall.
Minhoto M, Pais J, Pereira P, Picado-Santos L. 2005. Predicting Asphalt Pavement Temperature with a Three-Dimensional Finite Element Method. Transportation Research Record: Journal of the Transportation Research Board 1919(-1):96-110.
Mohamed A, Hansen W. 1997. Effect of Nonlinear Temperature Gradient on Curling Stress in Concrete Pavements. Transportation Research Record: Journal of the Transportation Research Board 1568:65-71.
Mohamed AR, Hansen W. 1996. Prediction of stresses in concrete pavements subjected to non-linear gradients. Cement and Concrete Composites 18(6):381-387.
Morabito P. 2001. Thermal properties of concrete variation with temperature and during the hydration phase. Milan, Italy: Department of Civil & Mining Engineering &Division of Structural Engineering.

Pane I, Hansen W, Mohamed AR. 1998. Three-Dimensional Finite element study on effects of nonlinear temperature gradients in concrete pavement. Transportation Research Record: Journal of the Transportation Research Board 1629:58-66.
Papagiannakis AT, Masad EA. 2007. Pavement design and materials. Hoboken, NJ: John Wiley & Sons.
Paris PC, Tada H, Donald JK. 1999. Service load fatigue damage -- a historical perspective. International Journal of Fatigue 21(Supplement 1):35-46.
Patel JK, Read CB. 1996. Handbook of the Normal Distribution--Second edition, Revised and Expanded. New York: Marcel Dekker. p. 427.
Philip JR, Vries DAd. 1957. Moisture movement in porous materials under temperature gradient. Transactions, American Geophysical Union 38(2):222-232.
Pickett G. 1942. The effect of change in moisture content on the creep of concrete under a sustained load. ACI Joumal 38:333-356.
Pollack HN, Huang S. 2000. Climate Reconstruction from Subsurface Temperatures. Annual Review of Earth and Planetary Sciences 28(1):339-365.
Priestley MJN TS. 1979. Discussion of the Paper Titled ‘‘Thermal Calculations for Bridge Design’’ by Hunt et al. Journal of the Structural Division 102(ST6):1277–1279.
Qin Y, Hiller JE. 2011a. Impacts of diurnal temperature cycles on the geothermal regime on Qinghai-Tibet Plateau. Cold Regions Science and Technology 65(3):429-436.
Qin Y, Hiller JE. 2011b. Modeling temperature distribution in rigid pavement slabs: Impact of air temperature. Construction and Building Materials 25(9):3753-3761.
Qin Y, Hiller JE. 2011c. Modeling the temperature and stress distributions in rigid pavements: impact of solar radiation absorption and heat history development. KSCE Jounral of Civil Engineering 15(11):In press.
Ramadhan RH, Al-Abdul Wahhab HI. 1997. Temperature variation of flexible and rigid pavements in Eastern Saudi Arabia. Building and Environment 32(4):367-373.
Richardson JM, Armaghani JM. 1987. Stress caused by temperature gradient in portland cement concrete pavement. Transportation Research Record: Journal of the Transportation Research Board 1121:7-13.
Rohsenow WM, Hartnett JP, Cho YI. 1998. Handbook of Heat Transfer. New York: McGraw-Hill. p. pp1501.
Šelih J, Sousa ACM, Bremner TW. 1996. Moisture transport in initially fully saturated concrete during drying. Transport in Porous Media 24(1):81-106.
Shah VN, Hookham CJ. 1998. Long-term aging of light water reactor concrete containments. Nuclear Engineering and Design 185(1):51-81.
Sivapalan M, Blöschl G. 1998. Transformation of point rainfall to areal rainfall: Intensity-duration-frequency curves. Journal of Hydrology 204(1-4):150-167.
Solaimanian M, Kennedy TW. 1993. Predicting maximum pavement surface temperature using maximum air temperature and hourly solar raidation. Transportation Research Record: Journal of the Transportation Research Board 1417:1-11.
Swinbank WC. 1963. Long-wave radiation from clear skies. Quarterly Journal of the Royal Meteorological Society 89(381):339-348.

Tang R, Etzion Y, Meir IA. 2004. Estimates of clear night sky emissivity in the Negev Highlands, Israel. Energy Conversion and Management 45(11-12):1831-1843.
Tang T, Zollinger DG, Senadheera S. 1993. Analysis of Concave Curling in Concrete Slabs. Journal of Transportation Engineering 119(4):618-633.
Thompson MR, B.J. Dempsey, Hill H, Vogel J. Characterizing temperature effects for pavement analysis and design. Transportation research record; 1987; Washington D. C.: National research council p. 7-13.
Torrenti JM, Granger L, Diruy M, Genin P. 1999. Modelling concrete shrinkage under variable ambient conditions. ACI Material Journal 96:35-39.
Uno PJ. 1998. Plastic Shrinkage Cracking and Evaporation Formulae. ACI Material Journal 95(4):365-375.
Natural resource conservation service [Internet]. 2009. http://websoilsurvey.nrcs.usda.gov/app/HomePage.htm. [updated cited. Available from: http://websoilsurvey.nrcs.usda.gov/app/HomePage.htm
Walton GN. 1985. Thermal Analysis Research Program--Reference Manua--lNBSIR 83-2655. New York: U.S. Department of Commerce.
Westergaard HM. 1927. Analysis of stresses in concrete roads caused by variations of temperature. Public Roads 8(3):54-60.
Historical Climate Information [Internet]. 2010. wrcc.dri.edu. [updated cited. Available from: http://www.wrcc.dri.edu/CLIMATEDATA.html
Witasse R, Georgin JF, Reynouard JM. 2002. Nuclear cooling tower submitted to shrinkage; behaviour under weight and wind. Nuclear Engineering and Design 217(3):247-257.
Wong SF, Wee TH, Lee SL. 2001. study of water movement in concrete. Magazine of concrete research 53(3):205-220.
Xi Y, Bazant ZP, Jennings HM. 1994. Moisture diffusion in cementitious materials Adsorption isotherms. Advanced Cement Based Materials 1(6):248-257.
Yavuzturk C, Ksaibati K, Chiasson AD. 2005. Assessment of Temperature Fluctuations in Asphalt Pavements Due to Thermal Environmental Conditions Using a Two-Dimensional, Transient Finite-Difference Approach. Journal of Materials in Civil Engineering 17(4):465-475.
Yu H, Khazanovich L, Darter M, Ardani A. 1998. Analysis of Concrete Pavement Responses to Temperature and Wheel Loads Measured from Intrumented Slabs. Transportation Research Record: Journal of the Transportation Research Board 1639(-1):94-101.
Yuan Y, Wan ZL. 2002. Prediction of cracking within early-age concrete due to thermal, drying and creep behavior. Cement and Concrete Research 32(7):1053-1059.

Appendix A—materials presented in Chapter 3

ELSEVIER LICENSE
TERMS AND CONDITIONS

May 22, 2011
This is a License Agreement between Yinghong Qin ("You") and Elsevier ("Elsevier") provided by Copyright Clearance Center ("CCC"). The license consists of your order details, the terms and conditions provided by Elsevier, and the payment terms and conditions.
All payments must be made in full to CCC. For payment instructions, please see information listed at the bottom of this form.

Supplier	Elsevier Limited The Boulevard,Langford Lane Kidlington,Oxford,OX5 1GB,UK
Registered Company Number	1982084
Customer name	Yinghong Qin
Customer address	1912B Woodmar Dr., Houghton, MI 49931
License number	2674441465472
License date	May 22, 2011
Licensed content publisher	Elsevier
Licensed content publication	Construction and Building Materials
Licensed content title	Modeling temperature distribution in rigid pavement slabs: Impact of air temperature
Licensed content author	Yinghong Qin, Jacob E. Hiller
Licensed content date	September 2011
Licensed content volume number	25
Licensed content issue number	9
Number of pages	9
Start Page	3753
End Page	3761
Type of Use	reuse in a thesis/dissertation

Appendix B—Materials presented in Chapter 5

SPRINGERLINK LICENSE
TERMS AND CONDITIONS
May 22, 2011
This is a License Agreement between Yinghong Qin ("You") and Elsevier ("Elsevier") provided by Copyright Clearance Center ("CCC"). The license consists of your order details, the terms and conditions provided by Elsevier, and the payment terms and conditions.
All payments must be made in full to CCC. For payment instructions, please see information listed at the bottom of this form.

License Number	2674451140605
License date	May 22, 2011
Licensed content publisher	Springer
Licensed content publication	KSCE Journal of Civil Engineering
Licensed content title	Modeling the Temperature and Stress Distributions in Rigid Pavements: Impact of Solar Radiation Absorption and Heat History Development
Licensed content author	Yinghong Qin, Jacob E. Hiller
Licensed content date	Nov 1, 2011
Volume number	15
Issue number	11
Type of Use	Thesis/Dissertation
Portion	Full text
Number of copies	1
Author of this Springer article	Yes
Title of your thesis / dissertation	Numerical study on the curling and warping of hardened rigid pavement slabs
Expected completion date	Jul 2011
Estimated size(pages)	110
Total	0.00 USD

Appendix C—1-D heat transfer model

```
% this program deals with 1-d heat transfer problem
% written by Yinghong Qin, all right reserved
% beta=0.5 is used to reduce the error.
clc;
clear;
%% geometry constants and thermal constants
para=xlsread('thermalpara.xls');
mat=length(para(:,1));
heatcon=para(:,2);
density=para(:,3);
heatcapa=para(:,4);
%
%% climatic input
% (1) solar radiation
latitude=39.5; % latitude of reno, NV
[sunrise,sunset]=sunrscal(latitude);
solar=xlsread('climatedata.xls','reno','C11:N13');
solarmean=solar(1,:); %mean solar radiation; in month; unit==kWh/m2/day;
solarmin=solar(2,:);  %min solar radiation; in month
solarmax=solar(3,:);  %max solar radiation ; in month
solarmean=solarmean*41.666; %http://en.wikipedia.org/wiki/Insolation; unit==w/m^2;
solarmin=solarmin*41.666; % convert
solarmax=solarmax*41.666; % convert
[daterefmin,daterefmax,datenum]=manudata(solarmax,solarmean,solarmin);
solarannual=12*pi*datenum./(sunset-sunrise);
% (2) inputted date referred
dewpoint=xlsread('climatedata.xls','dewpoint'); % unit 0F
dateref=[0;dewpoint(:,1);365];
% (3) daily temperature
temperature=xlsread('climatedata.xls','reno','C61:N63');
anmeanannual=temperature(1,:);
au=anmeanannual(1)/2+anmeanannual(end)/2;
anmeanannual=[au,anmeanannual,au];
flucannual=temperature(3,:)-temperature(2,:); %calculate
au=flucannual(1)/2+flucannual(end)/2;
flucannual=[au,flucannual,au]*0.5;
anmeanannual=interp1(dateref,anmeanannual,(0:365)','spline');
flucannual=interp1(dateref,flucannual,(0:365)','spline');
% (4) wind velocity
windannual=xlsread('climatedata.xls','reno','C69:N69'); % unit m/s
au=windannual(1)/2+windannual(end)/2;
```

```
windannual=[au,windannual,au];
windannual=interp1(dateref,windannual,(0:365)','spline');
% (5) air relative humidity
RHannual=xlsread('climatedata.xls','reno','C68:N68'); % unit m/s
au=RHannual(1)/2+RHannual(end)/2;
RHannual=[au,RHannual,au];
RHannual=interp1(dateref,RHannual,(0:365)','spline');
%% other parameters
%
Q=0; % heat generation;
emiss=0.93; %emissivity
sigma=5.669e-8; %stefan-boltzmann constant
cover=0.1; % cloud cover
absorp=0.78;
ch_length=0.151; %characteristic length
visco=16.01*10^-6; %viscocity of air
pr=0.7; % Pr numver of the air
kair=0.027; % wiki
%% space discrete
tbase=0.10;
enslab=10;
tslab=0.25; %unit m, 10in=0.254m
enbase=3;
[elink,coorlink,nelement,coorslab]=discrete(tslab,tbase,enslab,enbase);
slabelink=elink(1:10,:);
%% initial conditions
% give the initial temperature
nnode=length(coorlink(:,1));
%%
tt=xlsread('initial.xls','initial_reno');
tt=interp1(tt(:,1),tt(:,2),coorlink,'spline');
%% simulate preparation
tempall=[]; % used to store the temperature in the max solar radiation day of each month.
initialtemp=[];
years=1;
simu_days=365*years; % how much days is expected to be simulated
datecount=1; % use for save the initial temperature
solarradiation_annual=[];
for DAY=1:simu_days
    %% get the climatic data in the given day
    DAYAU=mod(DAY,365);
    anmean=anmeanannual(DAYAU+1);
    fluc=flucannual(DAYAU+1);
```

```
vwind=windannual(DAYAU+1);
RHday=RHannual(DAYAU+1);
solarr=solarannual(DAYAU+1);
%%
hr=24; %how much hours do you want?
t=hr*60*60;
dt=600;
U_day=[]; % a vector used to store the temperature of slab
countmax=1;
%
for time=0:dt:t
    cc=sparse(zeros(nnode,nnode));
    kk=sparse(zeros(nnode,nnode));
    rr1=zeros(nnode,1);
    %% loop over elements for stiffnes matrix
    for i=1:nelement
    % get the node number of element
    n1=elink(i,1);
    n2=elink(i,2);
    n3=elink(i,3);
    %determine which layer the element within------------------------
    if n2<tslab
        nmat=1;
    end
    if n2>tslab&&n2<tslab+tbase
        nmat=2;
    end
    if n2>tslab+tbase
        nmat=3;
    end
    % finish material properties determination----------------------
    lelement=coorlink(n3)-coorlink(n1);% calculate element length
    klocal=heatcon(nmat)/lelement*[7/3.,-8/3.,1/3.;-8/3.,16/3.,-8/3.;1/3.,-8/3.,7/3.];
    clocal=density(nmat)*heatcapa(nmat)*lelement*[2/15.,1/15.,-
1/30.;1/15.,8/15.,1/15.;-1/30.,1/15.,2/15.];
    rq=Q*lelement*[1.0/6;2.0/3;1.0/6];
    %assemble kk and cc
    kk(n1,n1)=kk(n1,n1)+klocal(1,1);
    kk(n1,n2)=kk(n1,n2)+klocal(1,2);
    kk(n1,n3)=kk(n1,n3)+klocal(1,3);
    kk(n2,n1)=kk(n1,n2);
    kk(n2,n2)=kk(n2,n2)+klocal(2,2);
    kk(n2,n3)=kk(n2,n3)+klocal(2,3);
```

```
        kk(n3,n1)=kk(n1,n3);
        kk(n3,n2)=kk(n2,n3);
        kk(n3,n3)=kk(n3,n3)+klocal(3,3);
        cc(n1,n1)=cc(n1,n1)+clocal(1,1);
        cc(n1,n2)=cc(n1,n2)+clocal(1,2);
        cc(n1,n3)=cc(n1,n3)+clocal(1,3);
        cc(n2,n1)=cc(n1,n2);
        cc(n2,n2)=cc(n2,n2)+clocal(2,2);
        cc(n2,n3)=cc(n2,n3)+clocal(2,3);
        cc(n3,n1)=cc(n1,n3);
        cc(n3,n2)=cc(n2,n3);
        cc(n3,n3)=cc(n3,n3)+clocal(3,3);
        rr1(n1)=rr1(n1)+rq(1);
        rr1(n2)=rr1(n2)+rq(2);
        rr1(n3)=rr1(n3)+rq(3);
        end
    % boundary condition giving
    % 1) air temperautre
    hour1=time/3600;
    airtemp1=anmean+fluc*sin(pi*(hour1-7)/12);
    [dewpointin]=dewcompute(RHday,  airtemp1);
    wind=vwind;
    tt1=tt(1);
    % 2) convection
    [qconv1]=reynolds(tt1,airtemp1,wind,ch_length,visco,kair,pr); % function
    % 3)irradiation
    refnum=2; % refnum 1--bentz model, 2--berdahl model, 3--Swinbank model
    [qirra1]=irrbentz(tt1,airtemp1,dewpointin,cover,sigma,emiss,refnum); % refnum 1--
bentz model, 2--berdahl model, 3--Swinbank model
    % 4)solar absorption

[qabsorp1]=solarradiation(hour1,absorp,solarr,sunrise(DAYAU+1),sunset(DAYAU+1)); %
function
    % 5) give heat flux to the top of slab
    rr1(1)=qconv1+qabsorp1+qirra1;
    rr1(nnode)=0.03*heatcon(3);
    %heat flux from the bottom of the earth
    % finish heat flux-------------------------------
    renewcc=cc/dt+0.5*kk;
    renewrr=0.5*rr1+(cc/dt-(1-0.5)*kk)*tt;%b=0.5;
    tt=renewcc\renewrr;
    %% 1) save the data on the maximum solar-radiation days
    if DAY/365>years-1
```

```
        if mod(time,3600)==0&&time~=0
            U_day=[U_day;tt(1:2*enslab+1)'];
            countmax=countmax+1;
        end
    end
    %% 2) save the data on the minimum solar-radiation days
    end
    tempall=[tempall;U_day];
end
tempall=[coorlink(1:2*enslab+1)';tempall];
tempall=[(-1:8759)'/24,tempall];
xlswrite('tempall.xls',tempall,'reno_wholeyear');
xlswrite('initial.xls',[coorlink,tt],'initial_reno');
```

Appendix D—couple heat- and mass-transfer model

```
% this program and its associated subroutines are designed to compute the
% moisture profile within the concret pavement slab;
% written by Yinghong Qin, all right reserved
clear all;
clc;
format long g;
%% 1) load weather conditions
days=365; % provide how much day you want to simulate
dayloopbegin=1;
slen=0.254; %meter, 12in=30.48 centimeter
eslab=40; % how much elements you want
nodeslab=2*eslab+1; % total number of the slab
coor=linspace(0,1,nodeslab)';
% ************************************ % finish the discretization
slabelink=zeros(eslab,3);
for i=1:eslab
   slabelink(i,1)=2*i-1;
   slabelink(i,2)=2*i;
   slabelink(i,3)=2*i+1;
end
% ++++++++++++++++++++++++++++++++++++++ % finish the link
%% 3)^^^^^^^^^^^^^^^^^^^^^^^^^^^^ % give the parameter relative to diffusivity
wc=0.45; % water cement ratio
% 3) porosity of concrete slab
C1_25=[0.28,0.86;0.4,1.59;0.68,2.57];
C1_25=interp1(C1_25(:,1),C1_25(:,2),wc,'spline')*10^-6;
alpha0=0.10;
hc=0.75;
n=6; % see bazant paper
QR=1300; % Q/R see bazant paper
temp_ref=22;
T0=temp_ref+273; % reference temperature;
%% give the initial boundary conditions
initialcon=[0*0.0254 1;0.5*0.0254,1;1*0.0254 1; 2*0.0254 1;3*0.0254 1;4.5*0.0254 1;
5*0.0254 1; 6*0.0254 1;8*0.0254 1;9*0.0254 1;10*0.0254 1];
coorindex=coor*slen;
RHa=interp1(initialcon(:,1),initialcon(:,2),coorindex,'linear');
%RHa=0.98*ones(nodeslab,1);
%%
A=199.65976; % 186.65976;
% ************************************
```

```
%% 4) other parameters

%  &&&&&&&&&&&&&&&&&  finish the inital condition
incre=days*24*1; % increment of time unit hour
URH=zeros(incre+1,nodeslab); % a vector used to store the moisture of slab
URH_real=zeros(incre+1,nodeslab);
count=1;
%% interpolation the weather data
% (1) wind speed and air relative humidity
windrhdata=xlsread('climatedata.xls','reno','C68:N69');
rhdata=windrhdata(1,:); % get the relative humidity
winddata=windrhdata(2,:); % get the wind speed;
%
%windrhdata=xlsread('climatedata.xls','losangeles','C68:N69');
%rhdata=windrhdata(1,:); % get the relative humidity
%winddata=windrhdata(2,:); % get the wind speed;
%
% (2) rainfall information
consthour=1; % the hour of construction 10---10AM;
slag=xlsread('slag.xls','reno_d'); % "reno_d' or 'losa_d'
%% 2)************************************ % discretize the space
[vwind]=datacomputenoflu(winddata,incre,dayloopbegin,1);%197 suggest the
construction at the middle of the July;
% air relative humidty
airrehum=xlsread('climatedata.xls','losangeles922','S32:T56');
[xreno,rhfit,R2]=rhamplitude(airrehum); % retude the amplitude of daily relative
humidity
[RHair]=airrh(rhdata,incre,dayloopbegin,consthour,xreno);
%%
temp=xlsread('tempall.xls','reno_wholeyear');
temp_all=[];
for i=2:length(temp(2:end,1))+1
   temp_au=interp1(temp(1,2:end),temp(i,2:end),coorindex(1:2*eslab+1),'spline');
   temp_all=[temp_all;temp_au'];
end
temp_all=[temp_all;temp_all(1,:)];
coeff=[];
rh_real_initial=RHa;
%% all the inputted data would be arranged here by use of the "shiftinfo"
%% function to meet the construction-season requirement.
dateindex=(0:8760)'/24+1; % the first not the 0th day but 1day
construct_begin=181;  %220;
construct_hour=1;
```

```
[RHair]=shiftinfo(RHair',construct_begin,construct_hour);
[slag]=shiftinfo(slag,construct_begin,construct_hour);
[vwind]=shiftinfo(vwind',construct_begin,construct_hour);
[temp_all]=shiftinfo(temp_all,construct_begin,construct_hour);
%%
yearrun=5;
moisture_all=[];
moisture_all_equ=[];
for yearrun=1:5

%%
++++++++++++++++++++++++++++++++++++++++++++++++++++++++++++++++++++++++
++++++++
for step=1:incre+1
   %
   T1=mean(temp_all(step,:))+273;
   coef=T1/T0*exp(QR/T0-QR/T1); % hydrocoefficient;
   C1=C1_25*coef;
   tlen=slen^2/(C1); %tlen=t0
   t_max=days*24/tlen;
   timest=linspace(0,t_max,incre+1);
   dt=timest(2)-timest(1);
   %
   cc=sparse(zeros(nodeslab,nodeslab));
   kk=sparse(zeros(nodeslab,nodeslab));
   rr=zeros(nodeslab,1);
   % the temperature of the slab is expected to be input from here
   % but it should be noted that the time step and the increment is the
   % same and also the calculated should be one by one step
   %% loop over elements for stiffnes matrix
   for i=1:eslab
      % get the node number of element
      n1=slabelink(i,1);
      n2=slabelink(i,2);
      n3=slabelink(i,3);
      lelement=coor(n3)-coor(n1);% calculate element length
      %determine the position of is wet of dry-----------------------
      %if RHa(n1)==1
         %Cfir=D0w*exp(Nwet*RHa(n1))*kama;
      %else
         Cfir=C1*(alpha0+(1-alpha0)/(1+((1-RHa(n2))/(1-hc))^n)); % ???????????????
      %end
      %if RHa(n2)==1
```

```
        %Csec=D0w*exp(Nwet*RHa(n2))*kama;
        Csec=C1*(alpha0+(1-alpha0)/(1+((1-RHa(n2))/(1-hc))^n));
      %if RHa(n3)==1
        %Cthi=D0w*exp(Nwet*RHa(n3))*kama;
        Cthi=C1*(alpha0+(1-alpha0)/(1+((1-RHa(n2))/(1-hc))^n));
      audiag=[(Cfir*tlen)/slen^2,(Csec*tlen)/slen^2,(Cthi*tlen)/slen^2];
      Pe=diag(audiag,0); % peclet number
      % finish material properties determination----------------------
      klocal=1/(lelement)*Pe*[7/3.,-8/3.,1/3.;-8/3.,16/3.,-8/3.;1/3.,-8/3.,7/3.];
      clocal=lelement*[2/15.,1/15.,-1/30.;1/15.,8/15.,1/15.;-1/30.,1/15.,2/15.];
      %assemble kk and cc
      kk(n1,n1)=kk(n1,n1)+klocal(1,1);
      kk(n1,n2)=kk(n1,n2)+klocal(1,2);
      kk(n1,n3)=kk(n1,n3)+klocal(1,3);
      kk(n2,n1)=kk(n1,n2);
      kk(n2,n2)=kk(n2,n2)+klocal(2,2);
      kk(n2,n3)=kk(n2,n3)+klocal(2,3);
      kk(n3,n1)=kk(n1,n3);
      kk(n3,n2)=kk(n2,n3);
      kk(n3,n3)=kk(n3,n3)+klocal(3,3);
      cc(n1,n1)=cc(n1,n1)+clocal(1,1);
      cc(n1,n2)=cc(n1,n2)+clocal(1,2);
      cc(n1,n3)=cc(n1,n3)+clocal(1,3);
      cc(n2,n1)=cc(n1,n2);
      cc(n2,n2)=cc(n2,n2)+clocal(2,2);
      cc(n2,n3)=cc(n2,n3)+clocal(2,3);
      cc(n3,n1)=cc(n1,n3);
      cc(n3,n2)=cc(n2,n3);
      cc(n3,n3)=cc(n3,n3)+clocal(3,3);
    end
    %++++++++++++++++++++++++++++++++++++++++++++++++++++++++++++++++++++
++++
    % 1) wet at the slab's surface
    if slag(step)==1
      RHa(1)=1; % relative humidity at the top of the specimen
      renewcc =cc/dt;
      renewrr=(renewcc-kk)*RHa;
      ccff=renewcc(2:nodeslab,2:nodeslab);
      rrff=renewrr(2:nodeslab);
      ccfp=renewcc(1:1,2:nodeslab);
      rrff=rrff-RHa(1)*ccfp';
      RHf=ccff\rrff;
      RHa(2:end)=RHf;
```

```
        % begin the C-R method
        renewcc=cc/dt+0.5*kk;
        renewrr=(cc/dt-0.5*kk)*RHa;
        ccff=renewcc(2:nodeslab,2:nodeslab);
        rrff=renewrr(2:nodeslab);
        ccfp=renewcc(1:1,2:nodeslab);
        rrff=rrff-RHa(1)*ccfp';
        RHf=ccff\rrff;
        RHa(2:nodeslab)=RHf;
    % 2) drying cycle--need consider the convection at the ground surface
    else if slag(step)==0
        rr(1)=A*(0.253/21.89+0.216*vwind(step)*0.66)*(-RHa(1)+RHair(step)); % provide
a variable air relative humidity and vwind speed
        % 0.096 refers to Zawde berhane's paper
        renewcc=cc/dt+0.5*kk;
        renewrr=rr+(cc/dt-(1-0.5)*kk)*RHa;%b=0.5;
        RHa=renewcc\renewrr;
        end
    end
    for cor=1:length(RHa)
        if RHa(cor)>=1
            RHa(cor)=1;
        else if RHa(cor)<=0;
                RHa(cor)=0;
            end
        end
    end
    %
    [rh_real]=realrh(RHa,temp_all,step,rh_real_initial,temp_ref);
    rh_real_initial=rh_real;
    for cor=1:length(rh_real)
        if rh_real(cor)>=1
            rh_real(cor)=1;
        else if rh_real(cor)<=0;
                rh_real(cor)=0;
            end
        end
    end
    %
    URH(count,:)=RHa';
    URH_real(count,:)=rh_real';
    count=count+1;
```

```
   %
++++++++++++++++++++++++++++++++++++++++++++++++++++++++++++++++++++++++++++
end
moisture_all=[moisture_all;URH_real(1:end-1,:)];
moisture_all_equ=[moisture_all_equ;URH(1:end-1,:)];
URH=zeros(incre+1,nodeslab); % a vector used to store the moisture of slab
URH_real=zeros(incre+1,nodeslab);
count=1;
end
%
moisture_all=[moisture_all;rh_real'];
moisture_all_equ=[moisture_all_equ;RHa'];
index=(0:length(moisture_all(:,1)))'/24;
moisture_all=[coorindex';moisture_all];
moisture_all=[index,moisture_all];
moisture_all_equ=[coorindex';moisture_all_equ];
moisture_all_equ=[index,moisture_all_equ];
%
xlswrite('moisture_all.xls',moisture_all,'reno');
xlswrite('moisture_all.xls',moisture_all_equ,'reno_equ_rhnodaily');
```

Appendix E—compute the total environmental loads

```
clear all;
clc;
temp_all=xlsread('temp_more.xls','reno_beta');
moisture_all=xlsread('moisture_more.xls','reno_beta');
visco=xlsread('visco.xls','viscofit');
%
%
coor_temp=temp_all(1,2:end);
coor_moisture=moisture_all(1,2:end);
total_stress=[];
thermal_stress=[];
[initialstress]=thermalstressprofile(temp_all(1:2,2:end));
%
total_stress=[total_stress;initialstress];
thermal_stress=[thermal_stress,initialstress];
shrinkagemax=600;
dayload=3;
%
[M,N]=size(temp_all(2:end,2:end));
hour=(1:M+2)';
[visco_hour]=visco_compute(visco,hour);
%
deformtrack=[];
creep=zeros(1,N);
%
for i=3:M
   visco=visco_hour(i)*10^6;
   temp=[coor_temp;temp_all(i-1:i+1,2:end)];
   moisture=[coor_moisture;moisture_all(i-1:i+1,2:end)];
   day=dayload+i/24;
   %[thermalstress,moisturestress,totalstress,
initialstress,deform]=stresscalculaterevise(temp,moisture,initialstress,shrinkagemax,visco
,dayload,day);
   [thermalstress,totalstress,
initialstress,deform]=stresscalculaterevise(temp,moisture,initialstress,shrinkagemax,visco
,dayload,day);
   total_stress=[total_stress;totalstress];
   thermal_stress=[thermal_stress;thermalstress(2,:)];
   %moisture_stress=[moisture_stress;moisturestress];
   deformtrack=[deformtrack;deform];
end
```

```
xlswrite('stress_all.xls',[temp_all(1:M,1),total_stress],'totalstress_reno');
xlswrite('stress_all.xls',[temp_all(1:M,1),thermal_stress],'thermalstress_reno');
% this function is designed to computed the thermal induced stress,
% moisture induced stress, and the total stress
function [thermalstress,totalstress,
initialstress,deform]=stresscalculaterevise(temp,moisture,initialstress,shrinkagemax,visco
,dayload,day)
EMOD=2.0586e10;
NU=0.15;
EXP=9e-6; % the expansion
Emulti=EMOD/(1-NU);
%%
% interpolate data according to the initial strss coor
tempuse=[];
for i=1:3
   au=interp1(temp(1,:),temp(i+1,:),moisture(1,:),'spline');
   tempuse=[tempuse;au];
end
moistureuse=moisture(2:4,:);
au=interp1(initialstress(1,:),initialstress(2,:),moisture(1,:),'spline');
initialstress=[moisture(1,:);au];
temp=[moisture(1,:);tempuse];
%
%
threshold=2;
%
[DEDsh]=desh_dt(day,dayload,shrinkagemax,moistureuse);
[DeDT]=tempratedeformation(EXP,tempuse);
[DeDsh]=pickettmoisture(shrinkagemax,moistureuse, initialstress(2,:));
[DeDtemp]=picketttemp(tempuse, initialstress(2,:));
devisco=initialstress(2,:)/visco*1e6;
% pickett effect refuced stress
%for INDEX=1:length(devisco)
   %if sign(devisco(INDEX))==sign(DeDsh(INDEX))
      %DeDsh(INDEX)=-1*DeDsh(INDEX);
   %end
   %if sign(devisco(INDEX))==sign(DeDtemp(INDEX))
      %DeDtemp(INDEX)=-1*DeDtemp(INDEX);
   %end
%end
DeDT=DeDT-Mean(DeDT);
detotal=-DEDsh-DeDT-devisco-DeDsh+DeDtemp;
```

```
%detotal=-DEDsh-DeDT-devisco-DeDsh+DeDtemp;%+DeDsh+DeDtemp-devisco;%-
creep;
%% -devisco is must-term to ensure the converge
%% -DeDsh is also a must-term to reflect the phenomenon
%% ----detotal=-DeDT-devisco-DeDsh+DeDtemp;
%
dsigma=detotal*Emulti*1e-12;
stress_au=initialstress(2,:)+dsigma;
totalstress=stressprofile(initialstress(1,:),stress_au);
[thermalstress]=thermalstressprofile([temp(1,:);temp(3,:)]);
%initialstress=[initialstress(1,:);thermalstress(2,:)];
[totalstress]=deformcontrol(totalstress, 4.6);
initialstress=[initialstress(1,:);totalstress];
deform=detotal;
end
%
%% (0)
%
function [DKh_Dt,Kh]=khcompute(moistureuse,interval)
M=length(moistureuse(2,:));
DKh_Dt=zeros(1,M);
Kh=zeros(1,M);
for i=1:M
   au=moistureuse(2,i);
   Kh(i)=1-au^3;
   DKh_Dt(i)=-3*au^2*(moistureuse(3,i)-moistureuse(2,i))/interval;
end
end
%% (1)
function [gradient]=gradientcom(temp,interval,index)
% this function aims to compute the gradient of the inputted "temp"; It
% return a row with 1*n elements
% ************************************************
% temp is a 3*n matrix,
% internal is the step time
% index is the differential method, 1, forward, 2 central, 3 backward
% ************************************************
if index==1
   gradient=(temp(2,:)-temp(1,:))/interval;
end
if index==2
   gradient=(temp(3,:)-temp(1,:))/(2*interval);
end
```

```
if index==3
   gradient=(temp(3,:)-temp(2,:))/interval;
end
end
%% (2)
%
function [DEDsh]=desh_dt(day,dayload,sh_all,moistureuse)
%*****************************************************************
% new
% this function computes the differential rate of the shrinkage.
% day stands for the current day
% dayload stands for the load-begining day
%   (1) day is the day the curing ends
%   (2) dayload is the day we want to compute
%   (3) sh_all is the total shrinkage
%   (4) rh(1) is the previous hour
%   (5) rh(2) is the current hour
%   (6) tsh is the ultimate shrinkage
%%
%*****************************************************************
tsh=600; % unit day
au=(day-dayload)/tsh;
tanhvalue=tanh(au^0.5); % an auxiliary variabl
[DKh_Dt,Kh]=khcompute(moistureuse,1);% 1 is one-hour interval, compute Kh and its
rate
%term1=-sh_all*3*DKh_Dt*tanhvalue;
term2=-sh_all*Kh*(1-tanhvalue^2)*0.5/(tsh^0.5*(day-dayload)^0.5);
DEDsh=term2;%+term1;
[DEDsh]=deformcontrol(DEDsh, 8); % threshold 10ue
end
%% (3)
%
function [DeDT]=tempratedeformation(EXP,temp)
% new
% this function designed to compute the deformation induced by temperature
% rate; detail refers to the line 771 in the prelim meeting
[gradient]=gradientcom(temp,1,2); % 2 central different method
DeDT=EXP*gradient*10^6; %10^6 is used to convert the deformation to ue
[DeDT]=deformcontrol(DeDT, 45); % threshold 50ue
end
%% (4)
%
function [DeDsh]=pickettmoisture(sh_all,moistureuse, initialstress)
```

```
% new
%% this function is design to compute the pickett moisture induced
%% shrinkage. Details can be referred to Eq.(29) in the prelim meeting
% rh1=moistureuse(2,:);
% rh2=moistureuse(3,:);
% sh_all=800;
% new
ft=4.6;
g=2; % use to compute the \Psi
r=0.3/ft; % compute the coefficient r, see Bazant's paper
psi=-g*3*moistureuse(2,:).^2;
[gradient]=gradientcom(moistureuse,1,2);
DeDsh=sh_all*psi.*(1-r*initialstress);
DeDsh=DeDsh.*gradient.^2;%gradient; %
DeDsh=DeDsh.*sign(gradient);
[DeDsh]=deformcontrol(DeDsh,1.0); % threshold 5ue
end
%% (5)
%
function [totalstress]=thermalstressprofile(temp)
% this function computes the total, linear, residual stresses induced by
% themal gradient within a slab.
%*************************************************************
% (3) temp must be a 2*N matrix, in which 1st row is coor, 2rd temp
% if temp is a matrix with >2*N matrix, the totalstress only compute the
% stress induced by the 2nd-row temperature profile
%*************************************************************
coor=temp(1,:);
if coor(1)==0 % if the coor begin from the top
   coor=coor-abs(coor(end))/2;
end
%
tslab=abs(coor(1))+abs(coor(end)); %the thickness of concrete slab 10in
EXP=9e-6; % the expansion
EMOD=2.0586e10;
NU=0.15;
k=50*10^6;% unit pa
Xlen=3.6; %slab transverse dimension unit M
Ylen=6; %slab longiditunal dimension unit M
lsmall=((EMOD*tslab^3)/(12*(1-NU^2)*k))^0.25;
lx=Xlen/lsmall;
ly=Ylen/lsmall;
```

```
cxcycurve=[1.05755  1.96403 2.56835 2.8705  3.07194 3.17266 3.22302 3.32374 3.3741
3.42446 3.57554 3.6259  3.77698 3.97842 4.07914 4.28058 4.48201 4.68345 4.93525
5.13669 5.33813 5.58993 5.84173 6.2446  6.54676 7   7.55396 8.10791 8.71223 9.06475
9.51799 10.2734 11.0288 11.7338 12.3381 12.9928
0.00845917  0.047735    0.0915013   0.126571    0.170464    0.205597    0.240746
0.280275    0.315424    0.368156    0.412064    0.4604  0.504309    0.53941 0.58773
0.631623    0.679911    0.723804    0.772077    0.811574    0.84228 0.87297 0.912452
0.951886    0.98256 1.01319 1.03939 1.0524  1.05661 1.0521  1.04756 1.03853 1.0295
1.02049 1.0247  1.02449
]'; % this parameter never change
CX=interp1(cxcycurve(:,1),cxcycurve(:,2),lx,'spline');
CY=interp1(cxcycurve(:,1),cxcycurve(:,2),ly,'spline');
%
tempdata=temp(2,:);
pars=polyfit(coor,tempdata,3);
% initial the polyfit parameters
A=pars(4); % constant
B=pars(3); % z
C=pars(2); % z^2
D=pars(1); % z^3

h2=abs(coor(1)); %half deep of the slab
Mstar=EXP*(B/3.0*h2^3+D/5.0^2*h2^5);
Nstar=EXP*(A*2.0*h2+C/3.0*2*h2^3);
DT=-12*Mstar/(EXP*(2*h2)^2);
con=EMOD/(1-NU);
residualstress=con*(-EXP*tempdata+12*Mstar*coor/((2*h2)^3)+Nstar/(2*h2));
linearstress=DT*EXP*EMOD/((1-NU^2)*2*h2)*(CX*NU+CY)*coor;
totalstress=(residualstress+linearstress)*10^-6;
totalstress=[coor+abs(coor(end));totalstress];
end
%% (6)
%
function [DeDtemp]=picketttemp(tempuse, initialstress)
% new
%% this function aims to compute the pickett deformation induced by
%% tempeature variation
%
ft=4.6;
alpha_1=0.63; % a constant see bazant paper ,0.063
rho=0.3/ft;
[gradient]=gradientcom(tempuse,1,2);
DeDtemp=alpha_1*(1-rho*initialstress).*gradient;
```

```
DeDtemp=DeDtemp.*sign(gradient);
[DeDtemp]=deformcontrol(DeDtemp, 50); % threshold 5ue
end
%% (7)
%
function [stressp]=stressprofile(coor,stress)
% this function compute the stress redistribution with a concrete slab
% using the Nforce and Mforce Mforce method proposed in Mohamed and Hansen
% paper, the stress distribution was computed using elastic model since the
% redistribution is finished immediately
%% parameter given
space=(abs(coor(1))+abs(coor(end)))/200;
coorau=coor;
coor=coor(1):space:coor(end);
stress=interp1(coorau,stress,coor,'spline');
EMOD=2.0586e10;
NU=0.15;
CX=0.69;
CY=1.03;
EXP=9e-6; % the expansion
%%
% interpolation
Nforce=0;
Mforce=0;
h=2*abs(coor(end));
%% compute the force
for i=1:length(coor)-1
    dz=coor(i+1)-coor(i);
    z=(coor(i+1)+coor(i))/2;
    Nforce=Nforce+(stress(i)/2+stress(i+1)/2)*dz;
    Mforce=Mforce-z*(stress(i)/2+stress(i+1)/2)*dz;
end
%% compute the stress
stressres=stress+coor*12*Mforce/h^3-Nforce/h;
Mstar=(1-NU)*Mforce/EMOD;
DT=-12*Mstar/(EXP*(h)^2);
stresslin=DT*EXP*EMOD/((1-NU^2)*h)*(CX*NU+CY)*coor;
stressp=stressres+stresslin;
stressp=interp1(coor,stressp,coorau,'spline');
end
%% (8)
%
function [DE]=deformcontrol(DE, threshold)
```

```
% this function aims to limited the free deformation occurence at the
% surface
%************************************************
% DE is a vector,
% threshold is a scale, must be a positive number
%************************************************
for i=1:length(DE)
   if abs(DE(i))>threshold
      if DE(i)>0
         DE(i)=threshold;
      else DE(i)=-threshold;
      end
   end
end
end
```